

Characterization and role of Tcf21-positive cells during lung alveolarization and neo-alveolarization

Inaugural dissertation

submitted to the

Faculty of Medicine

in partial fulfillment of the requirements

for the PhD-Degree

of the Faculties of Veterinary Medicine and Medicine

of the Justus Liebig University Giessen

by

Rodríguez Castillo, José Alberto

of Monterrey, Mexico

Giessen, 2020

From the Max Planck Institute for Heart and Lung Research
Director / Chairman: **Prof. Dr. Norbert Weißmann**
of the Faculty of Medicine of the Justus Liebig University Giessen

First Supervisor and Committee Member: **Prof. Dr. Werner Seeger**
Second Supervisor and Committee Member: **Prof. Dr. David Warburton**
Committee Members: **Prof. Dr. Thomas Braun**

Date of Doctoral Defense:

December 9, 2021

Table of Contents

1. Introduction.....	3
1.1. General overview of respiratory systems across the animal kingdom and evolutionary aspects.....	3
1.2. Functional anatomy of the human respiratory system.....	5
1.3. Anatomical and histological differences between the respiratory systems of the human and the mouse.....	9
1.4. Cellular composition of the lung.....	11
1.5. Regeneration and regrowth.....	20
1.5.1. Compensatory lung regrowth as a model of regeneration.....	21
1.6. Transcription factor 21.....	23
2. Aim of the work.....	25
3. Methods.....	26
3.1. <i>In vivo</i> experiments.....	26
3.2. Experimental mice.....	26
3.3. Genotyping of transgenic mice.....	27
3.4. Induction of lineage tracing and depletion of Tcf21^{lin}.....	29
3.5. Left pneumonectomy.....	30
3.6. Tissue processing for imaging of cryosections.....	32
3.7. Design-based stereology.....	33
3.9. Preparation of precision-cut lung slices from fixed organs.....	36
3.9. Flow cytometry.....	38
3.10. Fluorescence-activated cell sorting.....	41
3.11. Co-cultures for generation of alveolospheres.....	41
3.12. Image processing, analysis and preparation of figures.....	42
3.13. Statistics.....	42

4. Materials	43
4.1. Equipment	43
4.2. Reagents and drugs	44
4.3. Consumables	46
4.4. Primary antibodies	48
4.5. Secondary antibodies and detection systems	49
5. Results	50
5.1. Characterization of Tcf21⁺ cells in adult mice	50
5.2. Characterization of Tcf21^{lin} cells during secondary alveolarization	55
5.3. Validation of compensatory regrowth after pneumonectomy	62
5.4. Characterization of Tcf21^{lin} during compensatory regrowth	64
5.5. Effect of Tcf21⁺ cell depletion in compensatory lung regrowth	67
5.6. Contribution of the Tcf21 lineage to alveolosphere formation and growth ..	75
6. Discussion	81
7. Conclusion	89
8. Summary	91
9. Zusammenfassung	92
10. References	94
11. Appendix	106
12. List of Figures	107
13. List of Tables	109
14. List of Abbreviations	110
15. Publications	113
16. Acknowledgments	115
17. Affirmation	116

1. Introduction

1.1. General overview of respiratory systems across the animal kingdom and evolutionary aspects

Oxygen is essential for the survival of every complex organism. Aerobic respiration, which is dependent on oxygen, happens to be a particularly efficient mechanism of energy production (aerobic respiration is ~7 times more efficient than anaerobic respiration) (Hsia et al. 2013). As such, aerobic organisms are abundant in the present; however, the dominant life forms have not always depended on molecular oxygen for survival. Life began in a liquid environment under anoxic conditions about 4.5 billion years ago, when no oxygen was present in the atmosphere. Then, only very simple lifeforms, such as bacteria, existed and it was only after the surge of photosynthetic cyanobacteria that atmospheric oxygen concentration rose significantly (Allen and Martin 2007; Lazcano, Oró, and Miller 1983). Once oxygen was sufficiently abundant (around 2 billion years ago), transition of organisms to aerobiosis began (Stamati, Mudera, and Cheema 2011).

Since O_2 is a vital molecule for most complex organisms, it is no surprise that oxygen availability has played a key role in the evolution of life on Earth. The most severe known extinction events in the history of Earth occurred during the Paleozoic (Benton 1995). According to some estimations, 81% to 96% of all marine species became extinct by the end of the Paleozoic (Raup 1979; Stanley 2016). These periods of massive extinctions coincided with maritime hypoxia. It is thought that hypoxia was not the main contributor to mass extinction (Graham et al. 1995); however, since O_2 solubility in air is much higher than in water (>3000%), the acquisition of the ability to breath air likely posed an evolutionary advantage for water-breathing organisms inhabiting a relatively hypoxic environment (Hsia et al. 2013; Packard 1974). Thus, hypoxia may have been an important

driving force for the transition of organisms from the water to the land. In turn, transition to terrestriality required adaptation of preexisting respiratory structures to air breathing or alternatively, repurposing of other tissues to respiratory functions (Maina 1994).

Simple unicellular organisms and some small multicellular microorganisms rely purely on oxygen diffusion to satisfy their metabolic needs. Nonetheless, oxygen diffusion rates impose limits to the way aerobic organisms transport and utilize this molecule. The theoretical maximum size of a spherical organism that acquires O_2 only by diffusion is $\sim 500 \mu\text{m}$ (Maina 1994). Therefore, above this threshold, most multicellular lifeforms require means to efficiently distribute O_2 to the cells. Complex organisms, thus have evolved – often in an independent manner – specialized components that assist respiration at different levels. Some of these components include: 1) Large surface-containing organs that serve as gas exchangers, such as gills (crustaceans, fish, mollusks), book lungs (arachnids), skin (amphibians, arachnids), tracheae (arachnids, insects and myriapods) and lungs (amphibians, birds, crustaceans, some fish, mammals, some mollusks and reptiles); 2) molecules that serve as oxygen carriers (hemoglobins, hemocyanins, hemerythrins); and 3) respiratory media that transports O_2 from gas exchange sites to the locations where it is needed (blood, hemolymph)(Hsia et al. 2013; Terwilliger 1998; Maina 2002).

Compared to other respiratory organs, lungs allow for very efficient gas exchange. Mammals and birds rely on lungs for respiration and are among the organisms with the highest metabolic demands. Compared with amphibians with similar mass, oxygen consumption of mammals is over $100\times$ greater (Maina 1994). Accordingly, in order to meet such metabolic needs, the lungs from animals have developed in such a way that efficient gas exchange is made possible thanks to several adaptations. Among these are: 1) very large respiratory surface that enables simultaneous exchange of large amounts of gas, 2)

maintenance of a gradient that allows for constant flow, and 3) a very thin membrane, which facilitates quick exchange between the two sides of the respiratory surface.

The lung is the most important structure for respiration of mammals. However, the lung depends on other structures and organs to exert its functions. Some of these structures are part of the respiratory system (such as the extrapulmonary airways), while others connect the lung anatomically or functionally with other systems like the nervous, circulatory or muscular systems. The next sections will describe the structure and function of the components of the human respiratory system. For brevity, many interactions with other systems are not mentioned.

1.2. Functional anatomy of the human respiratory system

From both functional and structural points of view, the respiratory system can be divided to two components: 1) the conducting tract (the airway), which transports gases from the atmosphere to the gas-exchange sites and back; and 2) the respiratory zone, where gas exchange occurs. The conducting zone is composed of a series of tube-shaped and branched structures of progressively smaller diameter (trachea, and several generations of bronchi and bronchioles) which connect distally with the respiratory zone that is in turn formed by respiratory bronchioles, alveolar ducts and alveoli.

The trachea is the most proximal component of the airway. In the human (females and males), the trachea is 10–13 cm in length and 1–2.5 cm wide in the coronal plane, being slightly smaller in females than in males (Breatnach, Abbott, and Fraser 1984; Brand-Saberi and Schäfer 2014). Around the anterior and lateral aspects of the trachea, 15–20 incomplete C-shaped cartilaginous rings prevent the trachea from collapsing. The trachea connects at its proximal end with the larynx and bifurcates laterally into two main bronchi

at the level of the carina. The main (also known as primary or lobar) left and right bronchi transport air between the trachea and the lungs.

Entry of the airway to the lung occurs at the hilus, where the main bronchi penetrate the mediastinal surface of the lung along with the pulmonary veins and arteries. Once within the lung, the left primary bronchus promptly bifurcates into secondary bronchi; two left lobes (upper and lower) are supplied each by one of these secondary bronchi. Conversely, the right primary bronchus gives origin to three branches that ventilate each of the three right lobes (upper, middle and lower lobes). The pulmonary lobes from each side are separated by interlobar fissures.

The branching pattern continues with the division of primary bronchi into secondary bronchi. Secondary bronchi then divide further into tertiary or segmental bronchi. After some further generations of bronchi surrounded by progressively scarcer cartilage, bronchi eventually transition to primary bronchioli, which differ from the bronchi precisely by a complete lack of cartilage. A dichotomous branching pattern continues dividing the air-conducting structures along the proximal-distal axis into progressively smaller structures for a total of up to 21-25 generations of airways, finalizing at the terminal bronchioli, the most distal components of the conductive zone (Suarez, Dintzis, and Frevert 2012; Tomashefski and Farver 2008).

The respiratory zone contains the lung parenchyma, which undertakes the primary function of the lung: gas exchange. The functional unit of the lung is the acinus, the tissue supplied by a single terminal bronchiole. At the beginning of the respiratory zone, the respiratory bronchioles, which are partially capable of gas exchange, derive into alveolar ducts and finally into alveoli.

Alveoli are the basic unit of gas exchange and are polymorphic hollow structures that passively and cyclically inflate and retract during breathing. By the time air reaches the alveoli, air has passed through ~23 branching points and divided to fill up to ~400 million alveoli (Weibel 1963; Ochs et al. 2004). This massive compartmentalization of the lung which finishes with the thin-walled and well vascularized alveoli, allows for maximization of gas exchange by increasing the surface available for such process. In adult humans, total respiratory surface area is over 126 m² (Tomashefski and Farver 2008).

In the walls of alveoli, gas exchange occurs passively by diffusion between the air inside the alveoli and the blood contained in pulmonary capillaries, where oxygen enters the bloodstream and CO₂ is released into the expired air. During exchange gases have to cross what is known as the alveolar-capillary membrane. This “membrane” is formed by a thin layer of alveolar surfactant (which covers the alveolar lumen and prevents the alveoli from collapsing), a single layer of alveolar epithelial cells, some extracellular matrix and the capillary endothelial cells. This alveolar-capillary membrane is only ~0.6 μm thick in the human, which contributes to the efficiency of gas exchange (Tomashefski and Farver 2008).

In order to exert an efficient gas exchange, the lung does not only display an efficient ventilatory system that partitions the inhaled air into a very large exchange surface, it also requires an efficient system for distribution of poorly oxygenated blood to the gas exchange sites where, once oxygenated, blood can be sent back for re-distribution to the rest of the organs. Such system is known as the pulmonary circulatory system.

The pulmonary circulation connects with the heart at the right ventricle, where poorly oxygenated blood is pumped into the pulmonary trunk. From there, the blood is distributed to both the left and the right pulmonary arteries. Then, each pulmonary artery enters the

lung through the hilus and undergo multiple bifurcations. In the lung, blood continues its way along these successive arterial ramifications. Eventually, pulmonary arteries, which usually follow the path of the airway, transition into arterioles and finally, into capillaries (Tomashefski and Farver 2008).

Capillaries are an essential component of gas exchange. In the lung, capillaries do not follow the typical arrangement observed in other organs where adjacent capillaries follow a parallel path. Instead interconnected segments of pulmonary capillaries loop around pillars of connective tissue within the alveolar walls, generating a complex network that surrounds alveolar airspaces (Willführ et al. 2015). Upon oxygenation at the alveolar capillaries, blood is collected by pulmonary venules which then merge into pulmonary veins. Then, after multiple merging generations of pulmonary veins, blood exits each lung through a pair of pulmonary veins (superior and inferior). Subsequently, the four primary pulmonary veins drain the blood into the left atrium.

The pulmonary circulatory system is a low-pressure/high-capacity system. Indeed, with every cardiac beat, the pulmonary circulation receives the entire systemic venous return from the rest of the organism. Therefore, this system is designed to accommodate a large flow with minimal pressure differential (Tomashefski and Farver 2008).

The pulmonary parenchyma is in close contact with the oxygen-rich inhaled air. For this reason, the lung can directly receive most of the oxygen it requires for its own metabolic functions from the air or from the pulmonary circulation. However, the lung possesses a dual circulatory system where vessels derived from the systemic circulation contribute to the oxygenation of lung tissues, distributing blood derived from the left heart to structures which are not in contact with air nor the alveolar capillaries (bronchi, lymph nodes, and the visceral pleura) (Ellis 2005). In the lung, these systemic vessels are known as bronchial

vessels. Bronchial arteries are typically derived from the third intercostal artery on the right side and from the aorta on the left side. Bronchial arteries supply the bronchi up to the level of respiratory bronchioli, then bronchial blood returns partially through bronchial veins and another part of the bronchial blood returns via the pulmonary circulation (Tomashefski and Farver 2008; Charan, Thompson, and Carvalho 2007).

The surface of the lung (including the interlobar fissures) and the inner surface of the chest wall are covered by the visceral pleura and the parietal pleura, respectively. The pleura are composed of a layer of cuboidal mesothelial cells and a layer of connective tissue. The pleura also contains a network of lymphatic vessels that prevent abnormal accumulation of pleural fluid in the pleural space. The virtual space (almost empty under normal conditions, except for a small amount of pleural liquid) between both opposing pleurae is the pleural space. This virtual space is vital for maintaining negative pressure in the region, necessary for lung inflation following inspiratory movements of the thorax and for preventing lung collapse during expiration (Tomashefski and Farver 2008; Suarez, Dintzis, and Frevert 2012; Lai-Fook 2004).

1.3. Anatomical and histological differences between the respiratory systems of the human and the mouse

With the availability of transgenic animals (which are for the most part mice), a plethora of scientific studies, including the present work, have used the laboratory mouse as a model organism studying the biology and physiology of the respiratory system (Rawlins and Perl 2012; Swonger et al. 2016; Parker 2011). Since noticeable differences can be observed in the anatomy and histology of mice and humans, a correct understanding of the similarities and differences between the respiratory systems of the human and the mouse is highly relevant.

Mice possess a comparatively low mass, and the metabolic rate and respiratory frequency of these rodents are much higher than in humans. These factors account for some of the structural differences found between the respiratory systems of these two species. For example, in order to avoid excessive airway resistance to airflow, mice exhibit relatively larger lumen size than humans. While in the human airway, cartilage is found from the trachea to the most distal generation of bronchi to prevent collapse of the ducts, in the mouse, cartilage exists only in the trachea and in the proximal segment of the main bronchi, being virtually absent in intrapulmonary airways. This lack of intrapulmonary cartilage makes discrimination of small bronchi and bronchioli challenging in mouse lung sections (Suarez, Dintzis, and Frevert 2012).

In contrast to the dichotomous branching patterning observed in the human, where a parent branch bifurcates into two daughter branches of approximately equal size; the mouse airway exhibits monopodial branching by which, following an irregular dichotomy, a parent branch sprouts two daughter branches of disproportionate size to each other. Additionally, terminal bronchioles from the mouse usually divide into alveolar ducts directly, without transitioning to respiratory bronchioles first as in the human lung. In mice, lung parenchyma occupies a larger fraction of the lung volume than it does in the human (18% vs 12%) (Table 1) (Suarez, Dintzis, and Frevert 2012).

While the human right and left lungs are composed of three and two lobes, respectively; the murine lung contains four right lobes (cranial, middle, caudal and accessory – or cardiac, due to its proximity with the heart–) and a single left lobe. Another difference between the human and mouse lung is that the visceral pleura of mice is very thin being typically composed of a single cell layer of mesothelial cells over collagen, while the human parietal pleura is comparatively thicker (Suarez, Dintzis, and Frevert 2012).

Table 1. Differences between human and murine respiratory systems. Adapted from Suárez, 2012.

Feature	Human	Mouse
Number of lobes (right + left)	3 + 2	4 + 1
Airway generations	17-21	13-17
Airway branching pattern	Dichotomous	Monopodial
Respiratory bronchioli	Present	Commonly absent
Relative parenchymal volume in the lung (%)	12	18
Alveolar diameter (μm)	200-400	39-80
Alveolar-capillary membrane thickness (μm)	0.32	0.62

1.4. Cellular composition of the lung

The lung is home to over 30 different cell types (Gandjeva and Tuder 2018) which have defined phenotypes and roles. In the lung parenchyma, alveolar epithelial cells type 1 (AEC1), and type 2 (AEC2) and the rare brush cells form a continuous layer of cells separated from the alveolar lumen by the epithelial lining fluid or pulmonary surfactant. The majority of the respiratory surface of the lung is occupied by AEC1. These cells have very flat and thin morphology that facilitates gas exchange by minimizing the distance between capillaries and airspaces. On the other hand, AEC2 are cells commonly located in alveolar corners and are in charge of producing surfactant (Weibel 2015). In addition, AEC2 serve as stem cells of the alveolar epithelium, being capable of self-renewal and of differentiating to AEC1 (Barkauskas et al. 2013). Within the alveolar septum, endothelial cells form a network of capillaries that bring erythrocytes to the site of gas exchange (Weibel 1963). In addition, different populations of interstitial cells such as fibroblasts and pericytes, also reside in the septum (Vaccaro and Brody 1978; Weibel 1974).

Because of the relevance of fibroblasts to the present work, the most well characterized fibroblast subsets of the lung are described in the following sections, after providing some context about the general phenotype and function of fibroblasts in the organism.

1.4.1. Pulmonary fibroblast subsets in homeostasis and disease

Fibroblasts are cells that have been found in virtually all tissues and organs. Classically, and mostly as a result of observations made *in vitro* using cell culture systems, fibroblasts can be described as spindle shaped or fusiform, often contractile, and highly metabolically active cells (McAnulty 2007; Abercrombie 1978). Some other stereotypical features of fibroblasts are a contoured elliptical nucleus and well developed granular endoplasmic reticulum and Golgi apparatus (Komuro 1990). Closely linked to the extracellular matrix (ECM) *in vivo*, fibroblasts are not only characteristically associated with ECM molecules but are also the main cell type responsible for the initial production, maintenance and remodeling of the ECM (McAnulty 2007; Sorrell and Caplan 2009)

The classical interpretation of the phenotype and roles of fibroblasts has been challenged during the past decades due to several factors, including the following: 1) even *in vitro*, fibroblasts exhibit morphological variation. This variation has served as basis for selection of fibroblast subsets for different applications (Sorrell, Baber, and Caplan 2007). 2) The discovery of new fibroblast functions not initially attributed to this cell type; and conversely, 3) fibroblast-like characteristics have been ascribed to cells that were once thought unrelated to fibroblasts for displaying functions previously considered atypical of fibroblasts (i.e. lipid storage in the stellate cells of the liver [Wake 1971]), endocrine release of Erythropoietin by renal interstitial fibroblasts [Pan et al. 2011], presence of actin and vimentin filaments in Leydig cells, fibroblast-like cells in the intestinal villi. Although a better understanding of the cell biology of fibroblasts has been achieved, elaborating a concise

definition of what a fibroblast is and what characteristics clearly separate fibroblasts from other interstitial cells is challenging. However, based on current knowledge, fibroblasts are a heterogeneous population of interstitial cells that display different phenotypes and perform a high variety of functions according to the cell lineage, tissue localization, microenvironment and mechanical stimuli. These cells have shown to be crucial for a variety of processes, such as ECM homeostasis, wound healing, tissue repair, fibrosis formation, maintenance of stem cell niches and even production of certain hormones. (Sorrell, Baber, and Caplan 2007; El Agha, Kramann, et al. 2017; Zeisberg and Kalluri 2015; Pastuła and Marcinkiewicz 2019).

As in other tissues, fibroblasts in the lung display a variety of phenotypes that fulfill specialized roles during homeostasis and repair of lung tissue. In this organ, fibroblasts exist in different compartments (e.g. in the parenchyma, vessels and bronchi). Since fibroblasts are localized to the lung parenchyma, lung interstitial fibroblasts are of particular interest for the present work. The next section is dedicated to describe the main functions and phenotypes encountered only in lung interstitial fibroblasts.

1.4.2. Subpopulations of fibroblasts in the lung

Lung interstitial fibroblasts are mesenchymal cells enclosed within the alveolar walls. At least two phenotypic populations of interstitial fibroblasts have been described in the literature: the myofibroblast and the lipofibroblast. The main characteristic of the former is the expression of the contractile protein alpha smooth muscle actin (α -SMA) (Barron, Gharib, and Duffield 2016), while, the most prominent feature of lipofibroblasts is the presence of lipid droplets.

1.4.2.1. Lipofibroblasts

Lipofibroblasts are lipid droplet-laden cells found at the bases of the alveolar septa. Lipofibroblasts display fibroblast characteristics but also exhibit overlapping features with other mesenchymal or fibroblast cell types, such as adipocytes, smooth muscle cells, pericytes and myofibroblasts. In addition to containing a high lipid load, lipofibroblasts also contain glycogen deposits (McGowan and Torday 1997; Spit 1983) and intermediate contractile filaments similar to those of myofibroblasts (McGowan and Torday 1997; Kaplan, Grant, and Brody 1985).

The presence of lipid vacuoles in the lung mesoderm was first described by O'Hare and Sheridan in 1970. Cells containing these vacuoles were initially called lipid-laden fibroblasts (O'Hare and Sheridan 1970), while in the following years mesenchymal lung populations were classified as lipid interstitial cells or non-lipid interstitial cells. Because evidence has accumulated regarding the fibroblast characteristics displayed by lipid interstitial cells, in the present the preferred term for this cell type is lipofibroblast (McGowan and Torday 1997). This fibroblast subset has been shown to support the metabolism, growth, and differentiation of AEC2, with which lipofibroblasts maintain close contact with (J. Torday, Hua, and Slavin 1995; Besnard et al. 2009; Barkauskas et al. 2013)

Torday et al. demonstrated that transfer of triglycerides can occur from fibroblasts to AEC2. In their experiments, AEC2 were cultured with primary rat fibroblasts which had been previously incubated with [³H]-triolein, a radioactively labeled triglyceride. Upon co-culture, [³H]-triolein was detected in the extracted phospholipids from re-isolated AEC2 at higher levels than the radioactive [¹⁴C]-glucose added to the co-culture as control, suggesting

lipofibroblasts provide AEC2 with lipid substrates for surfactant production (J. Torday, Hua, and Slavin 1995).

Pulmonary lipofibroblasts also provide a site for storage of the lipid-soluble vitamin A, which in turn plays an important role during alveolarization and for lung extracellular matrix homeostasis through activation of retinoic acid receptors (McGowan, Doro, and Jackson 1997; McGowan and Holmes 2007; Massaro and DeCarlo Massaro 2010) .

Several markers have been associated with a lipidic phenotype in fibroblasts. This knowledge has offered new insights into the functions of lipofibroblasts and has provided alternate means for identifying these cells. In culture, McQualter et al. observed that a population of non-endothelial mesenchymal cells expressing Sca-1 and Thy-1 (thymus cell antigen 1, theta), but not CD166 (CD31⁻, CD45⁻, Sca-1⁺, Thy-1⁺, CD166⁻) differentiated to lipofibroblasts when stimulated with BMP4. In contrast, another population of Thy-1 negative, CD166-expressing cells (CD31⁻, CD45⁻, Sca-1⁺, Thy-1⁻, CD166⁺) differentiated into myofibroblasts when exposed to transforming growth factor beta 1 TGF-β1 (McQualter et al. 2013).

Including the initial study which described lipofibroblasts in rat lung tissue, most research about the lipofibroblast cell biology has been conducted in rodents (Vaccaro and Brody 1978; Maksvytis, Vaccaro, and Brody 1981; Kaplan, Grant, and Brody 1985; McGowan, Doro, and Jackson 1997; Hagood et al. 2005; Ntokou et al. 2017; El Agha, Kramann, et al. 2017) and to date, the presence of lipofibroblasts in the human lung alveolar septum remains controversial (Tahedi et al. 2014; Rehan et al. 2006). Employing stereological techniques, Tahedi and coworkers estimated and compared the abundance of lipid droplets in lungs of 14 different mammalian species (including *Homo sapiens*) using stereological techniques on electron microscopy preparations of tissues. Based on the

identification of lipid droplets, lipofibroblasts were only found in rodents (mouse, rat and rabbit), but could not be detected in human specimens (Tahedi et al. 2014). The results from this study conflict with a previous report from Rehan et al. in which the authors identified lipofibroblasts in human autopsy specimens by the presence of lipid droplets and immunostaining for adipocyte differentiation-related protein (ADRP). Additionally, cultured human embryonic lung fibroblasts and fibroblasts isolated from lung biopsies demonstrated several features that had been previously observed in the rodent lipofibroblast, such as lipid droplets, expression of ADRP and Thy-1, absence of α -SMA and the ability to capture triglycerides upon treatment with parathyroid hormone-related protein (PTHrP) (Rehan et al. 2006; Al Alam et al. 2015).

Identification of lipofibroblasts in human lungs by means of lipid droplet visualization has proven challenging. However, other lipofibroblast features that have been observed in animal models could be employed to reveal functionally analogous populations of fibroblasts in human tissue. Examples of these features are the expression of cell markers such as ADRP, platelet-derived growth factor receptor alpha (PDGFR- α), fibroblast growth factor 10 (FGF10), Thy-1, retinoic acid receptors, peroxisome proliferator-activated receptor gamma (PPAR- γ), PTHrP receptor (PTHrP-R), etc. (Varisco et al. 2012; Ahlbrecht and McGowan 2014; Torday, Torres, and Rehan 2003).

The presence of lipofibroblasts during lung development has been investigated by several authors. Lipofibroblasts have been observed as early as in the canalicular stage of lung development in the rat. Torday reported that the triglyceride load of fetal lung rat fibroblasts increased up to five-fold between days 18 and 22 of gestation (saccular stage of development). Also on the saccular stage, ADRP expressing cells were found to be abundant in the fetal mouse interstitium (E 18.5), where some of these ADRP⁺ cells co-expressed PDGFR α ⁺ (Ntokou et al. 2015). Although rodent lipofibroblasts have been

identified on prenatal stages of development, pulmonary lipofibroblasts seem most abundant during postnatal lung development (except in hamsters); afterwards, the lipid droplet content of mesenchymal cells decreases significantly (Sorokin, Padykula, and Herman 1959; Tahedl et al. 2014).

Current evidence suggests that the postnatal abundance of lipofibroblasts also seems to be species-dependent. These cells have been identified in both immature and mature specimens of rats, mice, hamsters and rabbits (Spit 1983; Tahedl et al. 2014). In one study, rodent lipofibroblasts were estimated to represent about 50% of the total interstitial fibroblasts according to cell profile analysis in electron microscopy tissue sections. However, clear differences were identified regarding the abundance of lipid droplets in interstitial cells. While lipid-containing fibroblasts are common in the adult mouse and contained abundant intracellular lipids, lipid droplets were absent in about half and a third of the cells with lipofibroblast characteristics in the rats and hamsters respectively (Kaplan, Grant, and Brody 1985).

1.4.2.2. Lipofibroblasts in the alveolar stem cell niche

Several locations at different levels of the airway and in the lung parenchyma are home to stem cell niches. It is thought that the special microenvironment of these niches maintains certain cell types – stem cells – in a state of relative undifferentiation. Upon injury, these stem cells respond by proliferating and differentiating to repopulate the damaged tissue. In the lung parenchyma, lipofibroblasts have been proposed to contribute to the maintenance of the alveolar stem cell niche (Wansleeben et al. 2013; Barkauskas et al. 2013). Recent experiments have confirmed the role of AEC2 as stem cells of the alveolar epithelium. There, AEC2 have been demonstrated to self renew and differentiate over long periods of time during homeostasis and showed increased clonal expansion upon partial genetic

ablation AEC2 (Barkauskas et al. 2013). An early study explored the supportive role of fibroblasts during AEC2 expansion using co-cultures of AEC2 and lipofibroblasts isolated from fetal rat lungs. In that study, production of surfactant protein B (SP-B) and expansion of AEC2 were stimulated by lipofibroblasts (Torday, Torres, and Rehan 2003). More recently, murine PDGFR- α stromal cells including a subpopulation of lipid-droplet containing cells supported the growth and differentiation of organoids formed by AEC2 (Barkauskas et al. 2013).

1.4.2.3 Myofibroblasts

As part of the healing process that follows injury in several tissues, some fibroblasts proliferate and acquire features such as higher contractility and enhanced matrix deposition to provide increased tissue resistance and to contribute to matrix remodeling. These fibroblasts with enhanced contractile properties given by contractile microfilaments or stress fibers similar to those found in smooth muscle cells are known as myofibroblasts (Desmoulière et al. 1995; McAnulty 2007; N. Sandbo et al. 2016). Myofibroblasts appear transiently during tissue repair and as healing progresses, cells with this phenotype are usually removed from the tissue by apoptosis at the time that the local microenvironment changes from a matrix deposition state to one that favors matrix degradation (Desmoulière et al. 1995).

Characteristically, myofibroblasts contain α -SMA, a contractile protein found also in the cytoskeleton of smooth muscle cells in the form of microfilament bundles. *In vitro* data have demonstrated that the ability of myofibroblasts to contract is proportional to the expression of α -SMA, highlighting the importance of this protein for contractility (Hinz et al. 2001). Furthermore, experiments by Ibrahim et al. revealed that α -SMA participates in wound contraction. They reported that α -SMA-deficient mice exhibited delayed skin wound

closure as compared to non-deficient mice. However, α -SMA was shown not to be essential for this process since complete wound closure eventually occurred in α -SMA-deficient mice as well (Ibrahim et al. 2015). In addition to α -SMA, myofibroblasts may also contain other contractile proteins such as non-muscle myosins, (ACTB, ACTG1) and smooth muscle myosin heavy chains; as well as molecules that contribute to the stability of the cell architecture, cell motility, formation of stress fibers and establishment of focal adhesions (Eddy, Petro, and Tomasek 1988; Ibrahim et al. 2015; Burridge and Chrzanowska-Wodnicka 1996; Lo et al. 2004; Nathan Sandbo and Dulin 2011).

Despite the contribution of myofibroblasts to wound healing, the presence of these cells during disease may be detrimental to the host tissue in the long term. When repair mechanisms fail to restore tissue homeostasis or if repeated or chronic insult takes place, myofibroblastic cells may persist in the site of injury and abnormal accumulation of ECM may occur. This phenomenon known as fibrosis is part of a plethora of chronic diseases that can affect various organs (including several forms of interstitial lung disease, cystic fibrosis, liver fibrosis, cirrhosis, and renal tubulointerstitial fibrosis). During fibrosis, abnormal aggregation of fibroblasts and ECM in the interstitium commonly interferes with the normal function of the organs. For example, in the lung, fibrosis may lead to inefficient gas exchange; while in the liver, fibrosis can significantly impair metabolism, hemostasis, coagulation and portal tension. Similarly, in the kidney, glomerular filtration and production of several hormones might be reduced (Desmoulière, Darby, and Gabbiani 2003; Rockey, Bell, and Hill 2015).

In the lung, however, myofibroblasts do not only play a role during the pathophysiology of fibrosis and as a response to injury, but are also essential components of non-pathological processes, including development. During alveolarization, murine myofibroblasts have been demonstrated to be crucial for production of elastin, and are thought to be important

for secondary septum formation (Boström et al. 1996; Boström, Gritli-Linde, and Betsholtz 2002). In this context, alveolar myofibroblasts were localized adjacent to elastin bundles at the tip of the forming septal tips and at the entry ring of newly formed alveoli (McGowan et al. 2008; Branchfield et al. 2016). Furthermore, myofibroblasts seemed more abundant at the time that elastin content peaked. Additionally, disturbed three-dimensional (3D) configuration of myofibroblasts was observed in various models of impaired alveolarization. It has been proposed that myofibroblasts play an essential role in alveologenesi; however, a causal relationship between myofibroblast organization and alveolarization has not been clearly established yet (Branchfield et al. 2016). Similar to the presence of myofibroblasts in healing wounds, the expression of α -SMA in developing lungs is transient: After the peak of alveolarization in the mouse lung, α -SMA-expressing fibroblasts decrease dramatically within the lung parenchyma; and in the normal adult lung, alveolar myofibroblasts are virtually undetectable unless stimuli like fibrosis or regrowth processes take place (Habieli and Hogaboam 2017; Chen et al. 2012; Branchfield et al. 2016).

1.5. Regeneration and regrowth

After tissue injury, the wound repair process in human adults commonly results in scar formation, leaving some non-functional fibrotic tissue once the injurious stimulus has ceased. Some injuries do not simply cause damage, but permanently remove part of the tissue instead, such as amputations. In these cases, the lost tissue is not recovered and a scar is left in the site of wound healing. Some organisms, however, are capable of recovering large portions of tissue. An extreme case of regenerative potential is the planarian, which can fully regenerate an intact individual upon amputation of the majority of the organism. Among vertebrates, salamanders are a popular model organism to study

regeneration since some of these animals can undergo limb regeneration without scar formation (Gurtner et al. 2008; Sánchez Alvarado 2006).

Regeneration in both planarians and salamanders is an example of epimorphic regeneration, a remarkable process which involves the recovery of the anatomical integrity of the lost tissue upon differentiation, proliferation and redifferentiation of cells at the amputation site. Generally speaking, the potential for this type of regeneration in mammals is rather limited in extent (Seifert and Muneoka 2018). Nonetheless, loss of large portions of tissue of certain organs can induce regrowth, rather than epimorphic regeneration of the remaining tissue in multiple mammal organisms. Perhaps the most well known and clinically relevant example of the capacity of mammal organs for regrowth is liver regeneration. Liver regeneration is the result of proliferation of mature cells (hyperplasia) and does not involve recovery of the original anatomical integrity of the organ. For example, if an hepatic lobe is excised, the rest of the lobes grow and compensate the function and mass of the missing lobe, but the dissected lobe is not replaced by a new one. In fact, this property allows therapeutic transplantation of single hepatic lobes from living individuals unto recipients (Taub 2004). Similarly, after resection of entire pulmonary lobes of small species of mammals, compensatory regrowth is induced in the remaining lung lobes (Paisley et al. 2013).

1.5.1. Compensatory lung regrowth as a model of regeneration

Evidence gathered from studies conducted in animals indicates that the compensatory lung regrowth that follows experimental partial pneumonectomy is the result, at least in part, of the formation of new tissue and alveoli (neopalveolarization) rather than mere expansion of preexisting airspaces (Hsia 2006; Fehrenbach et al. 2008; Voswinckel 2004). It has become clear that the extent and speed of the compensatory regrowth is both age-

and species-dependent: Smaller species (e.g. rodents) exhibit more complete and faster responses after pneumonectomy than larger species do; and aging negatively impacts regrowth (Paxson et al. 2011; Holmes, C. Thurlbeck 1979; Hsia 2006; Cagle, Langston, and Thurlbeck 1988).

Despite the phenomenon of compensatory lung regrowth having been investigated for nearly a century and, having been robustly demonstrated across a variety of species including mice, rats, rabbits and dogs (Addis 1928; Cohn 1939; reviewed by Hsia 2004); evidence for the occurrence of regrowth in human lungs has been scarce and limited to lung function tests and imaging techniques. Data from studies involving patients who had undergone pneumonectomy during childhood suggest that compensatory regrowth may occur in humans if the stimuli causing the loss of lung volume occur early in life (Stiles et al. 1969; Laros and Westermann 1987; Werner et al. 1993; Nakajima et al. 1998). In addition, a couple of case reports can be found in the literature. Ciric et al. reported the case of a woman who experienced an autopneumonectomy, presumably during childhood, and who had lung function tests within normal range at the age of 23. The patient's lung had a structurally normal appearance as revealed by computed tomography (CT) scan (Ciric et al. 2003). A second case was reported by Butler et al.: a woman which lung function tests, CT and hyperpolarized Helium-3 magnetic resonance imaging were compatible with the occurrence of lung regrowth 15 years after a right-sided pneumonectomy (Butler et al. 2012). Regardless of the limited capacity of the mature human lung for regrowth, enthusiasm remains that the study of the mechanisms behind compensatory regrowth in other species might pave the way towards future regenerative strategies against chronic lung diseases where disruption of lung parenchyma exists (Rodríguez-Castillo et al. 2018).

The use of the compensatory regrowth model in mice offers a number of advantages for the study of regenerative processes vs other models and species: 1) a large number of subjects can be studied in a relatively short amount of time compared to larger species since rodents exhibit a rapid and robust regrowth response following pneumonectomy. 2) Compensatory regrowth in mice extends to animals operated during adulthood. Therefore, the model can be used to investigate regeneration in mature animals, which is desirable for translational purposes. 3) The use of transgenic animals facilitates the investigation of cellular and molecular aspects of lung regeneration with loss/gain of function strains (including knockout and conditional knockout mice) or reporter and conditional reporter mice. 4) Compared to other models of regeneration/repair, the proportion of alveolar units lost in the pneumonectomy model is known and highly reproducible since entire lobes are resected. 5) The process of regrowth after pneumonectomy occurs without inflammation of pulmonary tissue (Thane, Ingenito, and Hoffman 2014; Paisley et al. 2013; Rawlins and Perl 2012).

To date, several cell types have been observed to participate in compensatory lung regrowth and multiple involved mechanisms have been identified (Thane, Ingenito, and Hoffman 2014). Further research will likely continue expanding our knowledge about this phenomenon and hopefully, this knowledge will enable the discovery of innovative regenerative therapies for chronic lung diseases.

1.6. Transcription factor 21

The transcription factor 21 (Tcf21) is a member of the b-Helix-Loop-Helix (bHLH) family of transcription factors encoded by a homonymous gene located on chromosome 6 in humans and chromosome 10 in mice. Current knowledge about the biological role and anatomical location of Tcf21 has been gained from studies in mice. Tcf21 is expressed

during several stages of prenatal development, mostly by mesenchymal cells located in multiple organs (e.g. heart, kidney, lung, cranial muscles, testes, ovary, adrenal gland and spleen), (Quaggin et al. 1999; Acharya et al. 2011). The relevance of Tcf21 for the development of the lung is highlighted by studies on Tcf21-deficient (Tcf21^{-/-}) mice. Quaggin and collaborators reported that Tcf21^{-/-} embryos also display impairment of epithelial branching morphogenesis. Additionally, Tcf21^{-/-} mice die immediately after birth and displaying severely hypoplastic lungs and impaired differentiation of the distal epithelium (Quaggin et al. 1999). Other studies showed that Tcf21 mRNA expression in the murine lung is concentrated in CD45⁻PDGFR α -GFP^{low} cells at postnatal day (P)8, during secondary alveolarization; and that the Tcf21 lineage partially overlaps with PDGFR α -GFP⁺ cells in the lung parenchyma of adult mice (McGowan and McCoy 2014; Swonger et al. 2016).

2. Aim of the work

Previous evidence indicates that Tcf21 expression is essential for prenatal lung development and suggests that Tcf21 expression in the lung is enriched in mesenchymal cells; however, formal characterization of the postnatal location, phenotype and function of Tcf21 had not been performed prior to the present study. Therefore, the scope of the present study was to identify and characterize the phenotype and role of pulmonary Tcf21-expressing cells during homeostasis, late lung development and in a model of murine pulmonary regrowth.

3. Methods

3.1. *In vivo* experiments

All animal experiments described in this work were approved by the local authorities (*Regierungspräsidium* Darmstadt: B2/369, B2/1129, B2/1151 and B2/1204).

3.2. Experimental mice

3.2.1. *Wild-type mice*

Unless noted otherwise, C57BL/6J mice were employed for animal experiments.

3.2.2. *Transgenic mice*

Tcf21^{tm3.1(cre/Esr1*)Eno} knock-in Cre driver mice (Tcf21^{iCre/+}, MGI:5442346), kindly donated by Dr. Michelle Tallquist from the University of Hawaii, were bred with B6.Cg-*Gt(ROSA)26Sor*^{tm14(CAG-tdTomato)Hze}/J inducible reporter mice (R26^{tdT}, The Jackson Laboratory: 007914)(Acharya et al. 2011; Madisen et al. 2010). Resulting Tcf21^{iCre/+};R26^{tdT/tdT} and Tcf21^{+/+};R26^{tdT/tdT} mice were inbred in order to keep tdTomato homozygosity. For Tcf21 lineage tracing experiments, Tcf21^{iCre/+};R26^{tdT/tdT} mice were employed. Upon exposure of Tcf21^{iCre/+};R26^{tdT/tdT} mice to tamoxifen, Cre-driven recombination in Tcf21-expressing cells allowed for the expression of the fluorescent reporter protein tdTomato by the Tcf21⁺ lineage. When necessary, tdTomato fluorescence was identified by comparing Tcf21^{iCre/+};R26^{tdT/tdT} tissue or cells with Tcf21^{+/+};R26^{tdT/tdT} samples, which lack tomato expression. Animals ready for *in vivo* induction of Tcf21⁺ cell depletion were created by breeding Tcf21^{iCre/+};R26^{tdT/tdT} mice with *Gt(ROSA)26Sor*^{tm1(DTA)Lky}/J mice (R26^{DTA}, The Jackson Laboratory: 009669, MGI: 009670) (Voehringer, Liang, and Locksley 2008). Resulting Tcf21^{iCre/+};R26^{tdT/DTA} mice

allowed for depletion of Tcf21⁺ cells via expression of the A subunit of diphtheria toxin (DTA) upon tamoxifen administration.

For experiments involving lineage tracing of ADRP, Plin2^{tm1.1(Cre/ERT2)Mort} (ADRP^{CreERT}) Cre-driver mice were mated with Gt(ROSA)26Sor^{tm4(ACTB-tdTomato,-EGFP)Luo/J} (mTmG) mice. Resulting ADRP^{CreERT};mTmG mice exhibit constitutive expression of the tamoxifen-responsive Cre/ERT2 in ADRP⁺ cells along with expression of membrane-bound tdTomato in all cells. Upon tamoxifen induced recombination in ADRP^{CreERT};mTmG mice, tdTomato expression switches to GFP expression in ADRP⁺ cells, allowing tracking of the ADRP lineage traced cells (ADRP^{lin}).

3.3. Genotyping of transgenic mice

End-point PCR and DNA electrophoresis were performed to investigate the genotype of loci of interest in transgenic mice. DNA was isolated from a piece of tissue obtained from the tail of P10–P14 mice using the AccuStart™ II Mouse Genotyping Kit (Quantabio, Beverly, MA, USA) following manufacturer's recommendations. The PCR primers are listed in table 2, and the PCR programs are described in table 3. The PCR products were subsequently loaded in agarose (1–1.5% [w/v]) gels containing ethidium bromide (0.2 µg/ml) and run in an electrophoresis chamber to resolve amplified DNA fragments. DNA bands were visualized and documented with a transilluminator (INTAS UV-systeme, Intas Science Imaging Instruments, Germany). Example images of genotyping gels are provided in Appendix 1.

Table 2. PCR primers for mouse genotyping

Mouse line	Primer name	Primer sequence	Size (bp)
Tcf21 ^{iCre}			WT: 321 Cre: 500
	Tcf21 F	5'-GCTTCCGATATCCAGATCCAGAC-3'	
	Tcf21 R	5'-CAAACCCTAGCACAAATCACTCGC-3'	
	MerP	5'-TTCTCCAGGCTCAAGACCAC-3'	
ADRP ^{CreERT}			Cre: 300
	Cre F	5'-TGCCCCTCTATGACCTGCTGCT-3'	
	Cre R	5'-TGCTCTGGTGACAAGGAGGGGT -3'	
R26 ^{tdT} or mTmG			WT: 330 Reporter: 250
	R26 F	5'-CTCTGCTGCCTCCTGGCTTCT-3'	
	R26 R	5'-CGAGGCGGATCACAAGCAATA-3'	
	CAGP R	5'-TCAATGGGCGGGGGTCGTT-3'	
R26 ^{DTA}			WT: 603 DTA: 650
	WT F	5'-CCAAAGTCGCTCTGAGTTGTTATC-3'	
	WT R	5'-GAGCGGGAGAAATGGATATG-3'	
	DTA F	5'-CGACCTGCAGGTCCTCG -3'	
	DTA R	5'-CTCGAGTTTGTCCAATTATGTCAC-3'	

ADRP, adipose differentiation-related protein; **DTA**, diphtheria toxin A; **F**, forward; **mTmG**, Gt(ROSA)26Sor^{tm4(ACTB-tdTomato,-EGFP)Lox/J}; **R**, reverse; **R26**, Rosa26; **Tcf21**, transcription factor 21 ; **WT**, wild type.

Table 3. PCR programs for genotyping of transgenic mice

PCR	Temperature	Time	
Tcf21 ^{iCre} ;R26 ^{tdT} and mTmG	95 °C	3 min	
	95 °C	30 s	36x
	62 °C	60 s	
	72 °C	50 s	
	72 °C	5 s	
	4 °C	∞	
ADRP ^{CreERT}	95 °C	3 min	
	95 °C	20 s	40x
	56 °C	30 s	
	72 °C	35 s	
	72 °C	7 min	
	4 °C	∞	
R26 ^{DTA} (both mutant and WT)	94 °C	3 min	
	94 °C	30 s	35x
	60 °C	60 s	
	72 °C	60 s	
	72 °C	2 min	
	4 °C	∞	

3.4. Induction of lineage tracing and depletion of Tcf21^{lin}

A variety of tamoxifen injection schemes were employed to induce Cre recombination during lineage tracing and cell depletion experiments. Before injections, tamoxifen was dissolved in a mixture of medium-chain triglycerides (Miglyol 812, Caesar & Loretz, Hilden,

Germany) at 20 mg/ml. A detailed list of the tamoxifen dosing is provided for each of the employed mouse lines in table 4.

Table 4. Tamoxifen dosing schemes used in this work

Experiment	Condition	Injection [day(s)]	Tmx dose	Sacrifice day
Tcf21 lineage tracing	P1→P7	P1	0.2 mg	P7 or P14
	P1→P14	P1	0.2 mg	P14
	P7→P14	P7	100 mg/kg	P14
	Adult (Non-OP)	1–3	100 mg/kg/d	7
	Adult (sham or PNX)	Pre-OP3– Pre-OP1	100 mg/kg/d	Post-OP1, Post-OP3 or Post-OP7
Tcf21 ⁺ cell depletion	P1→P14	P1	0.2 mg	P14
	P7→P14	P7–P9	100 mg/kg/d	P14
	Adult (Non-OP)	1–3	100 mg/kg/d	7
	Adult (sham or PNX)	Pre-OP3– Pre-OP1	100 mg/kg/d	Post-OP7
ADRP lineage tracing	P1→P14	P1	0.2 mg	P14

ADRP, adipose differentiation-related protein; **d**, day; **non-OP**, non-operated; **P**, postnatal; **Post-OP**, postoperative; **Pre-OP**, preoperative; **Tcf21**, transcription factor 21.

3.5. Left pneumonectomy

3.5.1. Surgical intervention

For experiments involving pneumonectomy, 12 to 22-week old mice were employed. For any given experiment, the maximum age difference between the subjects was two weeks.

The surgical protocol used in this work was adapted from (Voswinckel 2004; Lechner et al. 2017). Briefly, mice were orotracheally intubated with a 20G plastic cannula connected to a MiniVent mechanical ventilator (Harvard Apparatus, Holliston, MA, USA). Promptly, ventilation was initiated at 100 strokes/min with a tidal volume of ~250 µl. The fur covering the surgical area was shaved and then, asepsis was performed with iodine.

A surgical incision was made between the skin covering the xiphoid appendix and the axillary ventral line. The chest was opened through the 5th intercostal space to allow access to the thoracic organs. Afterwards, the left lung and left hilus were identified. The left hilus was ligated with a titanium clip and the distal portion was cut. Promptly after, the entire left lung was excised carefully. The rib cage was then closed using a 5 – 0 silk suture while great care was taken to prevent pneumothorax formation. Finally, the skin surrounding the surgical wound was approximated and closed with tissue adhesive (Vetbond, 3M, USA); anesthesia was interrupted, and the subject was extubated upon regain of spontaneous breathing.

3.5.2. Anesthesia and pain management

Isoflurane was delivered with a vaporizer (VetEquip, USA) as intraoperative anesthetic (5% for induction, 2% for maintenance). Bupivacaine (Actavis, Germany) was administered intraoperatively as local anesthetic. Subcutaneous Buprenorphine (Bayer HealthCare AnimalHealth, Leverkusen, Germany) and Metamizol (in water; Sanofi-Aventis, Frankfurt am Main, Germany) were employed as perioperative analgesics.

3.5.3. Perioperative care

Upon induction of anesthesia, an ointment (Bepanthen; Bayer, Leverkusen, Germany) was applied on the mouse eyes to prevent desiccation and corneal ulcers. Mice were operated

on a warm pad to maintain physiologic temperature. In order to prevent potential volume loss, saline solution (NaCl 0.9% [w/v]) and 5% glucose (w/v) were injected subcutaneously to the mice.

3.6. Tissue processing for imaging of cryosections

After mice were sacrificed, the chest was open via sternotomy and the inferior vena cava and aorta were severed. Then, pulmonary vessels were perfused with phosphate-buffered saline (PBS) (~10 ml) injected through the right ventricle to flush erythrocytes out of the lung. After turning white due to exsanguination, lungs were inflated with a mixture of paraformaldehyde (PFA) 2% (w/v) in PBS and OCT compound 1:1 to fill the chest. Next, thoracic organs were removed *in toto* from the thorax, and incubated in fixative at 4 °C for 2 h. Fixed lungs were subsequently separated from the other thoracic organs before embedding.

Lungs were placed in cryomolds, embedded in OCT compound and frozen in dry ice-cooled isopentane to form cryoblocks, which were stored at -80 °C until sectioning.

Cryosections were generated using a CM3050 S cryostat (Leica, Wetzlar, Germany), mounted in slides and stored at -80 °C. Typically 10 µm sections were employed but occasionally 30 µm sections were stained and/or directly imaged. Cryosections for immunofluorescent labeling were stained as follows. Cryosections were first fixed with a mixture of cold (-20 °C) acetone and methanol (1:1) for 15 min. Blocking was performed with 5-50% goat serum diluted in 1× PBS containing 3% (w/v) BSA (bovine serum albumin) and 0.3% (v/v) Triton X-100 for 1 h. If needed, permeabilization was carried out with saponin 1% for 20 min at room temperature. Then, the sample was incubated with primary antibody diluted in 1× PBS containing 3% BSA and 0.3% Triton X-100. After incubation with primary antibodies, the sample was labeled with secondary antibodies diluted in the

same solution of 1× PBS with 3% BSA and 0.3% Triton X-100. Finally, 1× PBS with DAPI (2 μM) was added to the sections as counterstain for 5 min. Stained sections were mounted and then stored at 4 °C for further observation. Between steps, samples were rinsed with 1× PBS. the antibodies used and corresponding dilutions are listed in tables 5 and 6.

3.7. Design-based stereology

Design-based stereology was employed for unbiased evaluation of the lung structure in several experiments. Specimens were embedded in glycol-methacrylate (plastic) as described in the following paragraphs.

3.7.1. Lung Isolation and fixation

Post-operated adult mice were first sacrificed by overdose of anesthesia with isoflurane. Upon sacrifice, sternotomy was performed and the diaphragm was dissected from the ribs. At this point, the ribs of post-operated animals were laterally retracted to prevent unequal effects of the rib cage on the inflation of lungs of uneven volume since pneumonectomized (PNX) animals would have less lobes than sham mice. Then, the inferior vena cava and the descending aorta were severed, but no vascular perfusion was performed. Next, the lung was inflated and fixed with a solution containing 1.5% (w/v) PFA and 1.5% (w/v) glutaraldehyde in 150 mM 4-(2-hydroxyethyl)-1-piperazineethanesulfonic acid (HEPES)-PBS at a pressure of 20 cmH₂O with a blunt needle (21G for pups, 20G for adults). The hydrostatic pressure was maintained during fixation by ligating the trachea with a suture while removing the needle. Finally, the lungs were removed *en bloc* along with the rest of the thoracic organs and incubated at 4 °C for 24 h in the fixative used above for inflation.

3.7.2. Lung volume estimation

Fixed lungs from post-operated mice were separated from any other extrapulmonary tissue (including the trachea and main bronchi, effectively separating the left lung [LL] from the right lung [RL]), and any existing blood clots were removed from the surface of the organ.

The water displacement method was used to measure lung volumes. For experiments not involving PNx, the total lung volume (LL+RL) was measured. For the post-PNx experiments a more detailed record of the volume of the lobes was kept: The cardiac or accessory lobe (CL) was identified and dissected. In the process, three lung fractions were generated, namely LL, CL and the rest (nCL, for non-cardiac lobes), and the volume of each of these fractions was measured individually.

3.7.3. Embedding of lung tissue

Agarose 4% (w/v) was used to embed the lungs (or separate lung fractions) inside cubic molds and was then let to harden at 4 °C. Upon polymerization, agar blocks were sectioned into 3-mm slabs. Then, lung slabs from the different fractions studied were immersed in cacodylate buffer in separate snap-cap vials for further processing.

In a fume hood, lung tissue was prepared for embedding in glycol-methacrylate in the following manner: First, tissue was washed (4 × 5 min) with 0.1 M sodium cacodylate buffer prior to treatment with 1% (w/v) osmium tetroxide (OsO₄) dissolved in 0.1 M sodium cacodylate buffer, for 2 h. Next, the lungs were washed again with cacodylate buffer 4 × 5 min and then with ddH₂O 4 × 5 min. Lung slabs were then treated with half-saturated uranyl acetate buffer overnight, protected from light. Upon washing with double-distilled water (ddH₂O), dehydration of the tissue was carried out in a gradient of acetone from 70%

to 100% (v/v). After dehydration, the samples were exposed overnight to a 1:1 mixture of 100% (v/v) acetone and Technovit 7100-Hardener I and then to Technovit-Hardener I solution alone, again overnight; followed by incubation with Technovit 7100-Hardener I-Hardener II for 5 min under continuous rotation. Finally, lung slabs were transferred to Histoform Q molds in the same Technovit 7100-Hardener I-Hardener II mixture, which was allowed to polymerize for at least 48 h. Technovit 3040 mixed with Technovit universal liquid (~3:1) was employed to fix Histoblock adapters to the methacrylate-embedded tissue blocks. Block were then removed from the molds and stored before sectioning.

3.7.4. Preparation of the sections

Methacrylate blocks were sectioned to generate 2- μ m sections with a d-profile steel microtome knife (Leica, Wetzlar, Germany). Single sections were obtained every 20 μ m for a total of 4 sections (e.g. sections 1, 11, 21 and 31). Tissue sectioned this way was used to estimate most structural parameters except alveoli number. Number of alveoli was estimated using an additional pair of 2 μ m sections with a distance of 4 μ m (i.e. first and third sections). Upon collection of the tissue, slides were left to dry at 65 °C.

3.7.5. Staining of lung tissue for stereological analysis

Richardson's staining was performed on methacrylate slides to highlight the lung structure as follows: Sections were incubated Richardson's stain for 30 s at ~65 °C. Sections were sequentially washed in cold, hot, and double-distilled water. Finally, sections were fixed in Roti®-Histol (Carl Roth, Karsruhe, Germany) and allowed to dry before imaging.

3.7.6. Generation of digital images and estimation of structural parameters of the lung

Once stained, whole lung slides were scanned (10×, 20× and 40×) and digitized to virtual slides using a NanoZoomer-XR C12000 (Hamamatsu Photonics, Japan). Virtual slides were then imported for further analysis using the stereology module of the newCAST™ software (Visiopharm, Denmark).

3.8.7. Analysis of the lung structure

Quantitative assessment of the lung structure was performed using design-based stereology, following the recommendations emitted by the American Thoracic Society and the European Respiratory Society on the matter (Hsia et al. 2010).

3.9. Preparation of precision-cut lung slices from fixed organs

Thick mouse lung sections (or precision-cut lung slices, PCLS) were employed for 3D imaging of cells and tissue. The preparation of the PCLS was done as follows: First, the pulmonary vasculature of the animals was perfused *postmortem* with 1× PBS. The lungs were then inflated intratracheally to full capacity with low gelling temperature agarose (Merck, Steinheim, Germany) 4% (w/v) in 1× PBS containing 2% (w/v) PFA. The trachea was ligated to prevent leakage and the lungs were transferred to PFA 2% (w/v) in solution with 1× PBS. The lungs were allowed to fix for 24 h and then were transferred to 1× PBS. Then the separate lobes were embedded in blocks of regular agarose (Carl Roth, Karlsruhe, Germany) 1% (w/v) in 1× PBS and incubated at 4 °C until blocks became solid. Afterwards, blocks were cut into 150-300 µm slabs with a VT1200S vibratome (Leica, Wetzlar, Germany). Slabs were subsequently transferred to 1× PBS for storage until further use.

3.9.1. Labeling of the alveolar capillary network and preparation of PCLS from lectin-perfused fixed organs

When observation of the alveolar capillary network was necessary, the luminal membrane of the pulmonary vasculature of mice was labeled before organ harvest with fluorescent lectin. Once mice had been sacrificed and the lungs exposed as described above, the mice were intubated via tracheostomy with a G20 plastic cannula and connected to a MiniVent ventilator. Immediately after mechanical ventilation was initiated (ventilation pattern: ~175 μ l/stroke, ~200 breaths per minute), 100 μ l of DyLight649-conjugated *Lycopersicon esculentum* lectin were slowly infused into the right ventricle. The injected lectin was then allowed to circulate in the bloodstream through the pulmonary vessels aided by the inflation-deflation cycles of the ventilated organ. Five min after, ventilation was interrupted and the lungs were subsequently processed for preparation of PCLS as described above.

3.8.2. Immunofluorescent staining of PCLS

Generally, PCLS were stained with fluorescent probes as described next: Sections were washed 3 \times with 1 \times PBS before blocking with a solution containing 0.5% (w/v) BSA and 0.5% (v/v) Triton X-100. Incubation with primary antibodies (a list of the antibodies with their specific concentrations can be found in tables 5 and 6) was then carried out overnight at 4 °C followed by 3 washes with 1 \times PBS + 0,05% TWEEN® 20 (PBST). If necessary, sections were then labeled with secondary antibodies raised against the primary antibody's isotype. DAPI (2 μ M) was added to the secondary antibody solution (or directly-labeled primary antibody solution) if required as counterstain. Finally, three more washing steps were performed on the sections with PBST, which were then mounted on slides with fluoromount W (Serva, Heidelberg, Germany) using properly-sized spacers (SunJin Lab, Hsinchu, Taiwan).

3.8.3. Labeling of lipid droplets in PCLS with LipidTOX dyes

LipidTOX™ dyes (green or deep red, ThermoFisher Scientific, Waltham, USA) were used to stain neutral lipids in thick sections. LipidTOX was diluted 1:250 in PBS with 2 µM DAPI and then added to previously fixed and non-permeabilized PCLS. The sections were then incubated with LipidTOX for 30 min. Afterwards, sections were mounted using appropriate spacers.

3.8.4. Immunolabeling of PCLS

For several experiments PCLS were fluorescently stained with a variety of antibodies prior to confocal microscopy. The PCLS were first washed with 1× PBS and then incubated with blocking solution (5% [w/v] BSA and 0.5% [v/v] Triton X-100 in 1× PBS) for 1 h. After blocking, three 30 min washings with PBST were done. Afterwards, PCLS were incubated with the antibodies in a solution containing DAPI as nuclear stain (5% [w/v] BSA, 0.1% [v/v] Triton X-100 and 2 µM DAPI in 1× PBS) for 4 h. More washings were performed and lastly, the slices were mounted with appropriate spacers on microscope slides. Mounted slides were stored at 4 °C.

3.9. Flow cytometry

For analyses of pulmonary cell populations after pneumonectomy, lungs were digested with Dispase and dissociated mechanically to generate lung cell suspensions, which were analyzed by flow cytometry upon staining with fluorescently labeled antibodies. The detailed protocol for flow cytometry is described in detail in the following paragraphs. In general, when washing steps had to be performed, samples were centrifuged at 500 *g* during 10 min, after which supernatant was removed.

3.9.1 Organ isolation and preparation of single cell suspensions

Once the chest contents of mice had been exposed after euthanasia. The vena cava and descendant aorta were severed to allow exsanguination. Next, pulmonary vessels were perfused with Hanks' Balanced Salt solution (HBSS) injected through the right ventricle. The lungs were filled with Dispase (~50 caseinolytic units/ml) instilled via tracheostomy, which was then ligated to prevent leaks. Afterwards, the thoracic organs were removed, placed in a 12-well plate with ~1 ml Dispase (~50 caseinolytic units), in which the lungs were partially digested to facilitate further dissociation, afterwards, 40 to 45 min later, lungs were separated from other organs and transferred to gentleMACS C tubes containing Dulbecco's modified Eagle medium (DMEM) medium with 1% (v/v) HEPES, 1% (v/v) penicillin/streptomycin (P/S) and DNase I (0.2 mg/ml). Mechanical dissociation of the lungs was done with a gentleMACS™ dissociator (Miltenyi Biotec, Bergisch Gladbach, Germany) using pre-loaded programs (first m_lung_01_02 followed by m_lung_02.01). Cell suspensions were sequentially filtered through 100 µm and 20 µm cell strainers. Then samples were centrifuged, and the pellet resuspended in DMEM with 1% HEPES (v/v). When fixation of the cells was required, suspensions were incubated with Cytotfix™ Fixation Buffer (BD Biosciences, USA) for 15–20 min at 4 °C, washed with PBS and stained immediately or stored at 4 °C for further analysis.

3.9.2 Immunofluorescent labeling for flow cytometry

A list of the antibodies used and their corresponding dilutions is provided in tables 5 and 6. $1-2 \times 10^6$ fixed or live cells were transferred to FACS tubes prior to staining. For labeling of membrane-bound proteins, cells were washed and resuspended with Flow Cytometry Staining Buffer (Thermofisher Scientific, Waltham, USA). Then, cells were incubated with an excess of anti-CD16/CD32 antibody (1:100) for 5 min at 4 °C to block unwanted interactions between the other antibodies used and Fc receptors in the surface of certain cells. After blocking, cells were incubated with unconjugated or fluorophore-conjugated

primary antibodies for 15 min at 4 °C. If necessary, samples were subsequently incubated with fluorescently labeled secondary antibodies. Upon staining with antibodies, cells were resuspended in flow cytometry buffer for analysis. Prior to acquisition, DAPI (4 µM) was added to the samples for dead cell discrimination.

Single cell suspensions were analyzed either in a BD LSR II or LSRFortessa™ Cell Analyzer (both from BD Biosciences, Franklin Lakes, USA) using the software FACSDiva (BD Biosciences, Franklin Lakes, USA) during acquisition. If possible, in experiments that required the use of fluorophores with spectral overlap, compensation was carried out using single stained samples containing antibody-capture compensation microbeads (OneComp eBeads™, Thermo Fisher Scientific, Waltham, USA). Events positive for the various markers investigated were identified comparing fully stained samples with “fluorescence minus one” (FMO) controls. FMO controls contained all but one the fluorophores present in fully stained sample. Matched isotype controls were used as reference too whenever necessary. For example, for analysis of intracellular markers. After acquisition, FlowJo 10.x software (FlowJo, Ashland, USA) was utilized to generate flow cytometry plots and histograms, and for quantitative evaluation of populations of interest.

3.9.3 Immunofluorescent labeling of intracellular proteins for flow cytometry

Intracellular staining of cell suspensions was performed in some experiments along with staining for membrane markers. When that was the case, fixed cells were first stained with antibodies against membrane-bound proteins. Then cells were permeabilized with 1× Perm/Wash solution (BD Biosciences, San Jose, USA) for 15 min at 4 °C, washed and were finally incubated with primary antibodies for intracellular antigens. If necessary, secondary antibodies were employed afterwards. During intracellular staining, Perm/Wash solution was employed as a buffer for washing steps and for dilution of antibodies.

3.9.4. Fluorescent labeling of neutral lipids by flow cytometry

The neutral-lipid binding dye LipidTOX was used to detect lipid droplets in both tissue sections and in cell suspension. For flow cytometry HCS LipidTOX™ green or red neutral lipid stains (Thermo Fisher Scientific, Waltham, USA) were added to previously fixed cells in a 1:500 dilution. Samples with LipidTOX were incubated for 30 min at room temperature and then washed with PBS before acquisition.

3.10. Fluorescence-activated cell sorting

For *in vitro* experiments involving alveolosphere cultures, separation of various cell populations was necessary. In such cases, cell sorting was performed after fluorescent staining of mouse lung single cell suspensions. The staining was similar to that employed for flow cytometry but whole cell suspensions, as opposed to only fractions, were stained. Cell sorting was performed in a BD FACSAria™ II cell sorter (BD Biosciences, San Jose, USA). Antibodies used are listed with their respective concentrations in tables 5 and 6.

3.11. Co-cultures for generation of alveolospheres

Upon sorting, isolated cells were centrifuged (500 *g* for 5 min at 4° C) and then resuspended with alpha minimum essential medium (α -MEM) containing 10% (v/v) fetal calf serum, 100 U/ml penicillin, 0.1 mg/ml streptomycin, 2 mM L-glutamine, 1x insulin-transferrin-selenium and 0.0002% (v/v) heparin (alveolosphere medium). Relevant mesenchymal cell populations for each co-culture condition were mixed with AEC2 (CD24^{low}CD326^{int}) and then diluted 1:1 with cold growth factor reduced Matrigel™ (Corning, New York, USA). The final volume of each cell-Matrigel™ mixture was 90 μ l, which was poured over a 12 mm, 0.4 μ m-pore size cell culture insert (Merck, Steinheim, Germany). Next, inserts were placed inside of 24-well plates and Matrigel was allowed to polymerize for 5 min at 37 °C. Then, 350 μ l of alveolosphere medium were added to each

well to generate an air-liquid interface. Cultures were incubated at 37°C with 5% CO₂ for 14 days. Medium was changed three times per week. Cultures were observed and images were acquired with an EVOS™ FL Auto Imaging System (Thermo Scientific, Waltham, USA).

3.12. Image processing, analysis and preparation of figures

Images from brightfield whole-slide scans were captured with the NDPView2 software (Hamamatsu Photonics K.K., Hamamatsu City, Japan) and the newCAST software (Visiopharm, Hoersholm, Denmark) was used for stereological analyses of scans.

FIJI/ImageJ was used to perform adjustments of brightness and contrast to epifluorescent and confocal images as well as for generating 3D renderings and projections of Z-stacks.

Graphs were prepared with the software Prism (Graphpad Software Inc., v6–8.x) and with the data visualization package “ggplot2” for the R programming language. Figures were assembled using the GNU Image Manipulation Program (GIMP, v2.x) and Inkscape (v0.9x).

3.13. Statistics

Statistical analyses were performed on Prism v6–8.x or using the R programming language. Unless noted otherwise, data are presented as mean ± SD. Differences were evaluated with t-test (unpaired, unless noted otherwise) for comparisons between two groups. Differences between more than two groups were evaluated by one-way ANOVA with Tukey’s post hoc test. Normalized data about organoid number and diameter were log₂-transformed before statistical analysis was carried out. *P* values lower than 0.05 were considered to be statistically significant.

4. Materials

4.1. Equipment

Product

Agar-slicing molds
Analytical balance
Autoclave
Auto imaging system, EVOS™ FL
BD FACSAria™ II Cell sorter
Biosafety cabinet, class II
Cell culture incubator
Centrifuge 5430 R
Centrifuge, Multifuge 3 S-R
Chemical fume hood
Confocal microscope, LSM 710
Cooling ThermoMixer, HLC – MKR 13
Cryostat, CryoStar™ NX50
Cryotome, CM3050 S
Fluorescent microscope, DM6000 B
gentleMACS™ dissociator
Heating plate
Hybridization oven, PersonalHyb
Incubator, Heracell vios 160i
Insulin-Transferrin-Selenium, 100×|
Isoflurane Vaporizer
Laminar flow hood
LSR Fortessa
Magnetic stirrer
Microcentrifuge
Microcentrifuge, Heraeus™ Fresco™ 17
Microtome, RM2255
Mouse ventilator MiniVent Type 845
NanoZoomer 2.0-HT Slide scanner
Neubauer chamber, improved
Paraffin embedding station, EG 1160
PCR System, ProFlex
pH benchtop meter, SevenCompact Duo S213-meter

Manufacturer

Made in house
VWR International
Systec
Thermo Fisher Scientific
BD Biosciences
NuAire
Thermo Fisher Scientific
Eppendorf
Heraeus
Norddeutsche Laborbau
Carl Zeiss
Digital Biomedical Imaging Systems AG
Thermo Fisher Scientific
Leica
Leica
Miltényi Biotec
Medax
Stratagene California
Thermo Fisher Scientific
Thermo Fisher Scientific
VetEquip
NuAire, Inc.
BD Biosciences
Heidolph Instruments
Labnet International
Thermo Fisher Scientific
Leica
Harvard Apparatus
Hamamatsu Photonics K.K.
Paul Marienfeld
Leica
Thermo Fisher Scientific
Mettler Toledo

Pipettes, automatic: 10 µl, 100 µl and 300 µl	Eppendorf
Pipettes, manual: 10 µl, 100 µl 300 µl and 1 ml	Eppendorf
Pipettor, Easypet 3	Eppendorf
Real-Time PCR System, QuantStudio 3	Thermo Fisher Scientific
Reusable Knife, 16 cm, profile d steel assy	Leica
Spectrophotometer, NanoDrop® ND-1000	Thermo Fisher Scientific
Stereomicroscope, M50	Leica Byosystems
Surgical instruments (various)	F.S.T
Ultra Microtome, MX35	Thermo Fisher Scientific
Ultraviolet transilluminator/Gel imager	Intas
Vacuum Tissue Processor, ASP200 S	Leica
Vibratome, Leica VT1200S	Leica
Vortex mixer	IKA®-Werke
Water bath	VOGEL med. Technik & Elektronik

4.2. Reagents and drugs

Product	Manufacturer
2-Methylbutane	Carl Roth
4-Hydroxytamoxifen	Merck
4',6-Diamidino-2-Phenylindole (DAPI)	Thermofisher Scientific
Absolute Counting Beads, CountBright™	Thermofisher Scientific
Acetone	Carl Roth
Agar	Merck
Agar for embedding	Carl Roth
Agar for microbiology	Sigma-Aldrich
Agarose for embedding	Carl Roth
Agarose for inflation	Merck
Ampicillin sodium salt	Merck
Azure II	Merck
Bepanthen ointment	Bayer
Bovine Serum Albumin	Merck
Cacodylic acid·Na-salt·3H ₂ O	Serva
Citric acid monohydrate	Carl Roth
Compensating beads, OneComp eBeads	eBioscience Inc.
Cytofix™ Fixation Buffer	BD Biosciences
Deoxyribonuclease I	Serva
di-Sodium tetraborate, decahydrated	Carl Roth
Dispase	Corning

Dispase	Corning
DMEM, high glucose (4.5g/l), HEPES	Thermofisher Scientific
Dulbecco's phosphate buffered saline 10×	Merck
eBioscience™ Flow Cytometry Staining Buffer	Thermofisher Scientific
Ethanol ≥99,8 %	Carl Roth
Ethidium bromide solution 1 % (10 mg/ml)	Carl Roth
Fixation and Permeabilization Solution	BD Biosciences
Fixation Buffer	BD Biosciences
Flow Cytometry Staining Buffer	Thermofisher Scientific
Fluoromount W	Serva
L-glutamine	Merck
Glutaraldehyde 50 % solution in water 10 x 5 ml	Serva
Goat serum	Merck
Hardener II	Kulzer
HBSS 1x	Thermofisher Scientific
HCS LipidTOX™ Deep Red Neutral Lipid Stain	Thermo Fisher Scientific
HCS LipidTOX™ Green Neutral Lipid Stain	Thermo Fisher Scientific
Heparin-Sodium (5000 I.E./ml)	Braun
HEPES solution 1 M, pH 7.0-7.6	Merck
Hydrochloric acid (HCl)	Carl Roth
Hydrogen peroxide solution, 30%	Merck
Isofluran CP®, Isoflurane 1ml/ml	CP-Pharma
Isopropanol	Merck
Lidocain (10 mg/ml)	Braun
Lycopersicon Esculentum (Tomato) Lectin, DyLight 649-labeled	Vector Laboratories
Magnesium chloride (25 nM)	Thermo Fisher Scientific
Magnesium chloride (50 nM)	Thermo Fisher Scientific
Matrigel™ GFR Membrane Matrix	Corning
Mayer's hematoxylin solution	Merck
Metamizol, Novalgin® (drops. 500 mg/ml)	Sanofi
Methanol	Carl Roth
Methyl green	Vector Laboratories
Methylene blue	Carl Roth
Mowiol	Made in-house
Nuclease-free water	Ambion
Osmium tetroxide	Carl Roth
Paraffin, Paraplast®	Leica
Paraformaldehyde	Merck
Penicillin - Streptomycin for cell culture (100×)	AppliChem

Perm/Wash	BD Biosciences
Pertex™ mounting medium	Mediate
Phosphate buffered saline (1x and 10x)	Merck
Ringer tablets	Merck
Roti®-Histol	Carl Roth
Sodium hydroxide (NaOH)	Carl Roth
Sucrose ≥99.5 %	Merck
Tamoxifen	Merck
Technovit 7100	Morphisto
Technovit Universal Liquid	Kulzer
Technovit® 3040	Kulzer
Tissue-Tek O.C.T.™ Compound	Sakura Finetek
Tris-EDTA (TE) buffer	Thermo Fisher Scientific
Triton® X 100	Carl Roth
TWEEN® 20	Merck
Uranyl Acetate	Serva
Vetbond Tissue Adhesive	3M
Water for injection	Thermo Fisher Scientific

4.3. Consumables

Product	Manufacturer
Agar molds	Custom made
Cell Culture Insert, Millicell, 12 mm,	Merck
Cover slides	Carl Roth
Easystrainer 100 µM	Greiner bio-one
Easystrainer 40 µM	Greiner bio-one
Embedding cassettes, Rotilabo®	Carl Roth
FACS tubes	VWR
Filter pipette tips: 10 µl, 100 µl, 200 µl, 300 µl, 1 ml	Greiner bio-one
GentleMACS C tubes	Miltenyi Biotec
Histobloc® for Histoform S & Q	Kulzer
iSpacer® one well, 0.2 mm deep	SunJin Lab
iSpacer® one well, 0.5 mm deep	SunJin Lab
Microcentrifuge tubes: 0.5, 1.5 and 2 ml	Eppendorf
Pasteur pipette, 3.5 ml	Sarstedt
Peel-A-Way Disposable Embedding Molds	Polysciences, Inc.
Pipettes, serological: 2 ml, 5 ml, 10 ml, 25 ml, 50 ml	Falcon

Polyamide suture, SUPRAMID, unneeded
Safety Cannula, 20 G, Vasofix®
Silk Suture, PERMA-HAND™
SuperFrost™ Ultra Plus Adhesion slides
Syringes, Micro-Fine™+ 0.3 ml 0.30 mm (30G) x
8 mm
Technovit Histoform Q
Test tubes: 15 ml and 50 ml
Titanium Ligating Clips, Horizon™

Serag
B. Braun Melsungen
Ethicon
ThermoFisher Scientific
BD Biosciences
Morphisto
Greiner bio-one
Teleflex Incorporated

4.4. Primary antibodies

Table 5. Primary antibodies used in this work

Target	Applica- tion	Catalog number	Host	Conju- gate	Dilu- tion	Incubation conditions	Company	Isotype/ Format
ADRP	FC	ab201535	Rb	AF-488	1:100	30 min, 4°	Abcam	IgG
ADRP	IHF-Cryo	ab52356	Rb	none	1:100- 1:200	O.N., 4°	Abcam	IgG
ADRP	PCLS	ab52356	Rb	none	1:200	O.N., 4°	Abcam	IgG
CD16/32	FC	553141	Rb	none	1:100	20 min 4°	BD Biosciences	IgG2a, κ
CD31	FC	102407	Rt	PE	1:300	20 min 4°	BioLegend	IgG2a, κ
CD31	FC	102404	Rt	Biotin	1:100	15 min 4°	BioLegend	IgG2a, κ
CD326	FC	118204	Rt	Biotin	1:100	15 min 4°	BioLegend	IgG2a, κ
CD45	FC	103113	Rt	PE/Cy7	1:400	20 min 4°	BioLegend	IgG2b, κ
CD45	FC	103104	Rt	Biotin	1:100	15 min 4°	BioLegend	IgG2b, κ
EpCAM	FC	118208	Rt	FITC	1:200	20 min 4°	BioLegend	IgG2a, κ
Isotype	FC	400505	Rt	FITC	1:200	20 min 4°	BioLegend	IgG2a, κ
Isotype	FC	400507	Rt	PE	1:300	20 min 4°	BioLegend	IgG2a, κ
Isotype	FC	400512	Rt	APC	1:100	15 min 4°	BioLegend	IgG2a, κ
Isotype	FC	400617	Rt	PE/Cy7	1:400	20 min 4°	BioLegend	IgG2b, κ
Ki67	PCLS	14-5698- 82	Rt	none	1:200	O.N., 4°	ThermoFi- sher Scientific	IgG2a, κ
PDGFR- α	FC	135908	Rt	APC	1:100	20 min 4°	BioLegend	IgG2a, κ
RFP	IHC- paraffin	600-401- 379	Rt	none	1:300	O.N., 4°	Rockland Immunoche- micals	IgG
α-SMA	PCLS	F3777	Mo	FITC	1:200	O.N., 4°	Merck	IgG2A
α-SMA	PCLS	IC1420A	Mo	APC	1:50	O.N., 4°	R&D Systems, Inc.	IgG2A
SPC	IHF-Cryo	AB3786	Rb	none	1:500	O.N., 4°	Merck	Serum
SPC	PCLS	AB3786	Rb	none	1:500	O.N., 4°	Merck	Serum

FC, flow cytometry; **Rb**, rabbit; **Rt**, Rat; **Mo**, mouse; **PCLS**, precision-cut lung slices; **O.N.**, overnight; **IHF-Cryo**,

Immunohistofluorescence on cryosections.

4.5. Secondary antibodies and detection systems

Table 6. Secondary antibodies and detection systems used in this work

Target	Catalog number	Application	Conjugate	Dilution	Incubation conditions	Company
Biotin	405233	FC	SAv-Brilliant Violet 510™	1:300	20 min, 4°	Biolegend
Biotin	405235	FC	SAv-Alexa Fluor 488	1:300	20 min, 4°	Biolegend
Rb	A-21244	IHF-Cryo	Alexa Fluor 647	1:500	1h, RT	ThermoFisher Scientific
Rb	A-21244	PCLS	Alexa Fluor 647	1:500	4h, RT	ThermoFisher Scientific
Rb IgG	A-11008	IHF-Cryo	Alexa Fluor 488	1:500	1h, RT	ThermoFisher Scientific
Rb IgG	A-11008	PCLS	Alexa Fluor 488	1:500	4h, RT	ThermoFisher Scientific
Rb IgG	A-21428	IHF-Cryo	Alexa Fluor 555	1:500	1h, RT	ThermoFisher Scientific
Rb IgG	A-21428	PCLS	Alexa Fluor 555	1:500	4h, RT	ThermoFisher Scientific
Rt IgG	A-11006	IHF-Cryo	Alexa Fluor 488	1:500	1h, RT	ThermoFisher Scientific
Rt IgG	A-11006	PCLS	Alexa Fluor 488	1:500	4h, RT	ThermoFisher Scientific
Rt IgG	A-21247	IHF-Cryo	Alexa Fluor 647	1:500	1h, RT	ThermoFisher Scientific
Rt IgG	A-21247	PCLS	Alexa Fluor 647	1:500	4h, RT	ThermoFisher Scientific
Rt IgG	A-21434	IHF-Cryo	Alexa Fluor 555	1:500	1h, RT	ThermoFisher Scientific
Rt IgG	A-21434	PCLS	Alexa Fluor 555	1:500	4h, RT	ThermoFisher Scientific

FC, flow cytometry; **Sav**, Streptavidin; **Rb**, rabbit; **Rt**, rat; **PCLS**, precision-cut lung slices; **O.N.**, overnight; **IHF-Cryo**, Immunohistofluorescence on cryosections; **RT**, Room temperature.

5. Results

To study the phenotype and localization of Tcf21⁺ cells and the contribution of these cells to lung development, homeostasis and regeneration, the Tcf21^{iCre} Cre-driver was employed in combination with R26^{tdT} conditional reporter mice throughout this work. First, lineage labeling of Tcf21 was performed in adult Tcf21^{iCre/+};R26^{tdT/tdT} mice by inducing Cre-driven recombination with tamoxifen (Tmx) (Fig. 1A). After recombination is induced in this strain, Tcf21⁺ cells initiate expression of the fluorescent reporter tdTomato from the now constitutively active Rosa26 locus. Genetic recombination allows cells to continue expressing tdTomato, even following cell division or if the Tcf21 expression ceases, thus, achieving labeling of the Tcf21⁺ cell lineage.

5.1. Characterization of Tcf21⁺ cells in adult mice

Lineage labeling of Tcf21⁺ cells was performed in adult mice to investigate the phenotype in homeostatic conditions. To verify that expression of tdTomato in the lung is induced exclusively after Cre-driven recombination following Tmx administration, the lungs of adult Tcf21^{+/+};R26^{tdT/tdT} or Tcf21^{iCre/+};R26^{tdT/tdT} mice previously exposed to Tmx and Tcf21^{iCre/+};R26^{tdT/tdT} lungs not exposed to Tmx were observed (scheme is provided in Fig. 1B). As exemplified in Fig. 1C, while tdTomato fluorescence was clearly identified in lung cryosections from Tmx-exposed Tcf21^{iCre/+};R26^{tdT/tdT} mice, no tdTomato⁺ cells were found in Tcf21^{+/+};R26^{tdT/tdT} lungs after Tmx exposure. Similarly, no tdTomato⁺ cells were observed in Tcf21^{iCre/+};R26^{tdT/tdT} lung sections of mice unexposed to Tmx (Fig. 1D). The results from these experiments indicate that expression of tdTomato in Tcf21^{iCre/+};R26^{tdTomato} mice only follows Tmx exposure in presence of Cre-mediated recombination.

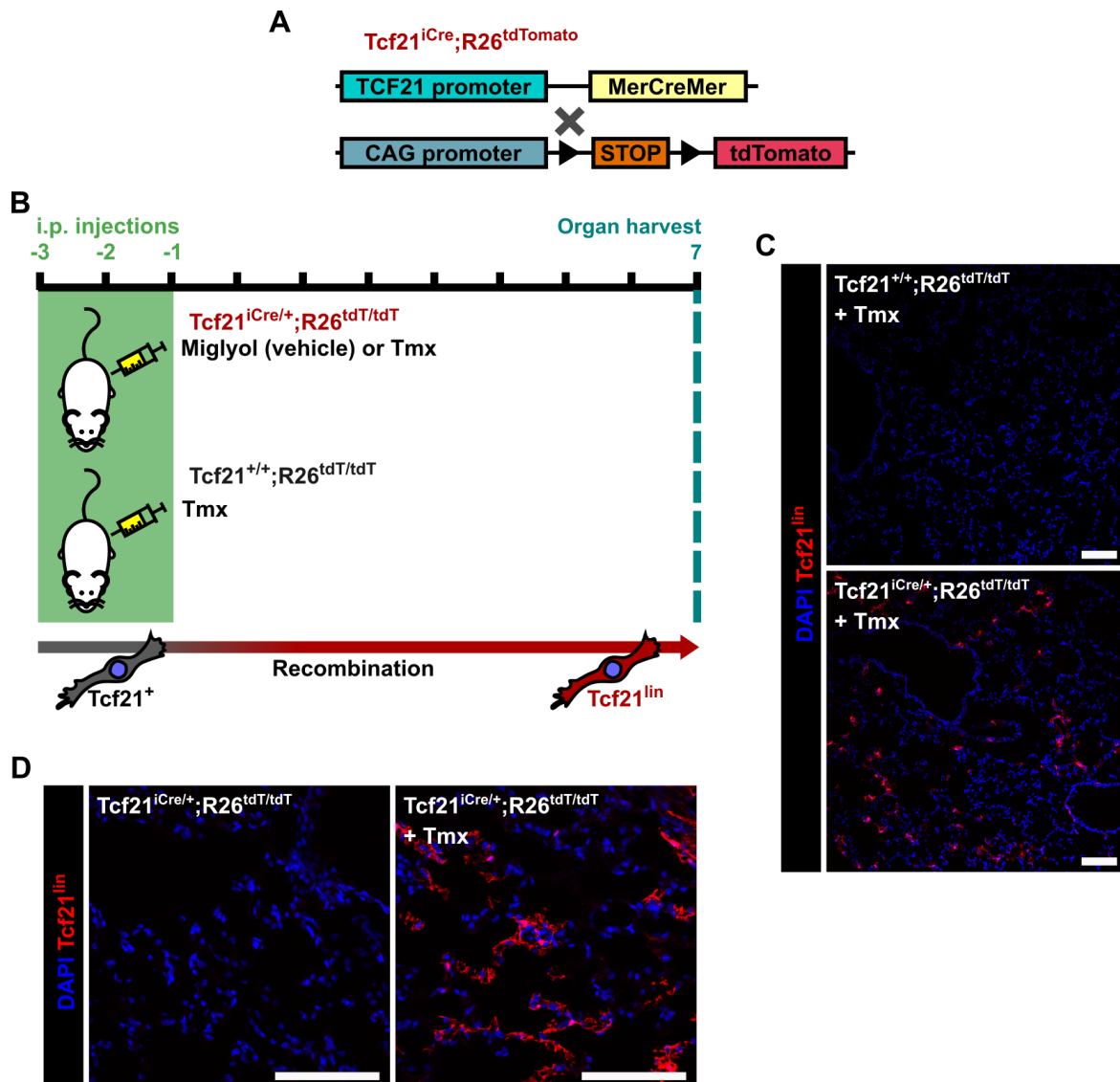


Figure 1. Induction of Cre-recombination in $Tcf21^{iCre/+};R26^{tdT/tdT}$ mice. **A.** $Tcf21^{iCre}$ mice were mated with $R26^{tdTomato}$ to generate $Tcf21^{iCre/+};R26^{tdT/tdT}$ inducible reporters. **B.** To induce Cre-driven recombination in $Tcf21^+$ cells, adult $Tcf21^{iCre/+};R26^{tdT/tdT}$ mice were injected with tamoxifen (Tmx, 100 mg/kg/d for three days), or not injected, to control for recombination in the absence of induction. Alternatively, $Tcf21^{+/+};R26^{tdT/tdT}$ mice were injected with the same dose of tamoxifen (Tmx) to verify the lack of tdTomato expression without Cre expression. **C.** While tdTomato⁺ cells were visible in $Tcf21^{iCre/+};R26^{tdT/tdT}$ cryosections upon induction with Tmx, tdTomato was not detected in $Tcf21^{+/+};R26^{tdT/tdT}$ mice. **D.** Cryosections show that tdTomato expression in $Tcf21^{iCre/+};R26^{tdT/tdT}$ mice is induced only after Tmx administration. Scale bars = 100 μ m. $Tcf21^{lin}$, Tcf21-lineage traced cells.

Upon induction of recombination in adult mice, Tcf21 lineage-traced cells ($Tcf21^{lin}$) were found scattered throughout the lung parenchyma (Figs. 1C-D, 2A). In this context, where recombination was induced in adult animals in absence of additional stimuli, $Tcf21^{lin}$ were assumed to be simply $Tcf21^+$ cells. $Tcf21^{lin}$ cells did not seem to be abundant but seemed

to occupy a comparatively large area in tissue sections (Figs. 1C-D, 2A). Analysis of $Tcf21^{iCre/+};R26^{tdT/tdT}$ lung sections immunohistochemically stained with anti-tdTomato antibody and Z-stacks from thick cryosections showed that the cell bodies of $Tcf21^{lin}$ cells are mostly located in the corners of alveoli (Fig. 2A) and emitted slender cytoplasmic processes that spanned the bases of alveoli (Fig. 2B). These processes were occasionally branched, sometimes contacted similar processes belonging to other $Tcf21^{lin}$ cells and could even form network-like structures with several neighboring tdTomato⁺ cells (Fig. 2C).

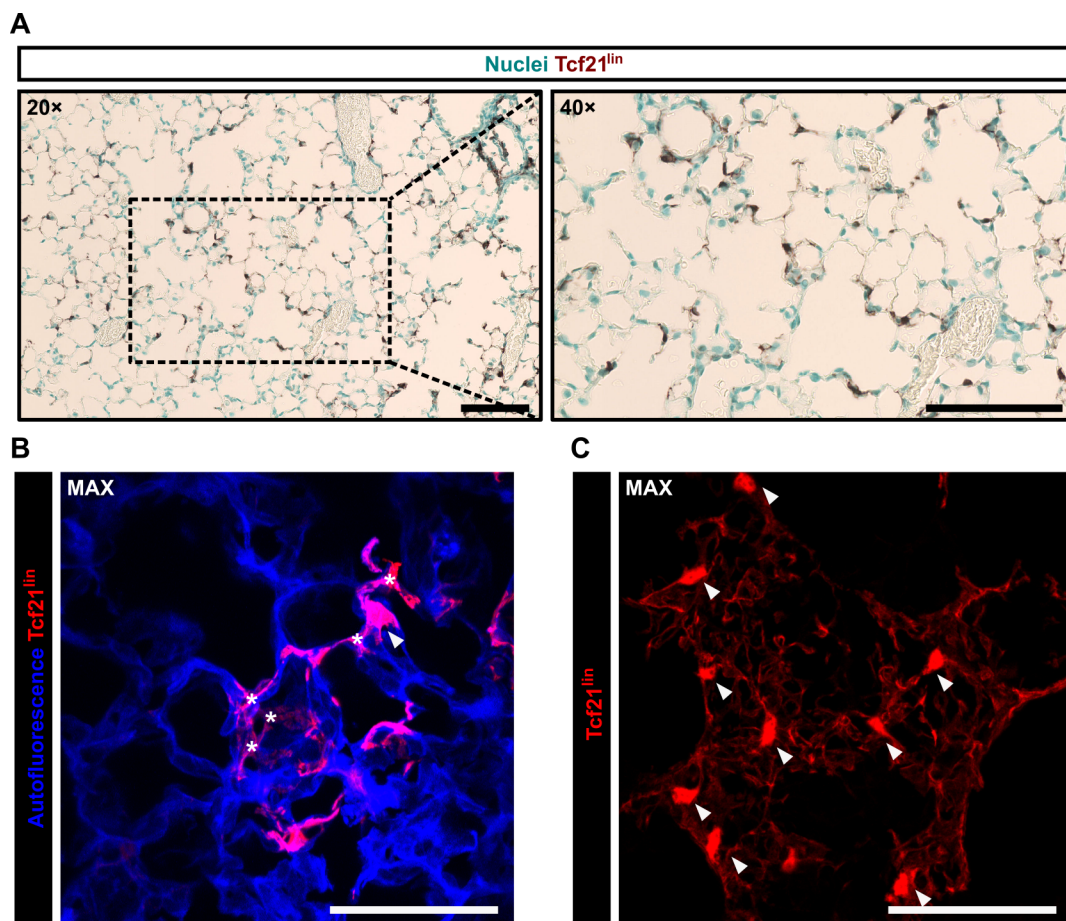


Figure 2. Spatial distribution of $Tcf21^{lin}$. **A.** Immunohistochemical staining of tdTomato in a $Tcf21^{iCre/+};R26^{tdT/tdT}$ lineage traced adult mouse. $Tcf21$ -lineage traced cells ($Tcf21^{lin}$) seem largely located in alveolar corners **B** and **C**. Maximum intensity projections (MAX) of adult $Tcf21^{iCre/+};R26^{tdT/tdT}$ mouse lung cryosections illustrating the 3D morphology of $Tcf21^{lin}$ **B**. $Tcf21^{lin}$ with long processes. **C.** Slender processes similar to that shown in B make contact with processes from neighboring $Tcf21^{lin}$. Arrowheads indicate the location of cell bodies. *Branching points of $Tcf21^{lin}$ processes. Scale bars = 50 μ m.

To characterize the phenotype of $Tcf21^{lin}$ cells in the lung, adult $Tcf21^{iCre/+}R26R^{tdT/tdT}$ lungs were dissociated into single-cell suspensions after lineage tracing induction. Then, cell suspensions were stained with various antibodies against several markers of different cell lineages. Analysis by flow cytometry upon CD140 (PDGFR- α), CD31 (platelet endothelial cell adhesion molecule, PECAM-1), CD45 and CD326 (Epithelial cell adhesion molecule, EpCAM) staining (for fibroblasts, endothelial, myeloid and epithelial cells, respectively) suggested that $Tcf21^{lin}$ cells were exclusively a subpopulation of mesenchymal cells, most of which had the signature $CD31^{-} CD45^{-} CD326^{-} PDGFR-\alpha^{+}$ (Fig. 3 and Appendix 2). The antibody panel used in this experiment included antibodies against CD31, CD45 and CD326 conjugated to identical fluorophores. Thus, improper function of any of these antibodies could have lead to misleading results. Therefore, some samples were individually stained for either CD31, CD45 or CD326, which upon analysis demonstrated that each of the antibodies targeting these markers could detect a population of cells, indicating the proper function of each of the antibodies tested (Appendix 2).

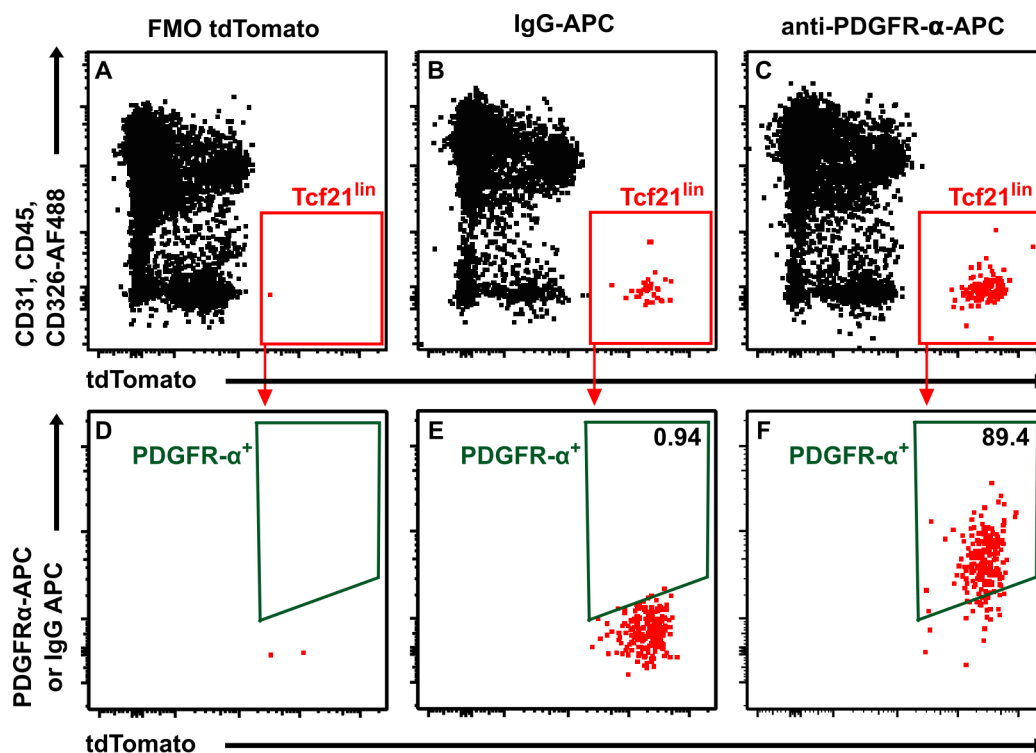


Figure 3. Tcf21^{lin} constitute a mesenchymal population primarily composed of PDGFR- α ⁺ cells in the adult mouse. Representative flow cytometry plots of single cell suspensions from Tcf21^{Cre/+};R26^{tdT/tdT} lineage traced adult mice stained with antibodies against CD31, CD45, CD326 and PDGFR- α or selected controls. Plots shown in **A**, **B** and **C** were generated after gating of live single cells and are derived from: **A**. tdTomato⁻ sample (“fluorescence minus one” [FMO] tdTomato; **B**. Tcf21^{Cre/+};R26^{tdT/tdT} sample containing an IgG-APC antibody instead of PDGFR- α antibody as isotype control; and **C**. Tcf21^{Cre/+};R26^{tdT/tdT} sample stained with anti-PDGFR- α -APC. Tcf21^{lin} events in **A-C** (which were found to be CD31⁻; CD45⁻ and CD326⁻), were then gated, demonstrating that most Tcf21^{lin} were additionally PDGFR- α ⁺ (**D-F**).

Next, the spatial relationship between Tcf21⁺ cells and the capillary bed of the lung parenchyma was investigated. To this end, lineage tracing of Tcf21^{lin} cells was performed in Tcf21^{Cre/+};R26^{tdT/tdT} adult mice and directly after sacrifice the lungs were perfused with fluorescently-labeled lectin (Lectin-Dylight 649) through the pulmonary vasculature, allowing for imaging of the alveolar capillary network. This lectin can bind vascular endothelium and its direct delivery into the circulation ensured that only the endothelium (and possibly, the lumen itself as well) would be labeled. Confocal imaging of these specimens revealed structures stained with Lectin-Dylight 649. While individual capillaries were difficult to distinguish in two dimensional (2D) sections, 3D imaging by means of maximum projection or 3D reconstructions allowed for easy identification of capillaries. The capillary bed could be observed, which was fenestrated by oval or polygonal capillary-free spaces. Around these spaces, loops of capillary segments interconnected, forming capillary networks. Qualitative analysis of confocal Z-stacks showed that the above described slender processes of Tcf21^{lin} cells seem to partially follow the outline of alveolar capillary loops. Sometimes, the tips of Tcf21^{lin} cell processes follow a portion of the capillary loop edge and end there or even, some of the tips may end in a circular hollow configuration that completely delineates the edge of capillary loops, forming a structure that resembles the shape of an inoculation wand tip or the eye of a sewing needle (Fig. 4).

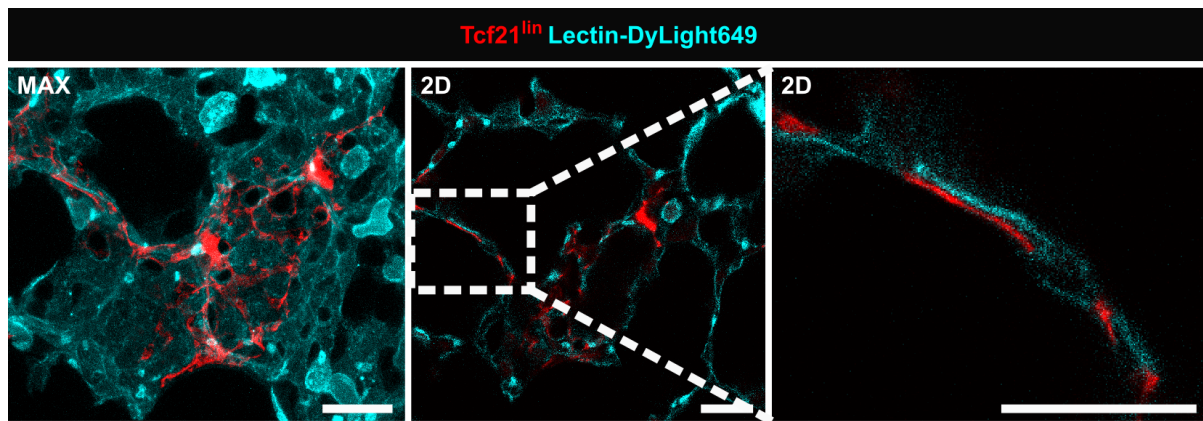


Figure 4. Confocal imaging of PCLS from a $Tcf21^{iCre/+};R26^{tdT/tdT}$ mouse labeled with fluorescently conjugated Lectin (Lectin-DyLight649). Maximum intensity projection (MAX) illustrates how the slender processes from $Tcf21$ -lineage traced cells ($Tcf21^{lin}$) follow the edge of capillary loops. Two-dimensional (2D) confocal sections illustrate the close proximity between $Tcf21^{lin}$ and the Lectin signal. Scale bars = 20 μ m.

5.2. Characterization of $Tcf21^{lin}$ cells during secondary alveolarization

The intact adult lung parenchyma does not exhibit significant growth; thus, adult mouse lung cells in homeostatic conditions display a slow turnover rate. Hence, the $Tcf21^{lin}$ phenotype described above in adult mice is assumedly present in non-proliferative conditions and in an environment that does not promote remodeling. To study the phenotype of parenchymal $Tcf21^{lin}$ in a more dynamic environment such as postnatal development, several features of $Tcf21^{lin}$ cells were identified through fluorescent techniques and quantified in 3D Z-stacks at P7, around the peak of secondary septation; and at P14, after the most intensive septation period had taken place. To induce recombination of the $Tcf21$ lineage during postnatal alveolarization, Tmx was administered i.p (100 mg/kg) at P1 or P7 and the lungs were isolated at P7 or P14 respectively as illustrated in Fig. 5.

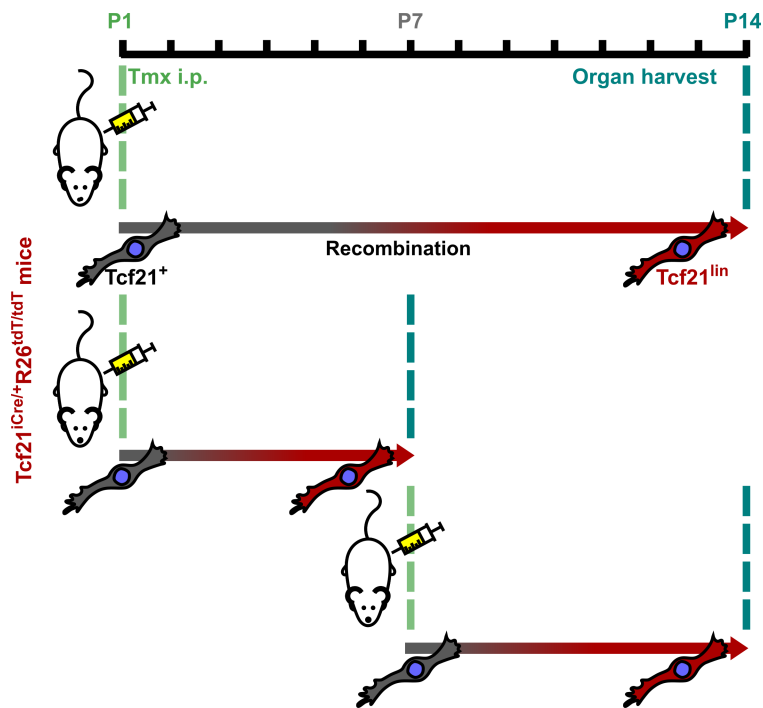


Figure 5. Induction of Cre-recombination for lineage tracing of Tcf21⁺ cells during postnatal alveolarization. Scheme illustrating the strategy followed to trace the Tcf21 lineage during postnatal alveolarization. Tcf21^{iCre/+};R26^{tdTomato} mice were injected with a single dose of tamoxifen (Tmx) either on the day of birth (postnatal day [P] 1; 0.2mg, i.p.) or at P7 (100 mg/kg, i.p.) to trigger Cre-induced recombination of Tcf21⁺ cells. Upon recombination, Tcf21-lineage traced cells (Tcf21^{lin}) express the fluorescent molecule tdTomato and can then be identified with fluorescent methods. Lungs were harvested at P7 or P14 from mice injected at P1 and on P14 from mice injected on P7.

Next whether Tcf21^{lin} display characteristics of fibroblasts was investigated. As identified by LipidTOX staining of PCLS, lipid droplets were found in the majority of Tcf21^{lin} cells at both P7 and P14 (Fig. 6). Consistently, ADRP which is characteristically located on lipid droplets surface, was also observed in most Tcf21^{lin} cells from P7 and P14 lungs by immunohistofluorescence (Fig. 7). Upon Pro-SPC staining at P7 and P14, parenchymal Tcf21^{lin} were frequently found to be in contact with SPC⁺ cells (Fig. 8A). Not only were Tcf21^{lin} cell bodies often adjacent to SPC⁺ cells as shown for lipofibroblasts in previous works but Tcf21^{lin} cell processes were also found contacting SPC⁺ cells at different places along the processes' length. Commonly, a Tcf21^{lin} would contact more than one neighboring SPC⁺ cell (Fig. 8B). Taking this features into account, It was estimated that over 90% of the parenchymal Tcf21^{lin} contacted SPC⁺ cells at both P7 and P14 (Fig. 8C).

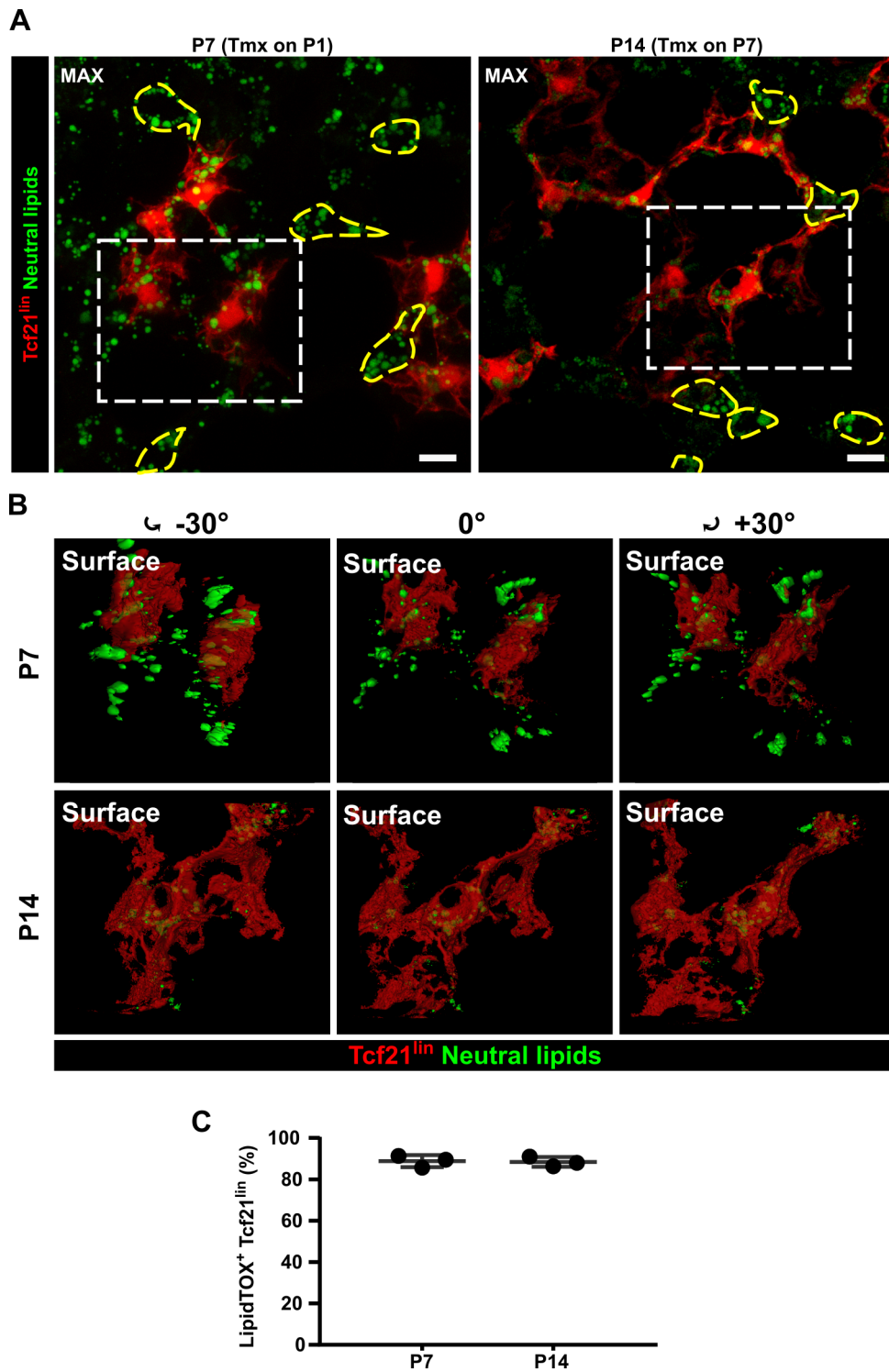


Figure 6. Neutral lipid droplets are highly prevalent in Tcf21^{lin} cells during late lung development. Confocal imaging of Precision-cut lung slices (PCLS) from Tcf21^{Cre/+};R26^{tdT/tdT} mice labeled with the neutral lipid dye LipidTOX. **A.** Neutral lipid droplets were visible within many Tcf21-lineage traced cells (Tcf21^{lin}) at both postnatal day (P) 7 and P14. Of note, some cells other than Tcf21^{lin} also contained lipid droplets. **B.** Surface renderings of the regions enclosed within white dashed lines in A, viewed from different angles. Cells at both timepoints confirm that lipid droplets are localized within Tcf21^{lin}. **C.** Manual quantification revealed that similarly large numbers of Tcf21^{lin} contained lipid droplets at P7 and P14. Error bars represent mean ± SD. n = 3 per group. Groups were compared with an unpaired Student's t-test. Scale bars = 10 μm. Tmx, tamoxifen.

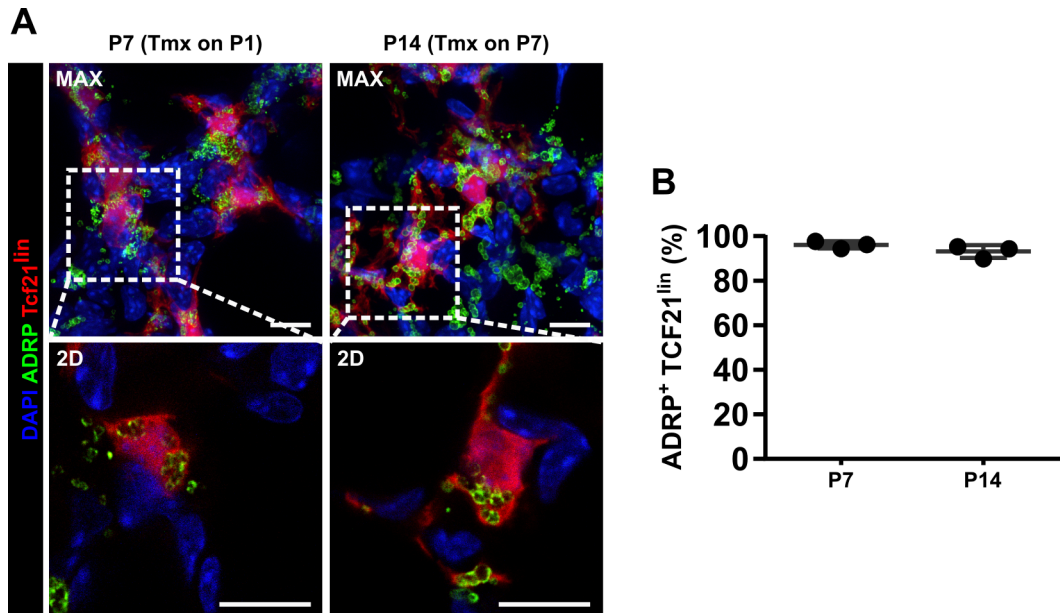


Figure 7. Tcf21^{lin} cells express the lipid droplet binding protein ADRP during late lung development. Confocal imaging of precision-cut lung slices (PCLS) from Tcf21^{iCre/+};R26^{tdT/tdT} mice stained with an anti-ADRP antibody. **A.** Maximum projections of sections (top) and two-dimensional (2D) images (bottom) from postnatal day (P) 7 and P14 lungs show Tcf21-lineage-traced cells (Tcf21^{lin}) containing clusters of spheroid-shaped Adipocyte differentiation-related protein (ADRP)⁺ structures (assumedly lipid droplets). Some tdTomato⁻ cells were also found to stain for ADRP. **B.** Manual quantification of the proportion of ADRP⁺ cells among Tcf21^{lin}. Most Tcf21^{lin} were found to be ADRP⁺ at both P7 and P14. Error bars represent mean ± SD. n = 3 per group. Groups were compared with an unpaired Student's t-test. Scale bars = 10 μm. Tmx, tamoxifen.

Even though lineage tracing experiments shown above indicate that nearly all Tcf21^{lin} express ADRP, the presence of some ADRP⁺tdTomato⁻ was appreciable. This observation might be expected if Tcf21 were expressed by only a subpopulation of lipofibroblasts or due to incomplete recombination of the Tcf21⁺ cell population if Tcf21 were expressed in the majority of lipofibroblasts. To further analyze this, it was assessed how lipofibroblast labeling of the Tcf21^{iCre} mouse differs from that of an inducible Cre driver strain of a “classic” lipofibroblast molecular marker. Thus, Tcf21 lineage labeling in Tcf21^{iCre/+}R26^{tdT/tdT} mice was compared to that of the ADRP lineage in ADRP^{CreERT/+};R26^{mTmG/+} mice at P14 upon P1 induction. In ADRP^{CreERT/+};R26^{mTmG/+} mice, cells recombined after Tmx exposure switch the constitutive expression of tdTomato, for GFP. tdTomato⁺ cells from Tcf21^{iCre/+};R26^{tdT/tdT} mice injected with tamoxifen at day 1 where comprised almost exclusively of

ADRP⁺ cells at P14. On the other hand, ADRP lineage-traced cells (ADRP^{lin}) from ADRP^{CreERT/+};R26^{mTmG/+} mice induced in a similar manner, contained a high percentage of ADRP⁻ cells. Results of this experiment demonstrated that the specificity of the Tcf21 lineage for the ADRP⁺ cell population is much higher than that of the ADRP lineage after the peak of secondary septation and suggest that a large portion of ADRP-expressing cells present immediately after birth lose ADRP expression by P14 (Fig 9).

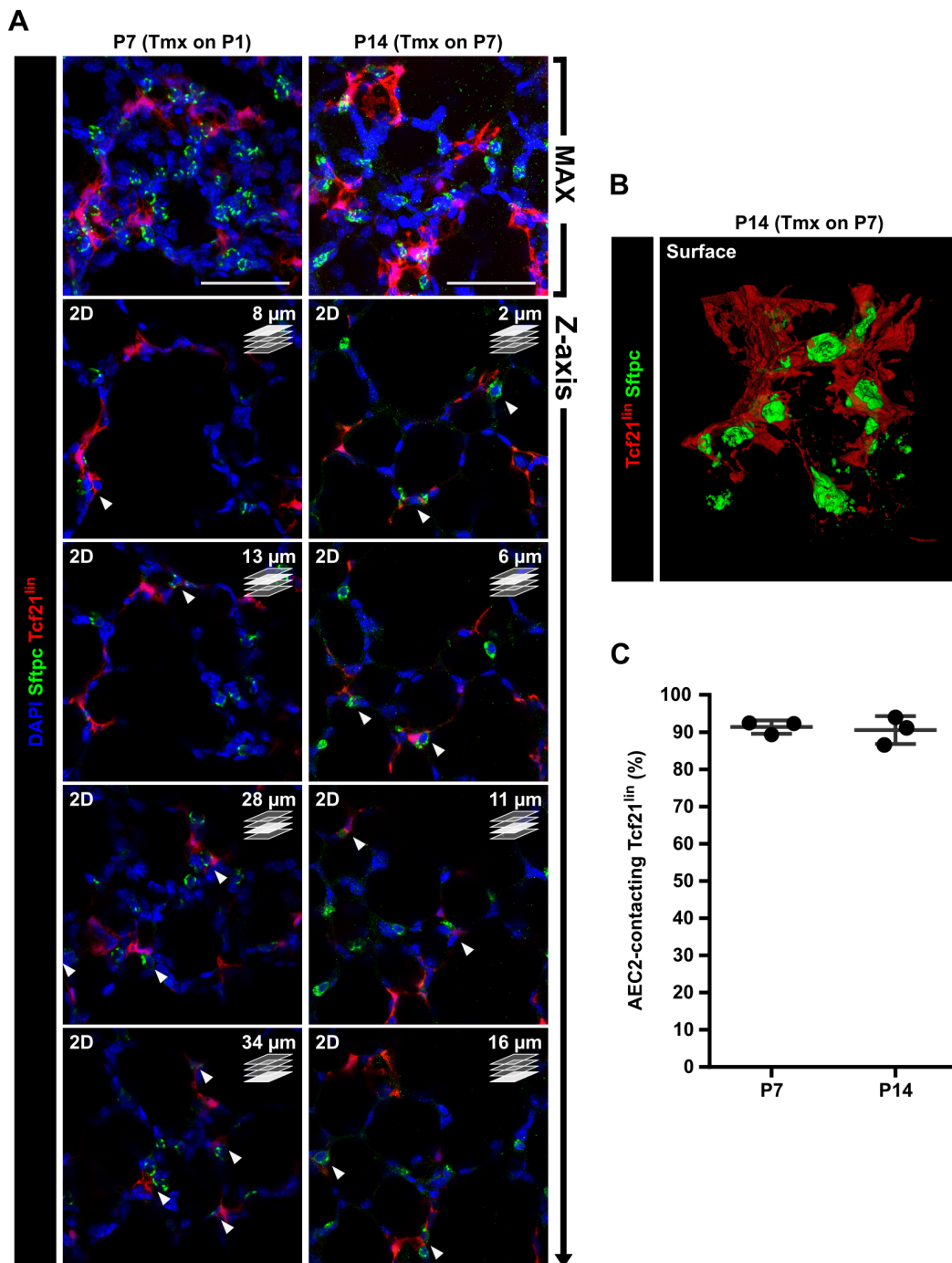


Figure 8. Tcf21^{lin} cells maintain close contact with alveolar type 2 cells during alveolarization. Lung precision-cut lung slices (PCLS) from postnatal day (P) 7 and P14. Tcf21^{Cre/+};R26^{tdT/tdT} mice were fluorescently stained with an anti-SPC antibody and imaged with a confocal microscope to evaluate the spatial relationship between Tcf21-lineage traced cells (Tcf21^{lin}) and alveolar type 2 cells (AEC2). **A.** Maximum intensity projections (MAX) of confocal Z-stacks show that TCF21^{lin} appear to be close to AEC2 at both P7 and P14. Two dimensional (2D) images obtained from the same Z-stacks at different depths — indicated in the upper-right corner of each image — reveal that Tcf21^{lin} contact AEC2 at both P7 and P14. **B.** Surface rendering of a Z-stack at P14 illustrates that single Tcf21^{lin} may contact several AEC2 cells. **C.** Comparison of the percentage of Tcf21^{lin} contacting AEC2 on P7 and P14 estimated manually in Z-stacks. The majority of Tcf21^{lin} were found to contact AEC2 at both timepoints. Error bars represent mean \pm SD. n = 3 per group. Groups were compared with an unpaired Student's t-test. Scale bars = 50 μ m.

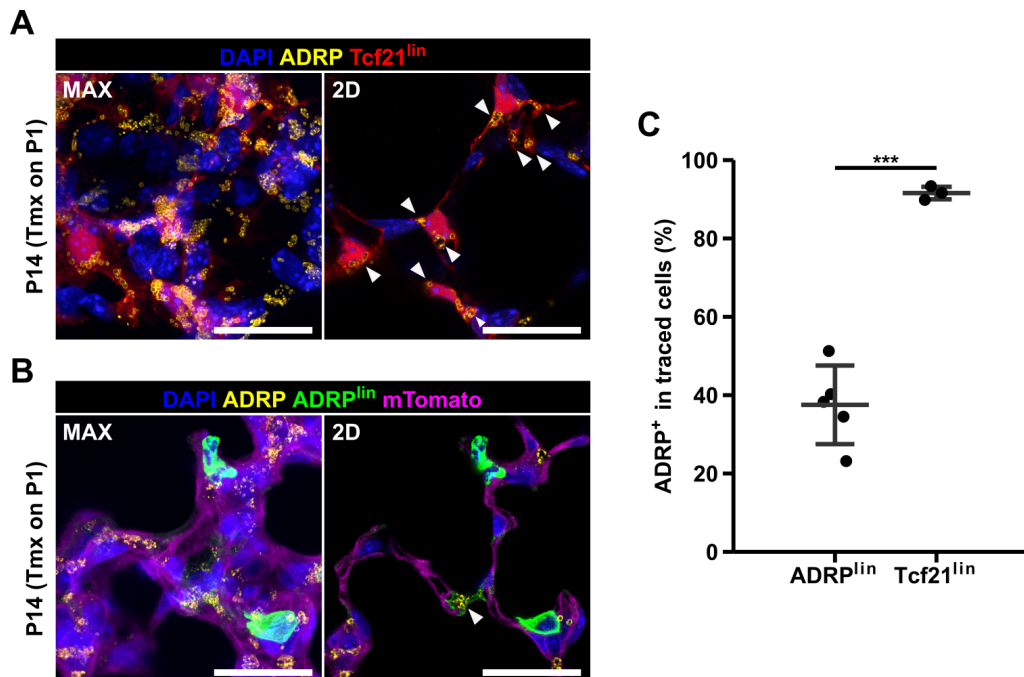


Figure 9. Early postnatal lineage tracing of Tcf21 results in more specific labeling of ADRP-expressing cells after the peak of secondary septation than ADRP lineage labeling. Confocal imaging of PCLS from Tcf21 lineage-traced (Tcf21^{lin}) cells (**A**) and ADRP lineage-traced (ADRP^{lin}) cells (**B**) at P14 upon P1 induction. In A and B, images at the left are maximum projections (MAX), while at the right, images represent two-dimensional (2D) planes. **C.** Comparison of the fraction of ADRP⁺ cells within the ADRP^{lin} populations. Arrowheads indicate ADRP⁺ profiles found inside ADRP^{lin} cells. Error bars represent mean \pm SD. n = 3–5 per group. Groups were compared with an unpaired Student's t-test ($***P \leq 0.001$). Scale bars = 25 μ m. Tmx, tamoxifen.

To evaluate turnover potential of Tcf21⁺ cells during secondary alveolarization, proliferation rate of Tcf21^{lin} was assessed with an immunofluorescent staining against Ki67 in PCLS. As expected for a rapidly growing organ, Ki67⁺ nuclei were found throughout the lung parenchyma at both P7 and P14. At P7, some Tcf21^{lin}Ki67⁺ cells were observed (10.6% \pm 1.9%); however Tcf21^{lin}Ki67⁺ cells were virtually absent by P14 in animals in which

recombination was induced at P7 ($0.2\% \pm 0.2\%$, $P < 0.001$). This result indicates that the expansion displayed by the Tcf21 lineage around the peak of secondary septation decreases dramatically by the time such peak is over (Fig. 10).

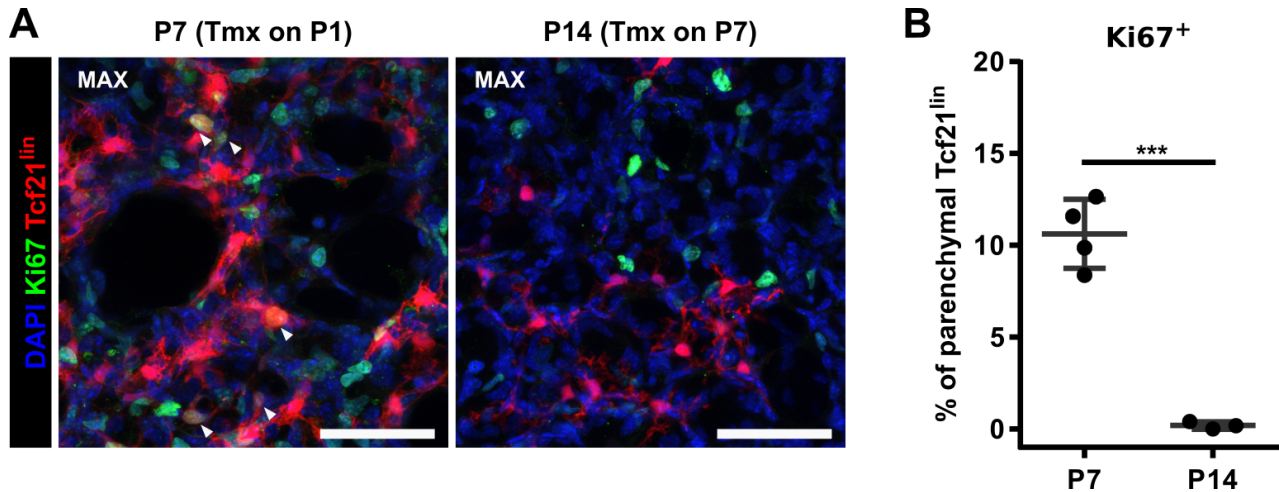


Figure 10. Proliferation of Tcf21^{lin} cells during secondary alveolarization. Confocal imaging of precision-cut lung slices (PCLS) from Tcf21^{Cre/+;R26^{tdT/tdT}} mice stained with anti-Ki67 antibody. **A.** Maximum projections (MAX) of tissues at postnatal day (P) 7 (left) and P14 (right) show Ki67⁺ cells in the lung parenchyma. At P14, proliferative Ki67⁺ cells included some Tcf21^{lin}. In contrast, at P14, overlap of the Ki67 and Tcf21^{lin} signals was negligible. **B.** Manual quantification of the proportion of Ki67⁺ cells among Tcf21^{lin}. While ~10% of Tcf21^{lin} stained for Ki67 at P7, Ki67⁺ Tcf21^{lin} were virtually absent at P14. Error bars represent mean \pm SD. $n = 3-4$ per group. Groups were compared with an unpaired Student's *t*-test (***) $P \leq 0.001$). Scale bars = 50 μ m. Tmx, tamoxifen.

Next, experiments were performed to investigate whether Tcf21^{lin} could give rise to myofibroblasts that appear during secondary septation. For this, lineage tracing of Tcf21⁺ cells was induced on either P1 or P7, and the lungs from lineage-labeled animals were harvested on P7 or P14 and analyzed by confocal microscopy upon α -SMA immunostaining. Remarkably, at each of the assessed time points less than 1% of Tcf21^{lin} shown to be α -SMA⁺, indicating that the Tcf21 lineage does not directly contribute significantly to the generation of myofibroblasts during secondary septation (Fig. 11).

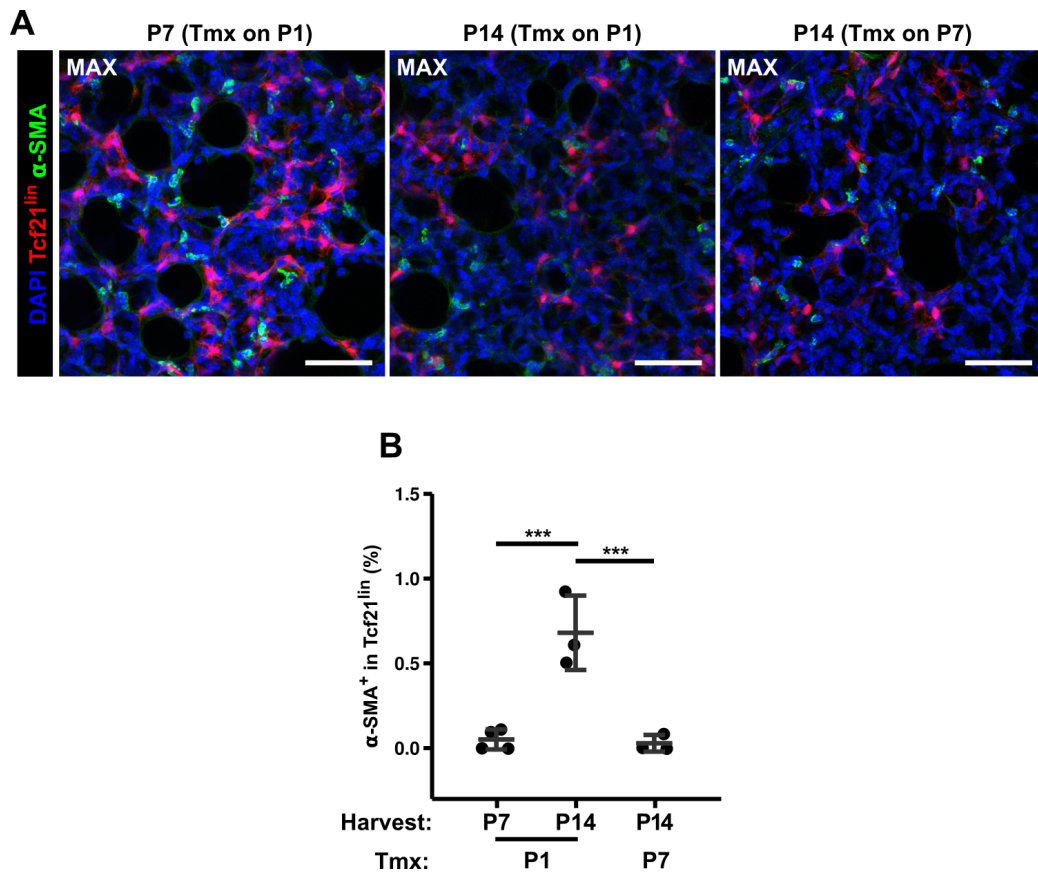


Figure 11. A very small proportion of Tcf21^{lin} cells contribute to the myofibroblast pool during secondary septation. A. Maximum projections (MAX) of anti- α -SMA-stained Tcf21^{Cre/+};R26^{tdT/tdT} lungs at either postnatal day (P) 7 or P14 after recombination at P1 or P7. **B.** Comparison of the fraction of α -SMA⁺ cells within the Tcf21^{lin} population in lung tissue. A negligible proportion of Tcf21^{lin} were shown to be α -SMA⁺. Error bars represent mean \pm SD. $n = 3\text{--}4$ per group. Differences between groups were evaluated by one-way ANOVA with Tukey's post hoc test ($***P \leq 0.001$). Scale bars = 50 μ m. Tmx, tamoxifen.

5.3. Validation of compensatory regrowth after pneumonectomy

The post-pneumonectomy compensatory regrowth is a useful model for studying *de novo* formation of alveoli in a lung that is already mature and in a non-inflammatory context. Thus, the phenotype of the Tcf21 lineage in this model was characterized and the impact of Tcf21⁺ cell depletion on *de novo* alveoli formation was investigated. Even though the occurrence of lung regrowth in several animal species (including rodents) is well established and documented by multiple authors (Voswinckel 2004; Fehrenbach et al. 2008; Hsia 2004), it was important to demonstrate that the specific protocol employed here indeed leads to compensatory growth of the remaining lung. Because of this, the left PNx

model was validated using an stereological analysis to evaluate the post-operative growth of lungs of wild-type C57BL6/J adult mice.

In concordance with previous reports, compensatory regrowth could be observed in PNx mice as evidenced by higher estimates of lung volume and total number of alveoli in the PNx group compared to sham mice by postoperative day (Post-OP) 7 (Fig. 12).

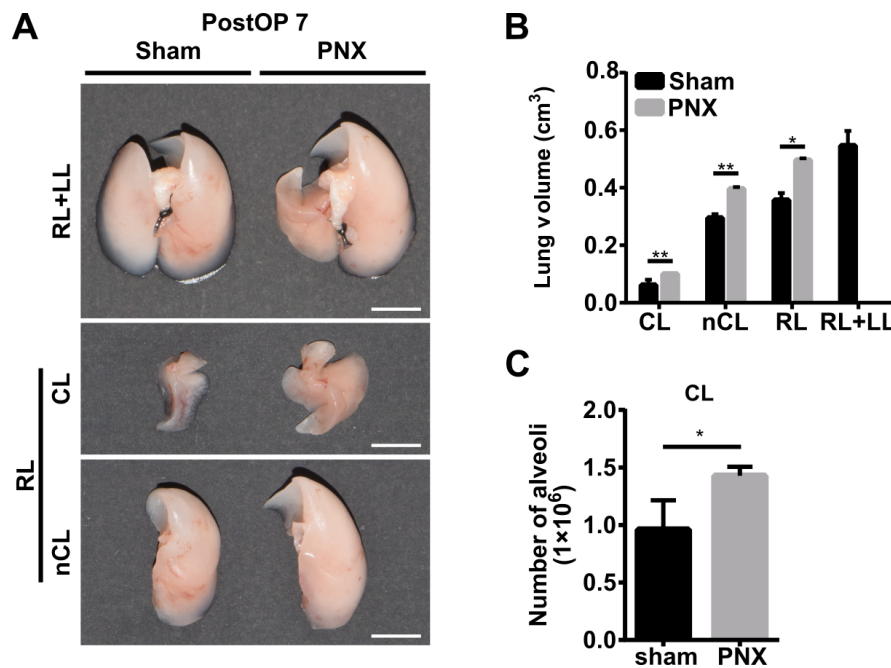


Figure 12. Validation of the post-pneumonectomy compensatory regrowth model. In order to confirm the validity of the compensatory regrowth model used in this work for studying neo-alveolarization, lungs of C57BL/6J wild-type mice that had undergone either sham or left pneumonectomy (PNx) procedures were analyzed using stereological methods at post-operative day 7 (Post-OP 7). **A.** Representative macroscopic images of sham and PNx right lungs. Top panels show the entire organ except for the previously excised left lobe (LL) of the PNx mouse while the middle and bottom panels show elements of the right lung (RL) (namely cardiac lobe [CL] and the rest of the lobes [nCL], respectively). PNx right lobes, specially the CL were evidently larger than those of sham controls. **B.** Stratified analysis of the volume of lung lobes after pneumonectomy. The volume of the RL from PNx mice was significantly higher than that of sham mice, as was the cardiac lobe volume and the compound volume of the other 3 lobes in the right lung (nCL, for non-Cardiac lobes). For reference, the total lung volume of sham mice including RL and LL is included in the graph. **C.** Comparison of the absolute number of alveoli in CL between sham and PNx mice estimated using the physical disector method. PNx CL had significantly more alveoli than sham CL did, indicating that neo-alveolarization had occurred in PNx lungs. Error bars represent mean \pm SD. $n = 3$. Sham and PNx groups were compared with an unpaired Student's t-test (* $P \leq 0.05$, ** $P \leq 0.01$). Scale bar = 5 mm.

5.4. Characterization of Tcf21^{lin} during compensatory regrowth

To characterize the phenotype of Tcf21⁺ cells during neo-alveolarization, Tcf21 lineage-tracing experiments were performed on either PNX-operated mice and sham-operated controls as described in Fig. 13.

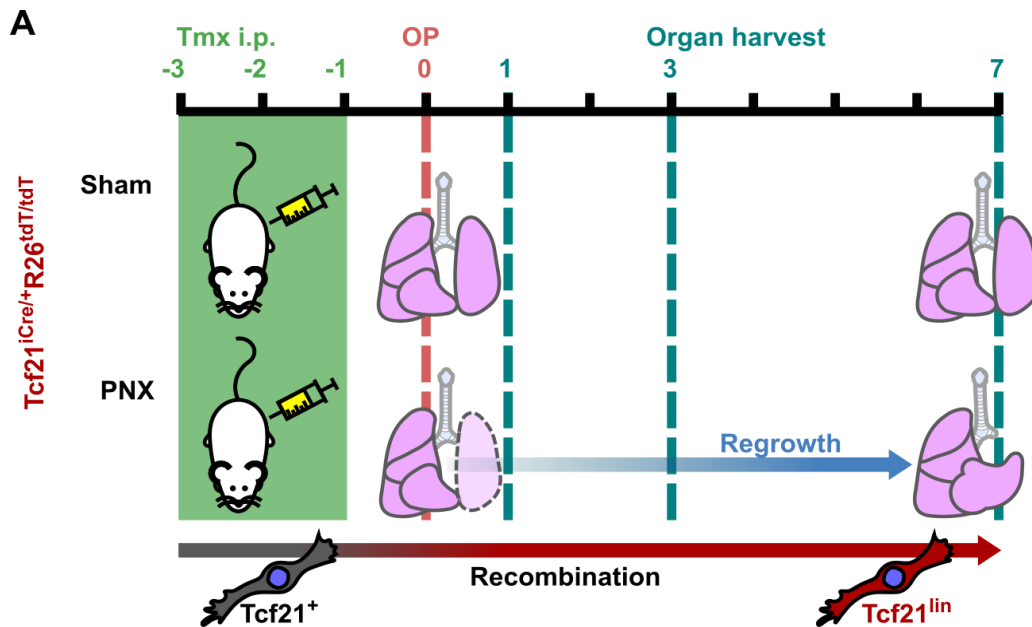


Figure 13. Experimental workflow for the study of the Tcf21 lineage during compensatory regrowth. Scheme illustrating the strategy followed to trace and study the Tcf21 lineage during regrowth. Cre-recombination of Tcf21⁺ cells was triggered in adult Tcf21^{iCre/+};R26^{tdT/tdT} mice with tamoxifen (Tmx) injected during three consecutive days (100 mg/kg/d, intraperitoneal [i.p.]). One day after the last injection, mice underwent sham or left pneumonectomy (PNX) operations (OP). The lungs of operated mice were then harvested on post-operative days 1, 3 or 7 for analysis of Tcf21 lineage-traced (Tcf21^{lin}) cells.

Analogous to the previously presented observations made in non-operated mice, Tcf21^{lin} cells were also found in the lung parenchyma of PNX and sham mice on days Post-OP 1, 3 and 7 (Fig. 14 and not shown). Flow cytometry analysis of cardiac lobe cell suspensions of PNX-operated mice showed that, during regrowth, Tcf21^{lin} cells are primarily mesenchymal cells that preserve the phenotype CD31⁻CD45⁻CD326⁻PDGFR- α ⁺ (Fig. 15). Confocal imaging of cryosections upon anti-SPC staining showed that Tcf21^{lin} cells preserve close spatial relationship with AEC2 (Fig. 16A). After, PNX LipidTOX-stained lipid droplets were commonly found in both sham and PNX operated mouse lungs; and

consistently, ADRP⁺ foci were found inside of lineage-traced cells (Fig. 16B and C). Using flow cytometry, no significant differences were found in the relative number of Tcf21^{lin} cells that expressed ADRP or captured LipidTOX between sham and the PNX groups at Post-OP 7 (Fig. 16D and E); however, the percentage of cells stained using these two lipid-related markers was in both cases over 90%. Taken together, these results suggest that upon PNX: 1) Tcf21^{lin} have for the most part a similar localization to that in (non-operated and sham) mice, and 2) Tcf21^{lin} preserve lipofibroblast-like characteristics during compensatory regrowth.

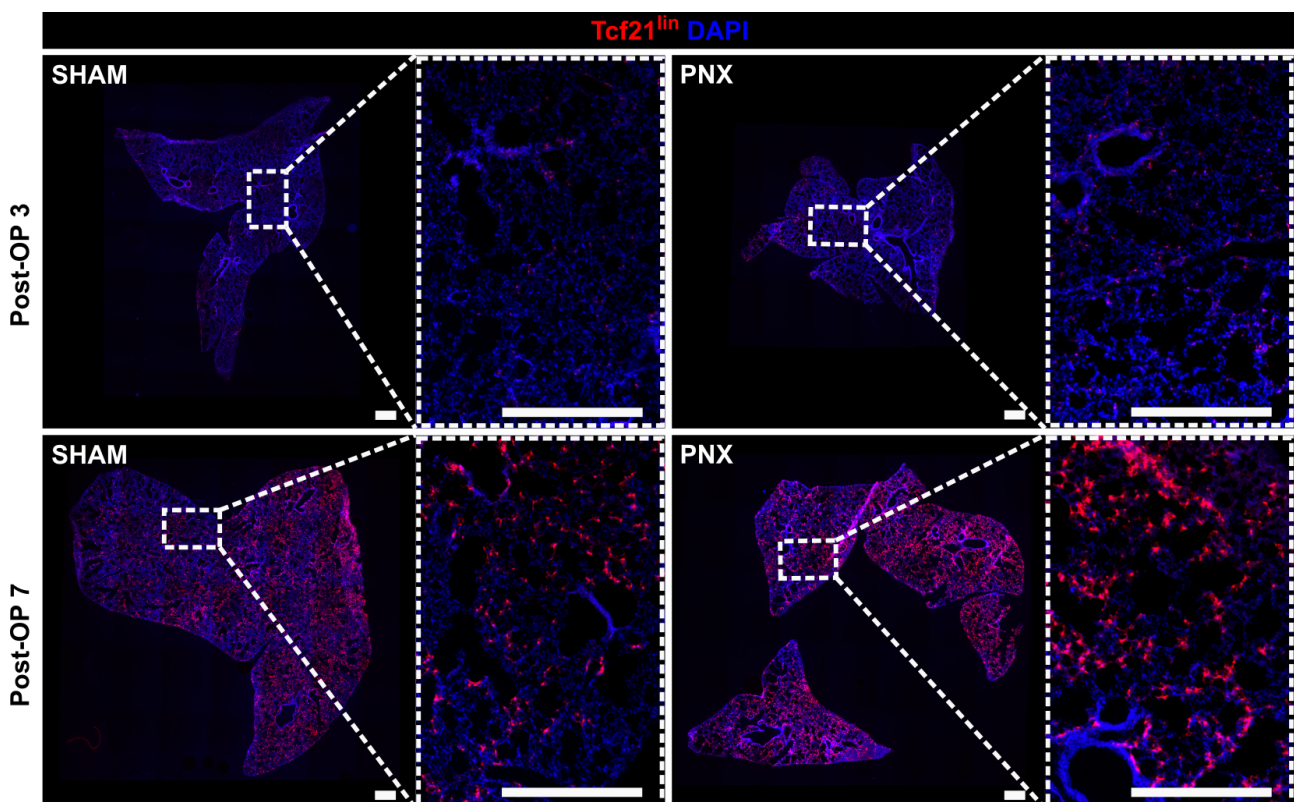


Figure 14. Pulmonary Tcf21^{lin} cells are localized to the lung parenchyma in both sham and pneumonectomized mice. Full-section scans of Tcf21^{iCre/+};R26^{tdT/tdT} mouse cardiac lobes (CL) harvested on post-operative days (Post-OP) 3 and 7. Insets show higher magnification images. At both timepoints Tcf21 lineage-traced (Tcf21^{lin}) cells are found in the lung parenchyma of both sham and pneumonectomized (PNX) mice. Scale bar = 500 μ m.

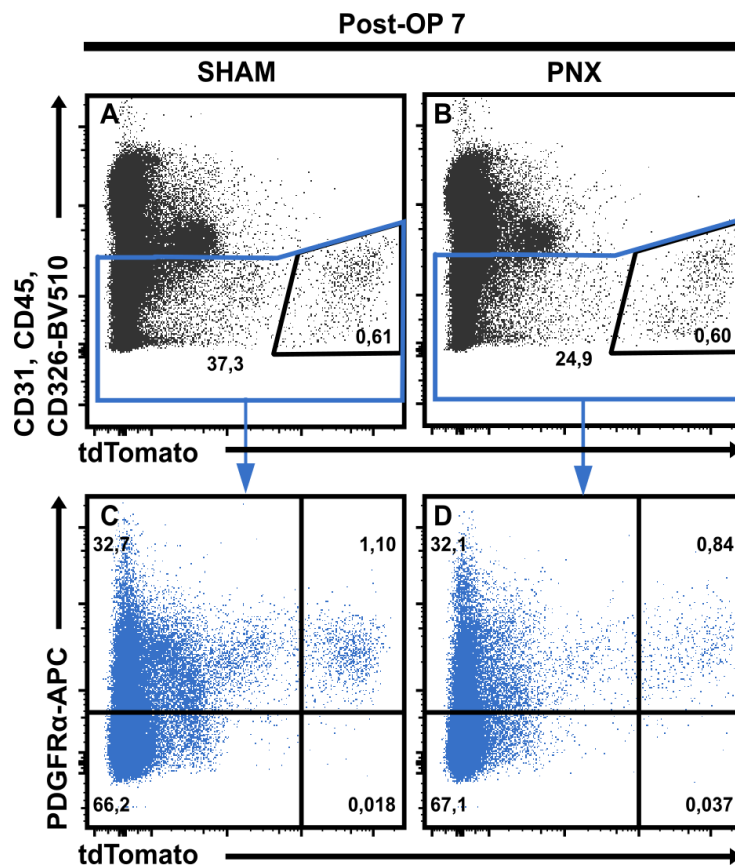


Figure 15. Tcf21^{lin} cells preserve PDGFR-α expression in the mouse after PNX. Representative flow cytometry plots of single cell suspensions from sham-operated (**A** and **C**) and pneumonectomy (PNX)-operated (**B** and **D**). Tcf21^{ICre/+};R26^{tdT/tdT} lineage traced adult mice on post-operative day (Post-OP) 7 were stained with antibodies against CD31, CD45, CD326 and PDGFR-α. Tcf21 lineage-traced (Tcf21^{lin}) cells events were CD31⁻, CD45⁻ and CD326⁻ (**A–B**, gated from single live cells). Tcf21^{lin} events were then gated, demonstrating that most Tcf21^{lin} were additionally PDGFR-α⁺ (**C–D**).

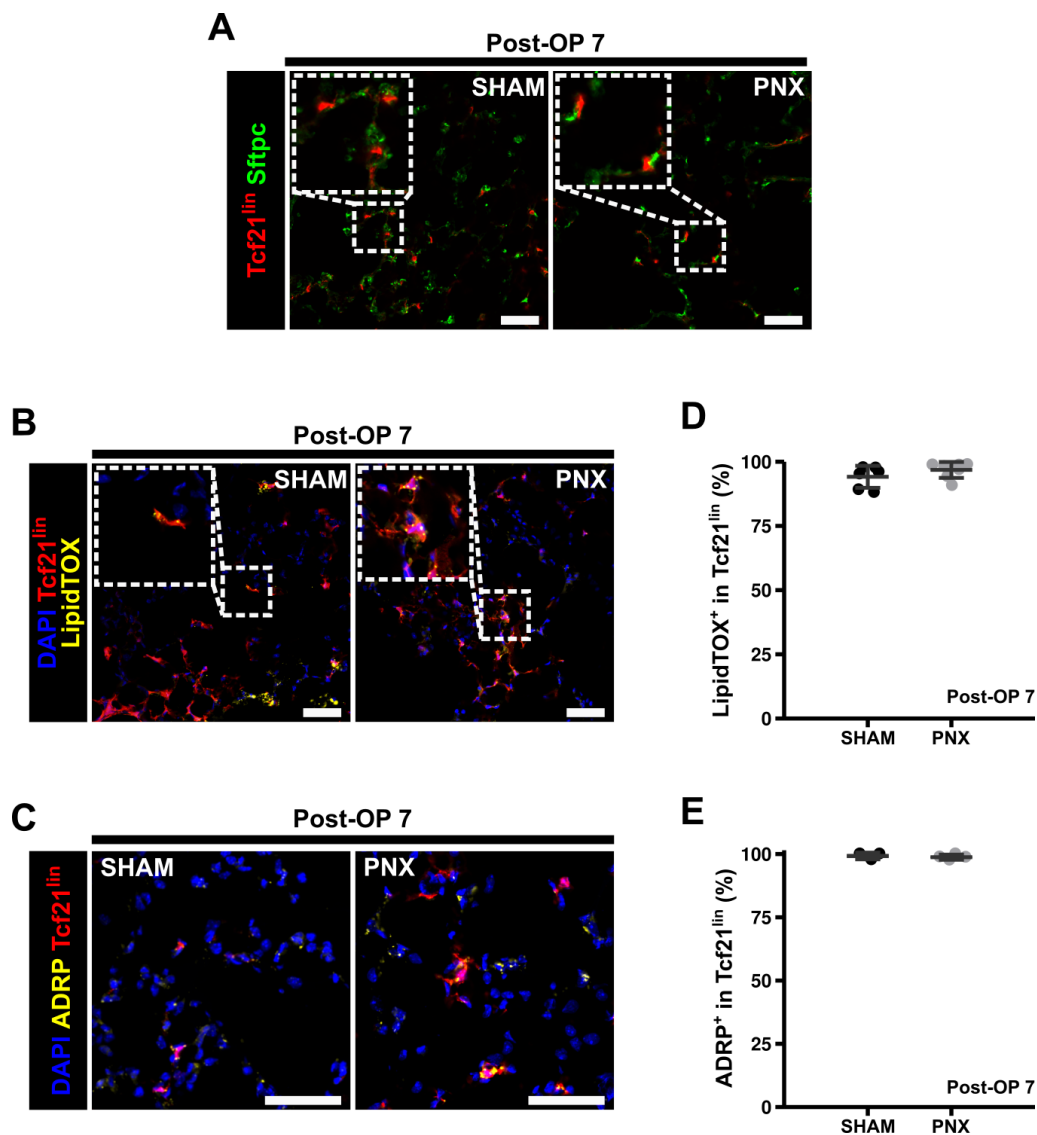


Figure 16. $Tcf21^{lin}$ show lipofibroblast characteristics, which are maintained during neo-alveolarization after pneumonectomy. **A**, **B** and **C**. Confocal imaging of cryosections from post-operated day (Post-OP) 7 $Tcf21^{iCre/+};R26^{tdT/tdT}$ mouse cardiac lobes stained with **A**) anti-Sftpc, **B**) LipidTOX, or **C**) anti-ADRP. $Tcf21$ lineage-traced cells ($Tcf21^{lin}$) in both sham and pneumonectomized (PNX) mice were in close contact with Sftpc⁺ cells. $Tcf21^{lin}$ generally stained with LipidTOX and were ADRP⁺. **D** and **E**. Quantification of the proportion of LipidTOX⁺ (**D**) and ADRP⁺ (**E**) within the $Tcf21^{lin}$ population at Post-OP 7 by flow cytometry. The majority of the $Tcf21^{lin}$ contained lipid droplets and was ADRP⁺. Error bars represent mean \pm SD. n = 3–4 per group for staining of Sftpc and ADRP; n = 6–7 per group for staining of LipidTOX. Groups were compared with an unpaired Student's t-test. Scale bars = 50 μ m.

5.5. Effect of $Tcf21^+$ cell depletion in compensatory lung regrowth

In order to evaluate the contribution of $Tcf21^+$ cells to lung remodeling during the process of compensatory lung regrowth, the next objective was to induce targeted depletion of $Tcf21^+$ cells in $Tcf21^{iCre/+};R26^{tdT/DTA}$ ($Tcf21^{lin}$ -depleted) mice (Fig. 17A) with Tmx injections

during three days before left PNx or sham surgery. Tmx-injected $Tcf21^{+/+};R26^{tdT/DTA}$ mice (non-depleted) were used as controls. Mice were then followed for 7 days after surgery, prior to sacrifice (Fig. 17B) and the lungs were quantitatively analyzed using design-based stereology.

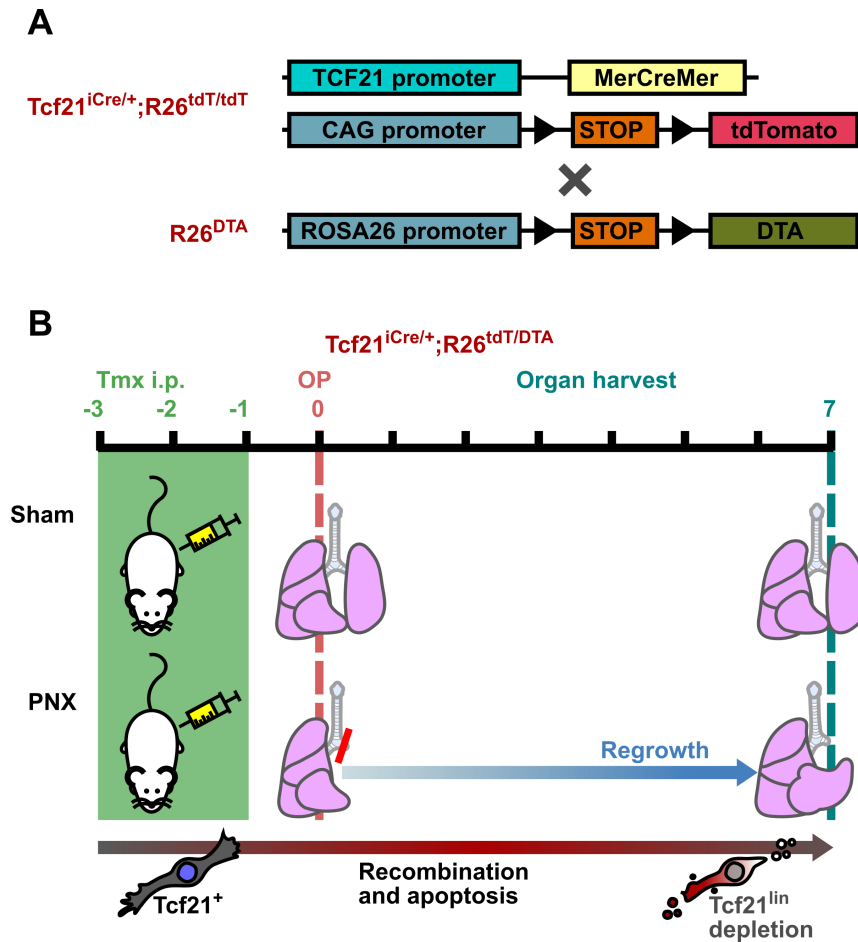


Figure 17. Studying the impact of $Tcf21^{lin}$ cell depletion in compensatory lung regrowth. Scheme illustrating the strategy followed to deplete lineage-traced cells ($Tcf21^{lin}$) before regrowth. **A.** $Tcf21^{iCre/+};R26^{+/+}$ mice were bred with $R26^{DTA/DTA}$ or $R26^{DTA/+}$ mice ($R26^{DTA}$) to generate inducible $Tcf21^{lin}$ depleters ($Tcf21^{iCre/+};R26^{tdT/DTA}$). **B.** Cre-recombination of $Tcf21^{+}$ cells was triggered in adult $Tcf21^{iCre/+};R26^{tdT/DTA}$ mice with Tmx injected during three consecutive days (100 mg/kg/d, i.p.). In this model, recombination triggers the expression of the A subunit of the diptheria toxin (DTA), causing apoptosis of $Tcf21^{lin}$ cells. One day after the last injection, mice underwent sham or left pneumonectomy (PNx) operations (OP). The lungs of operated mice were then harvested on post-operative day 7 for analysis.

During the early observation period following surgery, mice from sham groups initially gained more weight than PNx mice did (Post-OP 2 non-depleted PNx [96.0% ± 4.9%] vs non-depleted SHAM [103.3% ± 2.9%], $P=0.037$; $Tcf21^{lin}$ -depleted PNx [95.4% ± 3.7%] vs

Tcf21^{lin}-depleted SHAM [$105.5\% \pm 6.9\%$], $P < 0.001$) (Fig. 18A). Interestingly, the mean weight of the Tcf21^{lin}-depleted PNx group, which was the lowest of the four groups at Post-OP 2, increased gradually over the following days and became statistically higher than that of non-depleted PNx mice on Post-OP 7 ($113.0\% \pm 8.6\%$ and $105.2\% \pm 3.2\%$ respectively, $P = 0.021$).

During sacrifice at Post-OP 7, ascites was noted in many of the animals examined from both Tcf21^{lin}-depleted groups. As shown in (Fig. 18B), a large amount of ascitic fluid could be collected from some of the depleted animals examined (4 of 5 animals in which this feature was examined) while no fluid could be obtained from any of the control individuals. Another finding observed only in Tcf21^{lin}-depleted animals during the necropsy was the presence of abnormal abdominal adipose tissue. Compared to the fat from non-depleted mice, which had normal characteristics, Tcf21^{lin}-depleted fat tissue seemed loose and was enclosed in an insoluble gel-like capsule. The mesentery of these animals did not seem to be a single continuous structure, but rather, it seemed formed by isolated patches of fat held loosely by abnormally exposed mesenteric vessels (Fig. 18C). Of note, the changes mentioned above were present in Tcf21^{lin}-depleted mice, irrespective of the type of surgical intervention performed.

The lungs of post-operated mice were inflated with fixative under equal pressure conditions and then, the volume of the lungs was estimated (additionally, the volumes of CL, nCL and RL, were also estimated). By Post-OP 7, compensatory regrowth had occurred in PNx mice as evidenced by a higher mass-specific CL and RL volume compared to sham mice in both control and Tcf21^{lin}-depleted mice. Although the RL volume of PNx mice was higher than that of the sham groups, the RL volume of PNx mice was still lower than the total lung volume of the respective sham controls at Post-OP 7, indicating that regrowth remained incomplete at this time point. By Post-OP 7, no

significant difference was found between the mass-specific volume of the analyzed lung fractions of non-depleted PNX and *Tcf21^{lin}*-depleted PNX mice (Fig. 18B).

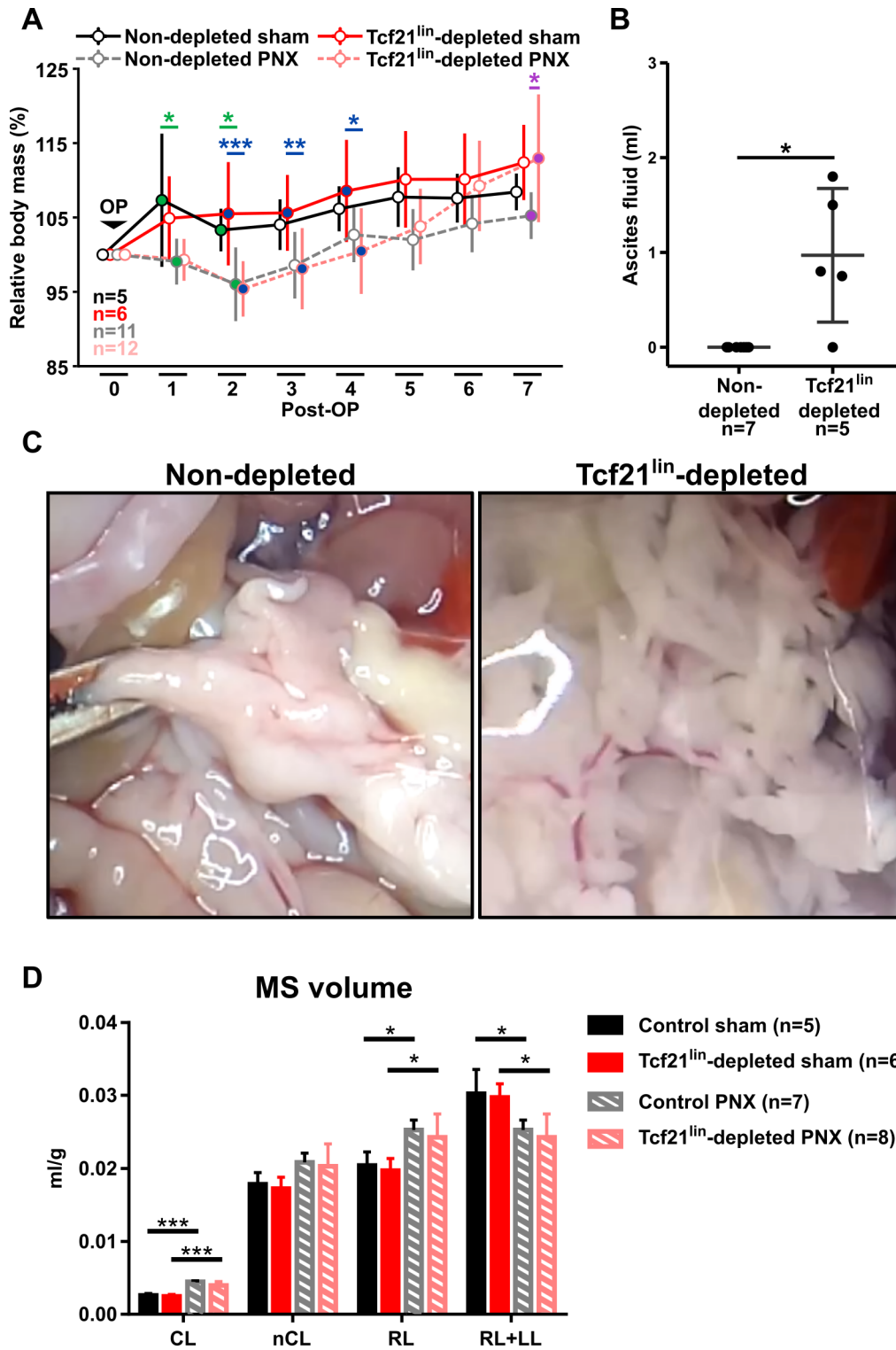


Figure 18. Macroscopic findings during compensatory lung regrowth model after *Tcf21^{lin}* cell depletion. *Tcf21^{iCre/+;R26^{tdT/DTA}}* (*Tcf21^{lin}*-depleted) and *Tcf21^{+/+;R26^{tdT/DTA}}* (non-depleted) mice were allocated to either sham or left pneumonectomy (PNX) groups after induction of Cre-recombination with tamoxifen and followed up to 7 days after

operation (OP). **A.** Body mass change after surgery. Data points indicate group means. Vertical bars indicate ± 1 SD. Statistically significant differences between groups are shown (*) and color-coded within the relevant data points. **B.** Comparison of the volume of collected peritoneal fluid between Tcf21^{lin}-depleted and non-depleted mice. **C.** Appearance of the intra-abdominal fat of Tcf21^{lin}-depleted and non-depleted mice at postoperative day (post-OP) 7. Tcf21^{lin}-depleted fat displayed abnormal morphology. **D.** Comparison of the mass-specific (MS) volume of cardiac lobes (CL), non-cardiac lobes (nCL; the sum of cranial, middle and caudal right lobes), right lungs and total lung volume (RL+LL) between experimental groups. While regrowth was incomplete in both Tcf21^{lin}-depleted and non-depleted lungs at Post- 7, PNx CL and RL showed significant regrowth compared to sham groups. No differential regrowth was observed between PNx Tcf21^{lin}-depleted and non-depleted lungs. Differences between experimental groups were evaluated by one-way ANOVA with Tukey's post hoc test for each time point in A and for each lobe subset in D. Groups in B were compared with an unpaired Student's t-test. (* $P \leq 0.05$, ** $P \leq 0.01$, *** $P \leq 0.001$).

As illustrated in Fig. 19 and in table 7, several structural parameters estimated using design-based stereology indicated the occurrence of neo-alveolarization in both PNx groups (non-depleted and Tcf21^{lin}-depleted). The CL had higher respiratory surface area, total septal volume and number of alveoli compared to the corresponding SHAM controls when normalized to body mass. The mass-normalized estimates of respiratory surface area, number of alveoli and septal volume, which are better indicators of generation of new gas exchange areas, were similar between non-depleted and Tcf21^{lin}-depleted PNx mice, suggesting that neo-alveolarization occurred in both PNx groups without pronounced differences.

In a previous experiment, the extent of Tcf21⁺ cell depletion in animals which had not undergone surgical procedures to validate the depletion model was estimated. There, Tcf21^{iCre/+R26^{tdT/tdT}} and Tcf21^{iCre/+R26^{tdT/DTA}} animals were sacrificed 6 days after the initial injection of Tmx of a total of 3 injections (100 mg/kg/d). On CL cryosections, a mean reduction of ~50% was observed in the abundance of Tcf21^{lin} in Tcf21^{iCre/+R26^{tdT/DTA}} lungs with respect to the non-depleted Tcf21^{iCre/+R26^{tdT/tdT}} controls (3.07% \pm 0.57% in Tcf21^{iCre/+R26^{tdT/tdT}} vs 1.53% \pm 0.35% in Tcf21^{iCre/+R26^{tdT/DTA}}, $P=0.004$) (Fig. 20).

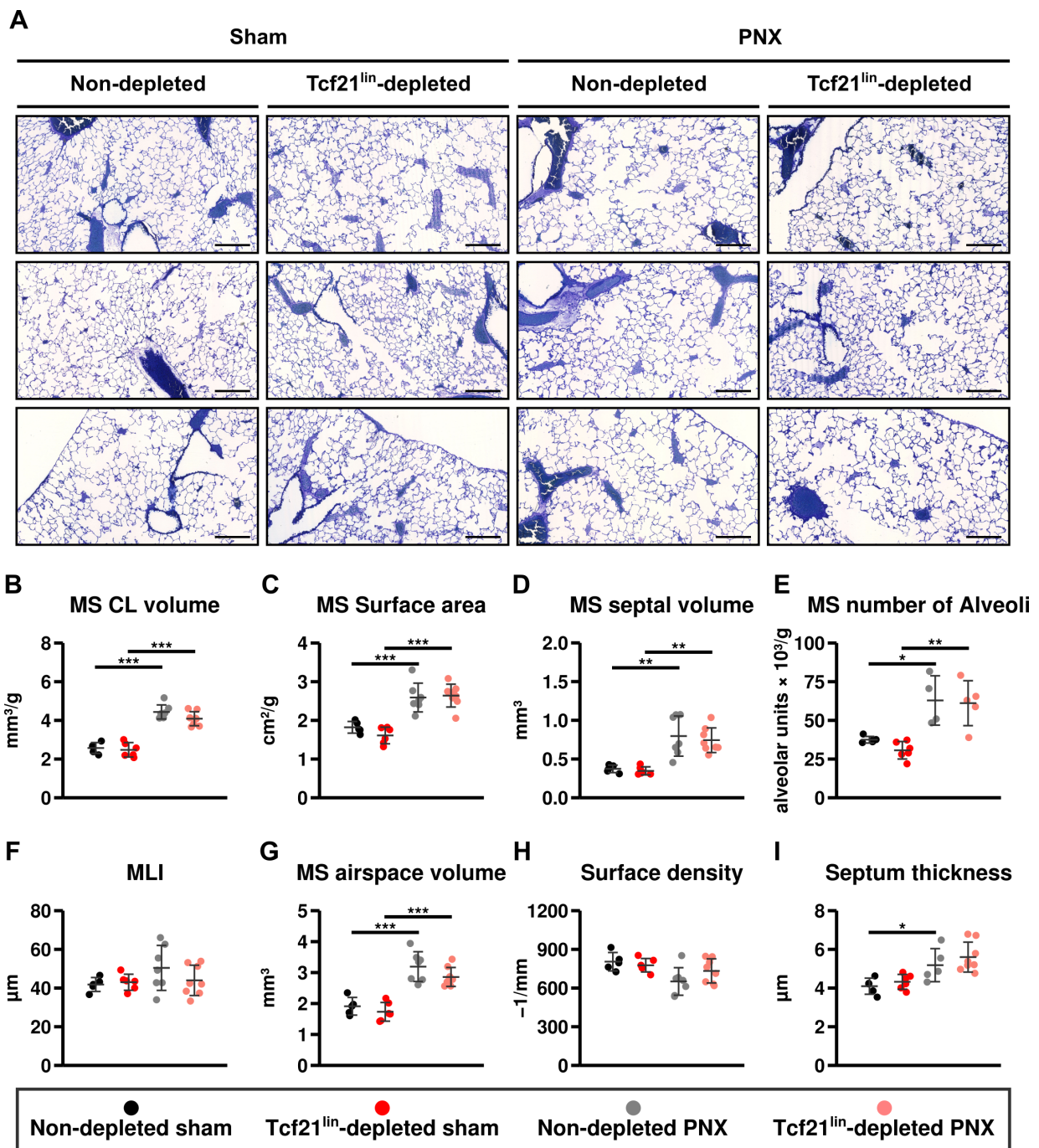


Figure 19. Stereological analysis of the effect of Tcf21^{lin} depletion on compensatory lung regrowth. A. Representative micrographies of sham and pneumonectomized (PNX) lungs at post-operative day (Post-OP) 7, without depletion or with partial depletion of Tcf21^{lin} (non-depleted and Tcf21^{lin}-depleted respectively). **B-I.** Comparison of several stereological parameters estimated in cardiac lobes: **B.** Mass-specific (MS) cardiac lobe (CL) volume. **C.** MS alveolar surface area. **D.** MS alveolar septal volume. **E.** MS number of alveoli. **F.** Mean linear intercept (MLI) **G.** MS volume of airspaces. **H.** Respiratory surface density. **I.** Alveolar septum thickness. N = 5–8 mice. Differences between experimental groups were evaluated by one-way ANOVA with Tukey's post hoc test (* $P \leq 0.05$, ** $P \leq 0.01$, *** $P \leq 0.001$). Scale = 250 μm.

Table 7. Stereological analysis of the structural impact of partial Tcf21^{lin} cell depletion on compensatory lung regrowth. Body mass, lobar volume and stereological estimates of cardiac lobes on post-operative day (Post-OP) 7 are shown for Tcf21^{lin}-depleted (Tcf21^{iCre/+}R26^{tdT/DTA}) and non-depleted (Tcf21^{+/+}R26^{tdT/DTA}) controls of both sham or pneumonectomized (PNX) groups. Summaries of each group are presented as mean (SD) and *P*-values are displayed in separate columns. No significant differences were found between sham groups or between PNX groups and due to space constrains resulting *P*-values from comparisons between sham groups were omitted. Superscripted letters indicate statistically significant differences (*P*≤0.05) versus a) sham control, and b) sham depleted.

Parameter [units]	Sham		PNX		P-value		
	Control	Tcf21 ^{lin} -depleted	Control	Tcf21 ^{lin} -depleted	Sham vs PNX		PNX
					Controls	Tcf21 ^{lin} -depleted	Tcf21 ^{lin} -depleted vs controls
Body mass [g]	28.1 (3.5)	26.3 (2.3)	27.9 (1.4)	26.7 (3.2)	0.999	0.997	0.576
CE CV CE ² /CV ²	0.06 0.12 0.2	0.04 0.09 0.17	0.02 0.05 0.14	0.04 0.12 0.13			
MS V(CL) [ml/g]	2.6 (0.3)	2.5 (0.4)	4.4 (0.4) ^a	4.1 (0.4) ^b	<0.001	<0.001	0.129
CE CV CE ² /CV ²	0.05 0.11 0.2	0.06 0.15 0.17	0.03 0.08 0.14	0.03 0.09 0.13			
V(CL) [mm³]	72 (9.1)	65 (8.9)	123.6 (9.4) ^a	108.8 (15.8) ^b	<0.001	<0.001	0.058
CE CV CE ² /CV ²	0.06 0.13 0.2	0.06 0.14 0.17	0.03 0.08 0.14	0.05 0.14 0.13			
V_v(par/CL) [%]	88.5 (3.5)	83.9 (3.1)	90.2 (3.1)	88.6 (2.5)	0.791	0.101	0.505
CE CV CE ² /CV ²	0.02 0.04 0.2	0.02 0.04 0.17	0.01 0.03 0.14	0.01 0.03 0.13			
MS S(alv,CL) [cm²/g]	1.8 (0.2)	1.6 (0.2)	2.6 (0.4) ^a	2.6 (0.3) ^b	0.001	<0.001	0.999
CE CV CE ² /CV ²	0.04 0.08 0.2	0.05 0.13 0.17	0.05 0.14 0.14	0.04 0.11 0.13			
S(alv,CL) [cm²]	51 (6.1)	42.3 (6.4)	72.4 (11.9) ^a	70.4 (11.9) ^b	0.011	0.001	0.861
CE CV CE ² /CV ²	0.05 0.12 0.2	0.06 0.15 0.17	0.06 0.16 0.14	0.06 0.17 0.13			
S_v(alv,CL) [mm⁻¹]*	804.3 (71.5)	776.9 (52.2)	651.1 (106.9)	732.9 (93.7)	0.070	0.994	0.147
CE CV CE ² /CV ²	0.04 0.09 0.2	0.03 0.07 0.17	0.06 0.16 0.14	0.05 0.13 0.13			
MS N(alv,CL) [1×10³/g]	37.5 (2.1)	30.7 (5.7)	62.9 (15.9) ^a	61.1 (14.5) ^b	0.017	0.003	0.893
CE CV CE ² /CV ²	0.03 0.06 0.2	0.08 0.18 0.17	0.13 0.25 0.25	0.11 0.24 0.2			
N(alv,CL) [1×10⁶]	1.1 (0.1)	0.8 (0.1)	1.7 (0.4)	1.7 (0.5) ^b	0.059	0.012	0.859
CE CV CE ² /CV ²	0.06 0.13 0.2	0.07 0.17 0.17	0.12 0.25 0.25	0.13 0.28 0.2			
N_v(alv,CL) [1×10³/mm³]	16.6 (1.5)	14.9 (2.3)	15.3 (4.4)	17 (4.7)	0.940	0.649	0.839
CE CV CE ² /CV ²	0.04 0.09 0.2	0.06 0.16 0.17	0.14 0.29 0.25	0.12 0.28 0.2			
MS V(sep,CL) [mm³/g]	0.37 (0.05)	0.35 (0.05)	0.8 (0.26) ^a	0.74 (0.16) ^b	0.002	0.002	0.775
CE CV CE ² /CV ²	0.06 0.13 0.2	0.06 0.15 0.17	0.12 0.33 0.14	0.08 0.21 0.13			
MLI [μm]	41.8 (3.6)	43 (4.1)	50.4 (11.6)	44 (7.8)	0.298	1.000	0.250
CE CV CE ² /CV ²	0.04 0.09 0.2	0.04 0.1 0.17	0.09 0.23 0.14	0.06 0.18 0.13			
τ(sep) [μm]	4.1 (0.4)	4.3 (0.4)	6.1 (1.7) ^a	5.6 (0.8)	0.017	0.218	0.589
CE CV CE ² /CV ²	0.05 0.1 0.2	0.04 0.09 0.17	0.11 0.28 0.14	0.05 0.14 0.13			
V(sep,CL) [mm³]	10.4 (1.6)	9.2 (1.7)	22.3 (7.8) ^a	19.8 (4.6) ^b	0.004	0.010	0.518
CE CV CE ² /CV ²	0.07 0.15 0.2	0.08 0.19 0.17	0.13 0.35 0.14	0.08 0.23 0.13			
V_v(sep/CL) [%]	16.4 (0.9)	16.9 (2.5)	20.2 (7.4)	20.6 (4.4)	0.510	0.434	0.998
CE CV CE ² /CV ²	0.02 0.05 0.2	0.06 0.15 0.17	0.14 0.36 0.14	0.08 0.21 0.13			

MS, mass-specific; **V**, volume; **CL**, cardiac lobe; **par**, parenchyma; **S**, Surface (of alveolar epithelium); **N**, number; **MLI**, mean linear intercept; **τ**, thickness; **sep**, septum; **air**, airspaces; **CE**, coefficient of error; **CV**, coefficient of variation.

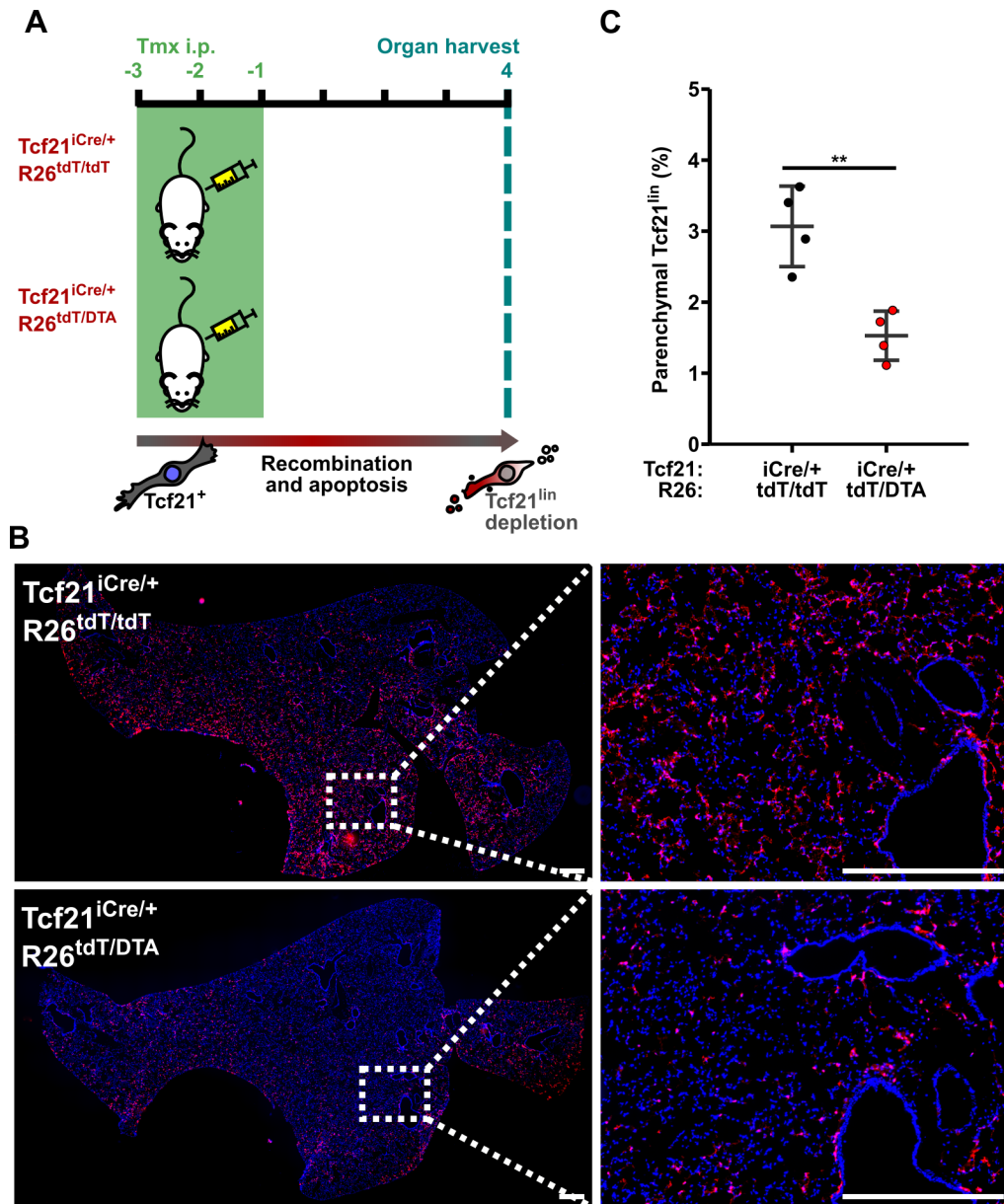


Figure 20. Tamoxifen injection of adult $Tcf21^{iCre/+};R26^{tdT/DTA}$ mice results in partial depletion of $Tcf21^{lin}$ cells. To validate the extent of $Tcf21^{lin}$ depletion induced by Cre-recombination, the proportion of $Tcf21^{lin}$ in the lung parenchyma was estimated in relation to all nucleated cells in cryosections. **A.** $Tcf21^{iCre/+};R26^{tdT/DTA}$ and $Tcf21^{iCre/+};R26^{tdT/+}$ mice were injected with tamoxifen (Tmx) during three consecutive days (100mg/Kg/d, intraperitoneal [i.p.]). 6 days after the initial injection, mice were sacrificed and the lungs were cryopreserved for sectioning. **B.** Whole section scans (left) and higher magnification pictures (right) of $Tcf21^{iCre/+};R26^{tdT/tdT}$ and $Tcf21^{iCre/+};R26^{tdT/DTA}$ mice after induction of depletion of $Tcf21$ lineage-traced cells ($Tcf21^{lin}$). $Tcf21^{lin}$ seem less abundant in DTA mice. **C.** Comparison of the abundance of $Tcf21^{lin}$ in mice with depletion or without depletion of $Tcf21^{lin}$. Tamoxifen injections induced ~50% reduction of $Tcf21^{lin}$ in $Tcf21^{iCre/+};R26^{tdT/DTA}$ mice. $n = 4$. Experimental groups were compared with an unpaired Student's t-test. (** $P \leq 0.01$). Scale bar = 500 μ m.

5.6. Contribution of the Tcf21 lineage to alveolosphere formation and growth

Lung organoids have been used by multiple other authors to study the involvement of certain cell types, often epithelial cells in lung development, repair or regeneration. These models commonly include non-epithelial cells that support epithelial organoid growth and thus could be used to investigate differentiation processes and mechanics of cell-to-cell interactions in an environment with limited cell heterogeneity compared to the native tissue (Nadkarni, Abed, and Draper 2016; Barkauskas et al. 2017).

Since a population of mesenchymal cells containing lipofibroblasts has been shown to support AEC2 (Barkauskas et al. 2013), the hypothesis of whether Tcf21^{lin} cells may support formation of alveolar-like structures *in vitro* was tested. First, a model of alveolospheres was used, in which an epithelial cell population enriched for AEC2 (CD326^{int} CD24^{low}), was co-cultured with resident mesenchymal cells (rMC [CD31⁻CD45⁻CD326⁻Sca1⁺]) (See general workflow of the experiment in Fig. 21). Thus, the aforementioned populations were sorted from Tcf21^{Cre+/-}R26R^{tdT/tdT} lung cell suspensions to generate control alveolosphere cultures (AEC2 + rMC). The sorted rMC population contained a fraction of the Tcf21^{lin} (Fig. 21B). To test whether Tcf21^{lin} cells play a role in formation of spheres, co-culture of AEC2 was also performed with rMC that were devoid of Tcf21^{lin} cells (AEC2 + Tcf21⁻ rMC) identified as CD31⁻CD45⁻CD326⁻Sca1⁺tdTomato⁻ or, alternatively, with rMC belonging to the Tcf21 lineage (AEC2 + Tcf21^{lin} rMC) with the phenotype CD31⁻CD45⁻CD326⁻Sca1⁺tdTomato⁺. As expected, by 14 days of culture (d14), control AEC2 + rMC cultures had developed spheres (Fig. 22). Comparatively, AEC2 + Tcf21⁻ rMC cultures had generated fewer organoids than those in control AEC2 + rMC cultures (43.04% ± 4.67% reduction, $P=0.006$). In contrast, culture of AEC2 + Tcf21^{lin} rMC

did not develop spheres. These results suggest that $Tcf21^{lin}$ cells are important, albeit, not sufficient for generation of alveolospheres.

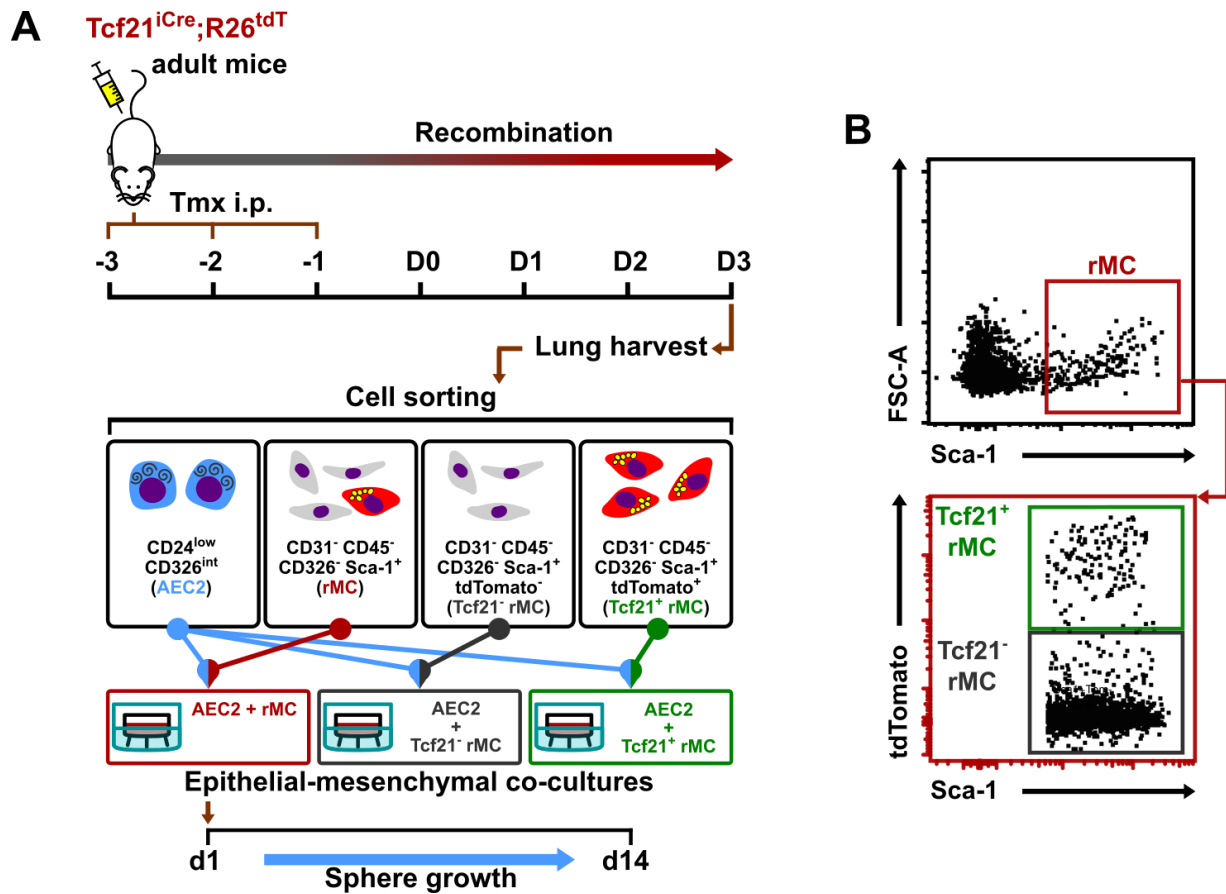


Figure 21. Experimental workflow for evaluation of the effect of TCF21^{lin} cells on a model of alveolosphere formation. **A.** General experimental scheme. $Tcf21^{iCre/+};R26^{tdT/tdT}$ mice were injected with tamoxifen (Tmx) once a day for three consecutive days. Cre recombination, and thus, expression of tdTomato by $Tcf21^{lin}$ was allowed to occur during the following days (D0-3). Six days after the first Tmx injection the animals were sacrificed, single cell suspensions were prepared from the harvested lungs. Then, four cell populations were isolated via cell sorting, including one epithelial population enriched for alveolar type 2 cells (AEC2, with the phenotype $CD24^{low}CD326^{int}$) and three resident mesenchymal cell populations: 1) $CD31^{-}CD45^{-}CD326^{+}Sca-1^{+}$ (rMC); 2) $CD31^{-}CD45^{-}CD326^{+}Sca-1^{+}tdTomato^{-}$ ($Tcf21^{-}$ rMC); and 3) $CD31^{-}CD45^{-}CD326^{+}Sca-1^{+}tdTomato^{+}$ ($Tcf21^{+}$ rMC). To evaluate the capacity of the different sorted mesenchymal populations to support organoid formation, rMC, $Tcf21^{-}$ rMC and $Tcf21^{+}$ rMC were each individually co-cultured in matrigel with AEC2 and alveolosphere growth was followed for 14 days. **B.** Flow cytometry plots demonstrating the gating strategy for the different mesenchymal populations that were co-cultured with AEC2. The top panel is gated from $CD31^{-}CD45^{-}CD326^{+}$ events. i.p. intraperitoneal.

In the aforementioned experiment, $Tcf21^{lin}$ did not seem to be particularly in close proximity with the forming alveolospheres (Fig. 22A), suggesting that cell to cell contact may not be necessary for alveolosphere growth. Therefore, it was explored whether $Tcf21^{lin}$ may

support alveolosphere formation even in absence of direct contact with epithelial cells. Thus, AEC2, Tcf21^{-rMC} and CD31⁻CD45⁻CD326⁻Sca1⁺tdTomato⁻ (Tcf21^{lin}) were FACS-sorted from Tcf21^{iCre/+;R26^{tdT/tdT}} lung cell suspensions from adult mice as explained above. Co-cultures of AEC2 + Tcf21^{-rMC} were generated in inserts, while Tcf21^{lin} alone were seeded in wells. After 24 h, inserts with AEC2 + Tcf21^{-rMC} were transferred to new wells with either medium only, or to wells containing Tcf21^{lin} (Tcf21^{lin}-supplemented) and followed for a further 13 days (Fig. 23A). By day 14, cultures containing Tcf21^{lin} had developed more and larger alveolospheres than the control group without Tcf21^{lin} (Fig. 23B-F). Given that AEC2 and Tcf21^{lin} were physically separated, the higher alveolosphere growth displayed in the tricultures suggests that Tcf21^{lin} may secrete soluble factors that promote alveolosphere formation and growth.

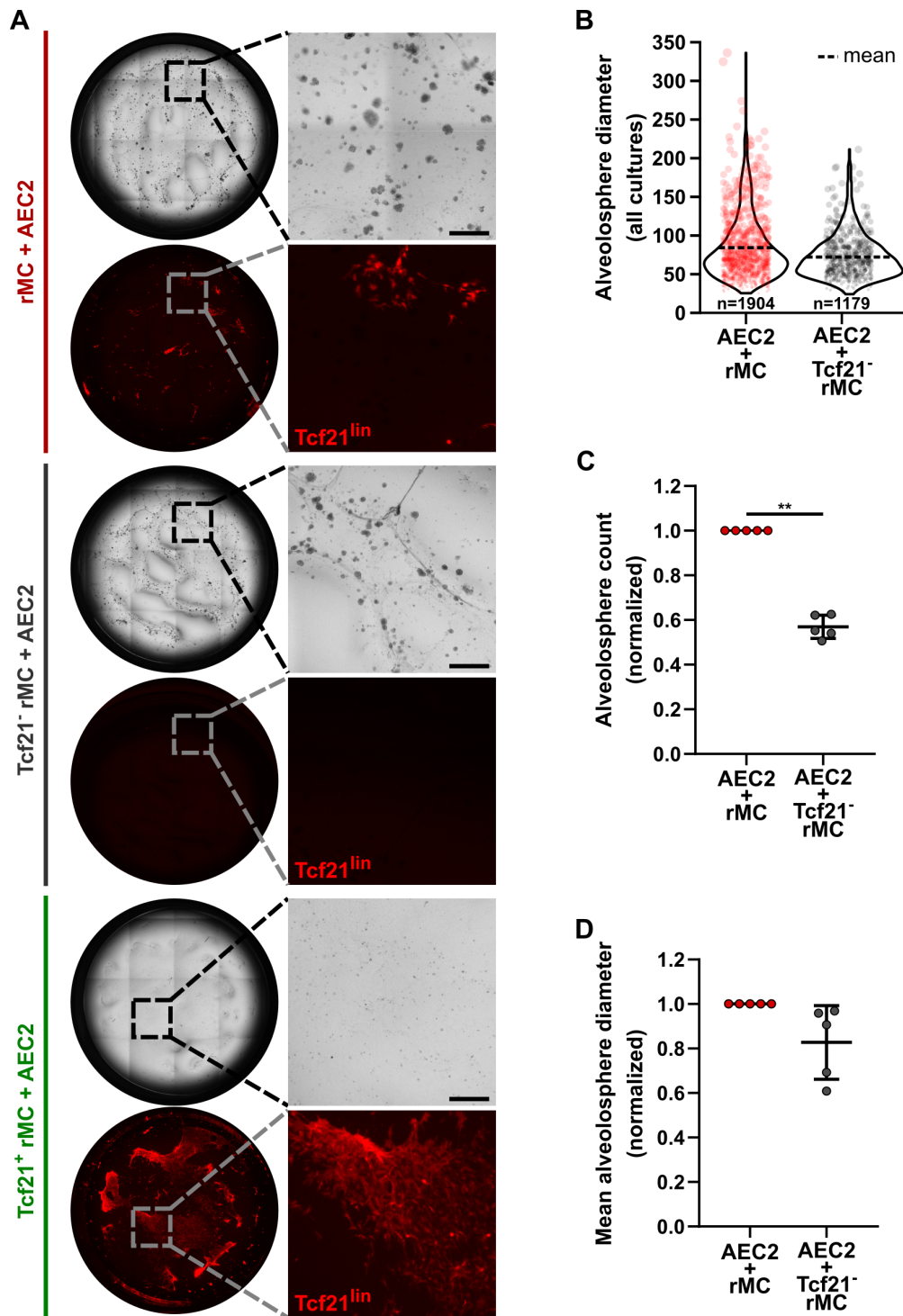


Figure 22. Tcf21^{lin} cells are important for alveolosphere formation. Three populations of resident mesenchymal cells (rMC, Tcf21⁻ rMC or Tcf21⁺ rMC) were independently co-cultured ($\sim 2.5 \times 10^4$ cells each) with alveolar epithelial type 2 cells (AEC2) ($\sim 2 \times 10^4$ cells) to evaluate the ability of Tcf21^{lin} cells to support alveolosphere formation. Analysis was performed at day 14 of culture. **A.** Whole well pictures (left circles) and higher-magnification pictures (right) of co-cultures. Brightfield images (top images within each group) reveal that both AEC2 + rMC and AEC2 + Tcf21⁻ rMC co-cultures generated alveolospheres, but AEC2 + Tcf21⁺ rMC co-cultures failed to generate alveolospheres. Fluorescent imaging of tdTomato⁺ cells from the same wells (bottom images within each group) revealed that Tcf21^{lin} were present in AEC2 + rMC co-cultures, while Tcf21^{lin} were abundant in AEC2 + Tcf21⁺ rMC cultures (where all seeded rMC's expressed tdTomato) and virtually absent in AEC2 + Tcf21⁻ rMC cultures. **B.** Violin plots displaying the density of alveolosphere diameters in all

cultures. Jittered data-points represent individual spheres, which diameter is depicted to scale. Group mean diameters are indicated by dashed lines. No statistical comparisons are shown. **C.** Relative comparison of the number of spheres in 14-day old co-cultures. Normalization was performed between matched cultures of cells derived from the same subjects. AEC2 + Tcf21⁺rMC co-cultures consistently yielded fewer spheres compared to matched AEC2 + rMC co-cultures. **D.** Comparison of the mean alveosphere size between paired AEC2 + Tcf21⁺rMC and AEC2 + rMC cultures. n = 5. Experimental groups were compared in C and D with an unpaired Student's t-test. (**P≤0.01). Scale bars = 200 μm.

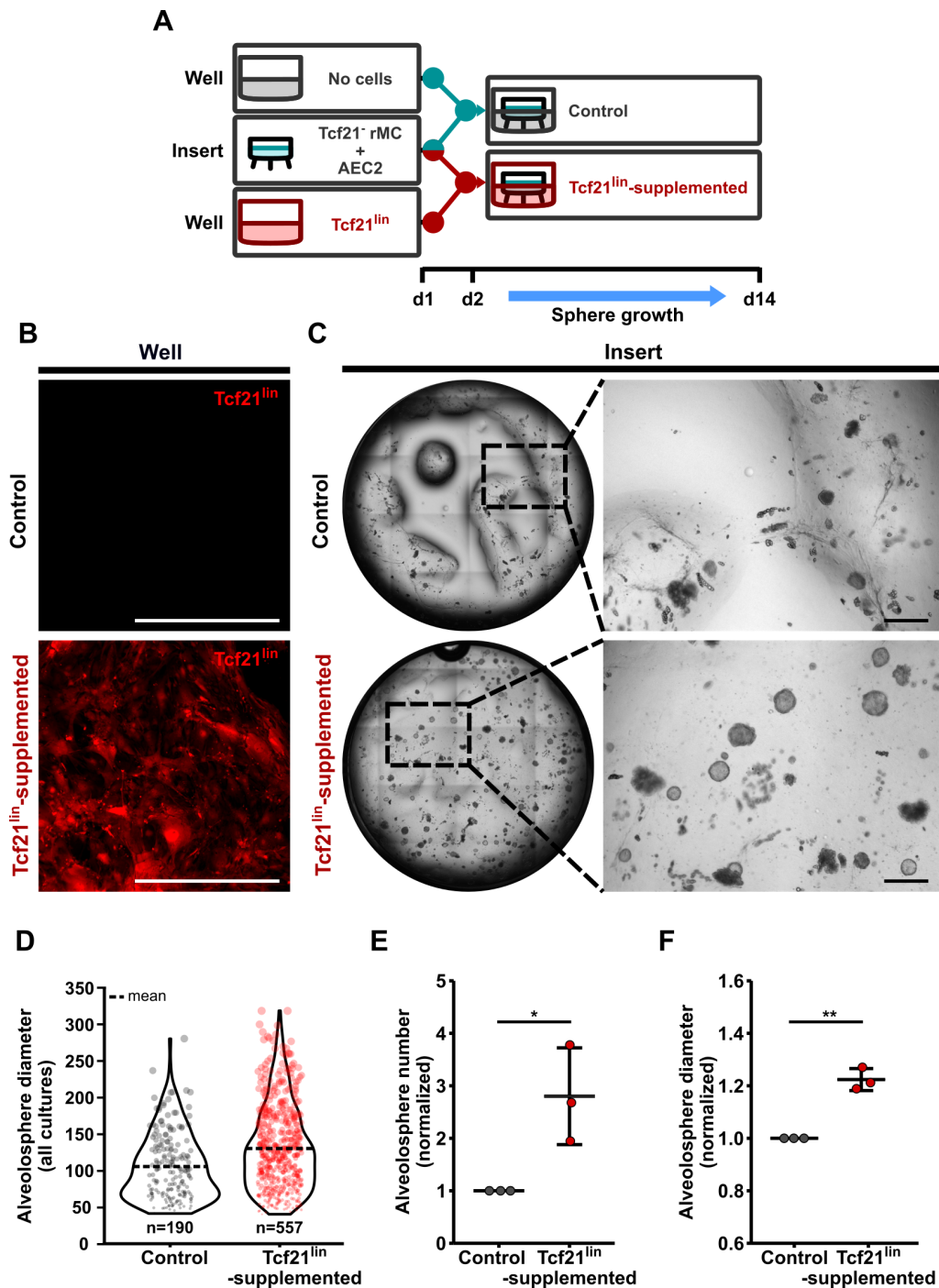


Figure 23. Tcf21^{lin} cells promote alveosphere formation in absence of direct contact with alveolar epithelial type 2 cells. **A.** Experimental design used to test whether Tcf21^{lin} can influence alveosphere formation in absence of cell to cell contacts, previously sorted Tcf21⁺ resident mesenchymal cells (rMC) (~2.5×10⁴) + alveolar epithelial type 2

cells (AEC2) ($\sim 1 \times 10^4$) were seeded in inserts and cultured alone (Control) or transferred to wells containing Tcf21^{lin} ($\sim 4 \times 10^3$) 24 h after seeding. Cultures were observed for sphere growth for 14 days (d1–14). **B.** Fluorescence microscopy images of the bottom of wells of control co-cultures or cultures with Tcf21^{lin} on d14. Lack of tdTomato signal verified the absence of Tcf21^{lin} cells in the control empty wells. **C.** Whole well representative pictures (left) and higher-magnification images (right) of inserts from co-cultures on d14. More and bigger alveolospheres are apparent in Tcf21^{lin}-supplemented cultures. **D.** Descriptive violin plots displaying the density of sphere diameters pooled from all cultures. Jittered data-points represent individual spheres, which diameter is depicted to scale. Dashed lines indicate group mean diameters. **E and F.** Comparison of alveolosphere number (E) and diameter (F) between paired control and Tcf21^{lin}-supplemented cultures. Both parameters were statistically higher in Tcf21^{lin}-containing cultures than in control cultures. $n = 3$. Groups were compared in E and F with an unpaired Student's t-test. ($*P \leq 0.05$, $**P \leq 0.01$). Scale bars = 500 μm .

6. Discussion

The present work aimed to characterize the phenotype and role of Tcf21-expressing cells and the Tcf21 lineage during homeostasis and alveolarization processes of the murine lung. To achieve this aim, lineage tracing of Tcf21 was performed *in vivo* during late lung development, homeostasis and neo-alveolarization; and the impact of Tcf21⁺ cell deficiency was investigated both *in vitro* (in an organoid model) and *in vivo* (in a compensatory regrowth model). During secondary septation, Tcf21^{lin} contained abundant lipid droplets and showed active proliferation. This findings coincide with a period of high lipid droplet accumulation in lipid interstitial cells, septum and lung; as well as high abundance of lipofibroblasts in the rodent lung (Kaplan, 1985; Maksvytis, 1981; Tahedl, 2014). In the adult lung, Tcf21^{lin} continued to harbor neutral lipid deposits, had a lipofibroblastic phenotype and displayed a branched morphology. Following partial depletion of Tcf21^{lin} in adult mice no significant effect was observed in the structure of the lung during post-pneumonectomy compensatory regrowth; however, alveolosphere formation by AEC2 in a co-culture system was impaired in absence of Tcf21^{lin}.

Tcf21 has been described to be expressed in a variety of organs during different stages of development (kidney, heart, facial muscle, adrenal gland, spleen, lung, gonads) (Quaggin et al. 1999; Acharya et al. 2011, 2012; Braitsch et al. 2012). In mature mice Tcf21 expression can be found in several organs including kidney, lung, heart and adipose tissue (Kanisicak et al. 2016; Maezawa et al. 2014; de Jong et al. 2015; Park et al. 2019). In some organs, expression of Tcf21 is required for proper development or even organogenesis. This is the case of heart, kidney, spleen, and lung (Quaggin et al. 1999; Braitsch et al. 2012; Lu et al. 2000). Tcf21 expression has previously been detected in mesenchymal cells of the developing lung (Quaggin et al. 1999; McGowan and McCoy

2014; Swonger et al. 2016). In this work, it was demonstrated that Tcf21⁺ cells in the lung parenchyma of mice are exclusively mesenchymal cells that primarily display a lipofibroblastic phenotype. This was indicated by the presence of neutral lipid droplets, ADRP staining and the proximity of these cells to AEC2. Furthermore, during secondary alveolarization and during neo-alveolarization, the Tcf21 lineage also displayed a lipofibroblastic phenotype.

The close relation between lipofibroblasts and AEC2 has been recognized by several authors (O'Hare and Sheridan 1970; McGowan and Torday 1997; Brody 1985). Here, the use of a fluorescent conditional reporter with nuclear and cytoplasmic expression facilitated the exploration of both the morphology of a lipofibroblast subset and the spatial relationship of this subset with other cell-types. In this regard, evidence presented in this work shows that Tcf21⁺ lipofibroblast-AEC2 close spatial relationship is not limited to contact between cell bodies. Cytoplasmic processes of Tcf21⁺ cells also make contact with non-immediately adjacent AEC2, thus, increasing the number of AEC2 that a single Tcf21⁺ cell can contact with. Nonetheless, the biological relevance of the proximity between Tcf21⁺ cell cytoplasmic processes and AEC2 is yet to be determined since it is unknown whether these areas may serve as sites for interactions similar to those found between adjacent cell bodies or may, alternatively, be home to interactions of different nature.

A fraction of the Tcf21^{lin} cytoplasmic processes were found to follow the border of capillary loop edges in a fashion not previously described before to the best knowledge of the author. One might speculate that the intricate relationship between Tcf21⁺ cells and alveolar capillaries might be the result of developmental ties between these cells, or could facilitate endothelium-fibroblast interactions. Evidence of the importance of Tcf21 for correct development of capillaries in the lung comes from previous works in which Tcf21^{-/-} mice at birth showed abnormal capillary location, where no capillaries are found in close

proximity to the alveolar epithelium; additionally in the kidney, Tcf21 null mice and podocyte-specific Tcf21 null mice show arrested glomerular development with aberrant capillary loop formation (Quaggin et al. 1999; Maezawa et al. 2014). However, the relevance of the close relationship between Tcf21^{lin} and endothelial cells in the lung remains to be investigated.

The presence of cytoplasmic lipid droplets is the defining feature of lipid-interstitial cells or lipofibroblasts. *In vitro*, it was demonstrated that triglycerides, the main component of lipofibroblast lipid droplets, can be transferred from lipofibroblasts to AEC2 (Maksvytis, Vaccaro, and Brody 1981; J. Torday, Hua, and Slavin 1995); *in vivo*, the peak of triglyceride content in the mouse lung occurs during postnatal development and coincides with an increase of surfactant production which has led authors to believe that lipofibroblasts support AEC2 providing substrates for the generation of surfactant (Sorokin, Padykula, and Herman 1959; McGowan and Torday 1997). In this study, it was found that Tcf21^{lin} labeled before and during the peak of secondary septation display abundant lipid droplet deposits; at P7 and P14, these cells demonstrated to be in contact with AEC2, possibly facilitating lipid transfer to AEC2. Of note, the rate of proliferation of Tcf21^{lin} was also coincidental with secondary septation since proliferating Tcf21^{lin} were found at P7, but were nearly absent at P14.

In this work the expression of Tcf21 and the persistence of a lipidic phenotype was clearly demonstrated. Tcf21⁺ cells during late lung development, that were traced and analyzed at various intervals, consistently had characteristics of lipofibroblasts. In adult animals, Tcf21⁺ cells were also observed to have lipid droplets, albeit these droplets were visibly scarcer than those of developing lungs, similar to what has been described for lipofibroblasts previously (Kaplan, Grant, and Brody 1985). Furthermore, Tcf21^{lin} cells maintained their lipidic phenotype after PNX.

In the organoid studies presented here, the presence of Tcf21^{lin} supported the growth of alveolospheres in combination with another (Sca1⁺) mesenchymal population. This result is consistent with findings from Barkauskas et al. (Barkauskas et al. 2013). In that work, alveolosphere growth from AEC2 was facilitated by co-culture with primary PDGFR- α ⁺ lung stromal cells, a population that included lipofibroblasts. Since CD31⁻CD45⁻Sca1⁺ cells from mouse lungs have shown to co-express PDGFR- α (McQualter et al. 2013), it is likely that the Sca-1⁺ population that is required to allow Tcf21^{lin} support over alveolosphere formation expresses PDGFR- α and might be contained within the population employed by Barkauskas. However, characterization of this cell population was beyond the scope of this work.

Although interactions between lipofibroblasts and AEC2 are likely to be facilitated by the proximity of these two cell-types *in vivo*, the organoid model generated during this study did not allow to investigate aspects related to intercellular contacts. However, alveolosphere growth support by Tcf21^{lin} was present in absence of contact between Tcf21^{lin} and AEC2, suggesting that at least some of the AEC2-supporting actions by lipofibroblasts are not cell-contact-dependent and must be mediated by soluble factors.

Evidence exists of the capacity of lung fibroblasts to differentiate to and from myofibroblastic phenotypes. In the normal lung, for example, myofibroblasts arise during late lung development and participate in secondary septum formation; at this stage myofibroblasts are derived from and partially overlap with PDGFR- α ⁺ cells (Boström et al. 1996; McGowan et al. 2008; Branchfield et al. 2016; Ntokou et al. 2015). Furthermore, during compensatory regrowth after pneumonectomy, a transient increase of PDGFR- α ^{dim} α -SMA⁺ myofibroblasts was synchronous with neo-alveolarization (Chen et al. 2012). Additionally, in a recent work, el Agha et al. demonstrated that lipofibroblasts (identified via ADRP lineage labeling) are an important source of myofibroblasts in a model of

bleomycin-induced fibrosis. There, ADRP^{lin} labeled 4 weeks before bleomycin exposure accounted for ~20% of the myofibroblasts at the peak of fibrosis. Conversely, upon lineage labeling of α -SMA during fibrosis, ~30% of the α -SMA-lineage was found to acquire a lipofibroblastic phenotype (based on the expression of ADRP) after fibrosis resolution (El Agha, Moiseenko, et al. 2017). All these findings illustrate the plasticity of fibroblasts and suggest that fibroblasts can switch phenotype in response to different stimuli. Strikingly, this study demonstrated that only a negligible fraction of the Tcf21⁺ cells transitioned or gave rise to myofibroblasts and that Tcf21^{lin} contributed very little to the myofibroblast pool during secondary alveolarization. While Tcf21⁺ lipofibroblasts did not show a myofibroblastic phenotype under the conditions tested in this work, whether Tcf21⁺ cells can undergo lipofibroblast-to-myofibroblast conversion under pathological conditions (e.g. bronchopulmonary dysplasia or fibrosis) remains to be investigated.

Using a model for genetic cell depletion of Tcf21^{lin} in adult mice to investigate the effect of Tcf21⁺ cell reduction during neo-alveolarization, no significant alterations of the lung architecture were found in post-PNX mice that would indicate that Tcf21⁺ cells are essential for *de novo* septum formation. However, the depletion ratio of Tcf21⁺ cells achieved in this study was about 50%. Given that the *in vitro* experiments demonstrated a noticeable impairment in alveolosphere formation in complete absence of Tcf21⁺ cells, the lack of effect of Tcf21 lineage partial depletion on the structure of the lung after pneumonectomy could indicate that higher depletion rates are required to impair neo-alveolarization. Alternatively, the Tcf21 lineage might have a comparatively minor role in alveoli neo-formation *in vivo*, where many other cell-types are present with respect to the relatively simple co-culture model utilized by the author in the alveolosphere system. Admittedly, alternative depletion schemes such as longer induction-to-operation intervals, administration of higher doses of Tmx, postoperative induction of depletion, or assessment

at later time points could have lead to higher depletion of Tcf21⁺ cells. In any case, more efficient depletion models should be utilized in future studies to convincingly demonstrate whether or not lipofibroblasts play a relevant role in alveoli formation.

As a side note, depletion of Tcf21⁺ cells caused visible changes outside of the respiratory system: Tcf21⁺ cell-deficient mice 1) gained more weight than controls; 2) showed pronounced ascites; and 3) had abdominal fat tissue of abnormal characteristics. These three phenomena are likely to be related to each other, and given that Tcf21 expression has been identified in visceral adipose tissue (de Jong et al. 2015), the author speculates that depletion of Tcf21⁺ cells in the fat caused ascites (perhaps due to impairment of the oncotic gradient in the peritoneal cavity), and then accumulation of peritoneal fluid resulted in weight gain. It is evident that ascites contributed to the increased weight of Tcf21⁺-depleted mice; nonetheless, it is less clear whether or not the changes in the fat tissue caused ascites. Detailed characterization of the extra-pulmonary findings upon depletion of Tcf21⁺ cells and investigation of the causal mechanisms was out of the scope of the current work but communication of these findings might be of interest to researchers in other fields of study.

Finally, during the development of this study a work was published by Park et al., in which the authors describe some overlapping findings to those reported here. Using the same mouse strain used in most of the experiments presented here, Tcf21^{iCre};R26^{tdT}, the authors characterized the Tcf21 lineage, focusing heavily on embryonic development but also including experiments during postnatal development and with adult mice.

Because the report from Park et al. is closely related to the present work, The relevant results are summarized next: They showed that lineage-labeling at E9.5 resulted in labeling of mesenchymal cells at E19.5, these cells were predominantly found surrounding

proximal bronchioli while induction of recombination at several later timepoints (up to E15.5) resulted in the addition of labeling of progressively distal populations of mesenchymal cells. In agreement with the findings of the present work, Park and collaborators also reported that recombination in adult lungs induced labeling of mesenchymal cells throughout the lung parenchyma, including peribronchial and perivascular regions. Additionally, the labeled cells did not stain with antibodies against markers of non fibroblastic cell types such as cytokeratin, Hopx, Pro-SPC and CD31. Although in embryonic lungs, it was shown that some Tcf21⁺ cells, specially around E11.5 give rise to a portion of the vascular smooth muscle cells and bronchial smooth muscle cells. Less than 1% of lineage-labeled cells found at E18.5 that had been labeled at E14.5 and later were α -SMA⁺ cells in bronchi and vessels. At embryonic timepoints, the number of Tcf21^{lin} identified to express PDGFR- α (with anti-PDGFR- α antibody or by using PDGFR- α -GFP mice) was about 20-30%, while this number was higher (40-50%) in adults. Analysis of E18.5 ADRP-immunostained lungs following recombination at E9.5, E11.5 or E15.5 indicated that the Tcf21 lineage after E11.5 primarily contributes to the lipofibroblast population of the embryonic lung (~90% of the Tcf21^{lin} were also ADRP⁺). Similar findings regarding ADRP staining of the Tcf21 lineage were ascertained during postnatal lung development (labeling at P2, harvest at P14) and in adult mice (labeling at week 8, harvest at week 9), though a lower proportion (~75%) of Tcf21^{lin} were also ADRP⁺ in adult mice compared to previous time points. In the present work, similar observations were done upon ADRP staining of lungs during secondary alveolarization. Upon isolation of ribosomal-associated transcripts from the Tcf21-lineage, Park et al. showed that fibroblast gene transcripts such as Pdgfra, Vimentin and Col1a1 were enriched in Tcf21^{lin} of adult mice. Transcripts of the ADRP-encoding gene, Plin2, and Col13a1 were enriched in Tcf21^{lin} in both perinatal and adult mice, while other transcripts such as FGF10 and

Zfp423 were only enriched in Tcf21^{lin} of perinatal mice, and Thy1 and Desmin were only enriched in adult Tcf21^{lin}. In developing lungs Tcf21 expression peaked at P7. Park et al. also found that a high proportion (>60%) of Tcf21^{lin} in the distal lung contain lipid droplets in both P7 and 9-week old mice when labeling at P2 or 8 weeks, respectively. Presence of lipid droplets was also a recurrent finding at different postnatal time points and during neo-alveolarization in this study, but the prevalence of these lipid droplets found by the author of the present work in Tcf21^{lin} was generally higher than the figures reported by Park et al. A very important observation from Park was that overexpression of Tcf21 lead to increased fluorescence intensity upon LipidTOX staining in primary fibroblasts, suggesting that Tcf21 plays an active role in fibroblast lipid accumulation.

The data presented here allowed to reach similar conclusions to those of Park et al. with regard to the lipofibroblastic nature of the Tcf21 lineage. Furthermore, the 3D approach taken here to investigate the phenotype of Tcf21^{lin}, particularly during secondary septation and during homeostasis, allowed for a more precise evaluation of the ADRP-expressing and neutral lipid-containing cells. Likely because of this, the relative number of Tcf21^{lin} that contained ADRP or lipid droplets reported in the study from Park was lower than the values reported here. Thus, the results presented here might suggest an even more relevant role of Tcf21 in fibroblast lipid accumulation.

The present work differs from the one published by Park et al. in several ways: 1) While Park et al. focuses heavily on the characterization of the Tcf21 lineage in embryonic lungs, the present work focuses mainly in postnatal timepoints and includes neo-alveolarization; 2) This work described the morphology of adult Tcf21^{lin} and the relation of this cells with other cell types of the alveolus; and 3) While Park et al. established a causal role for Tcf21 in lipid accumulation, the present work investigated the role of Tcf21^{lin} in alveolarization processes. Undoubtedly the present work and that of Park et al. compliment each other

providing evidence of the close relation between Tcf21 expression and the appearance and maintenance of a lipidic phenotype in lung fibroblasts.

7. Conclusion

In summary, this work presents convincing evidence that the Tcf21 lineage in the lung parenchyma of mice represents cells of exclusively mesenchymal character, with lipofibroblastic phenotype based on localization, cell marker expression and neutral lipid droplet content. Tcf21^{lin} cells are, additionally, essentially distinct from the myofibroblasts that populate the lung during secondary septation. Tcf21^{lin} cells in adult mice were found to have a peculiar morphology with multiple slender cytoplasmic processes which contain lipid droplets and contact AEC2. Some of these processes were demonstrated to keep a close spatial relationship with alveolar capillary loops (Fig. 24). Stereological data failed to demonstrate a significant impact of Tcf21⁺ cell depletion on the architecture of the lung during lung regrowth upon pneumonectomy; however results from *in vitro* experiments suggested that the Tcf21 lineage might contribute to alveolarization. Alternate and more efficient depletion strategies could prove useful to clarify this conflict. Future studies on how Tcf21 expression in the lung parenchyma is linked to the generation or phenotypic maintenance of lipofibroblasts should be guaranteed. Finally, the expression pattern of Tcf21 in human lungs should be confirmed and studied. Currently, the existence of a human fibroblast subset equivalent to the rodent lipofibroblast by means of identification of interstitial lipid droplets is still controversial. Nevertheless, future identification of common molecular markers and pathways between rodent lipofibroblasts and human lung fibroblasts will enable exciting new possibilities regarding the use of translational approaches to study lung fibroblast biology.

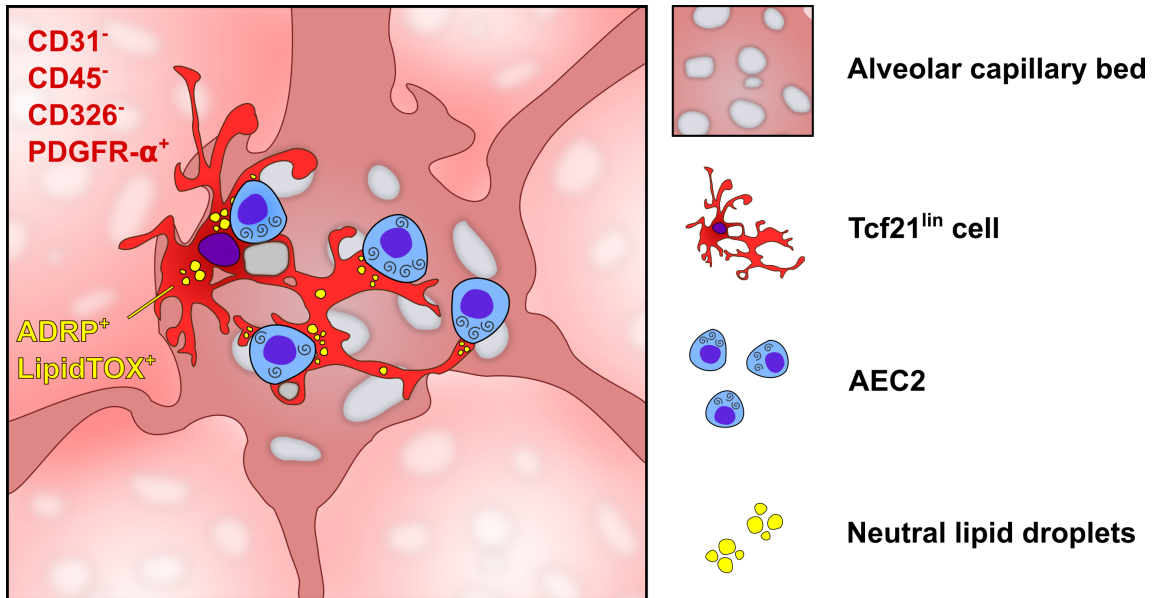


Figure 24. Prominent features of Tcf21^{lin} cells in murine alveoli. Schematic representation of the base of an alveolus *en face* and surrounding alveoli. Several characteristics of Tcf21^{lin} cells are displayed. In this study, it was demonstrated that Tcf21^{lin} cells in mice lungs are chiefly located to the alveolar compartment. Most of these cells display lipofibroblastic phenotype (CD31⁻CD45⁻CD326⁻PDGFR-α⁺, ADRP⁺, and LipidTOX⁺) and slender cytoplasmic processes that very often contact one or more alveolar epithelial type 2 cells (AEC2).

8. Summary

The transcription factor 21 (Tcf21) has been demonstrated to impact cardiac fibroblast differentiation, and is highly expressed in the lung mesenchyme. Tcf21 has been found to be essential for prenatal lung development, since global deletion of Tcf21 in mice results in abnormal lung morphology and early postnatal lethality. In contrast, formal characterization of the postnatal location, phenotype and function of Tcf21 in the lung had not been performed prior to the present study. Therefore, this study aimed to identify and characterize the phenotype and role of pulmonary Tcf21-expressing cells in mice during homeostasis, late lung development and in a model of pulmonary regrowth.

In this work, immunophenotyping of the Tcf21 lineage in lung tissue and lung cell suspensions of inducible reporter Tcf21^{iCre/+};R26^{tdTomato/tdTomato} mice resulted in convincing evidence that the pulmonary Tcf21 lineage of mice during postnatal development and in adult mice represents cells of exclusively mesenchymal character (CD31⁻CD45⁻CD326⁻PDGFR- α ⁺). Tcf21-lineage traced (Tcf21^{lin}) cells mostly held a lipofibroblastic phenotype based on localization, cell marker expression (ADRP⁺) and neutral lipid droplet content (LipidTOX⁺). Tcf21^{lin} cells were, in addition, essentially distinct from the myofibroblasts that populate the lung during secondary septation. After induction of lineage tracing in adult animals, Tcf21^{lin} cells were found to have a similar phenotype than postnatal Tcf21^{lin} cells. Moreover, Tcf21^{lin} cells were observed to have a peculiar morphology with multiple slender cytoplasmic processes which contain lipid droplets and contact alveolar epithelial cells type 2. Some of these processes kept a close spatial relationship with the border of alveolar capillary loops.

Left pneumonectomy was performed to induce compensatory regrowth in adult Tcf21^{iCre/+};R26^{tdT/DTA} mice following partial depletion of Tcf21^{lin} cells and in control Tcf21^{+/+};R26^{tdT/DTA} mice. Subsequent stereological analysis conducted 7 days after surgery failed to demonstrate a significant impact of preoperative Tcf21⁺ cell partial depletion on the architecture of the lung; however, results from *in vitro* experiments using alveolospheres indicated that Tcf21^{lin} cells contribute to alveolosphere formation, and that the Tcf21^{lin}-dependent support for sphere formation was at least partially mediated via soluble factors.

9. Zusammenfassung

Der Transkriptionsfaktor 21 (Tcf21) beeinflusst nach bisherigem Stand der Studien, die Differenzierung von kardialen Fibroblasten und ist im Lungenmesenchym hoch exprimiert ist. Auch für die pränatale Lungenentwicklung wurde gezeigt, dass TCF21 eine essentielle Rolle spielt, da eine globale Deletion von Tcf21 in Mäusen zu einer abnormalen Lungenmorphologie und zu einer frühen postnatalen Letalität führt. Eine genaue Charakterisierung der Lokalisation, des Phänotyps und der Funktion von Tcf21 positiven Zellen in der postnatalen und adulten Lunge wurde bis zu Beginn dieser Arbeit jedoch nicht durchgeführt. Daher war das Ziel dieser Studie, den Phänotyp und die Rolle der pulmonalen Tcf21-exprimierenden Zellen in Mäusen während der Homöostase, der späten Lungenentwicklung und in einem Modell des kompensatorischen Lungenwachstums zu identifizieren und zu charakterisieren.

In der vorliegenden Arbeit wurden mittels Immunphänotypisierung der Tcf21-Linie in Lungengewebe und in Lungenzellsuspensionen von Mäusen mit induzierbarem Reporter für TCF21, Tcf21^{iCre/+};R26^{tdTomato/tdTomato} überzeugende Beweise geliefert, dass die pulmonale Tcf21-Linie postnataler und adulter Mäuse einen ausschließlich mesenchymalen Charakter hat (CD31⁻CD45⁻CD326⁻PDGFR- α ⁺).

Basierend auf der Lokalisation, der Zellmarkerexpression (ADRP⁺) und dem Lipidtröpfchengehalt neutraler Lipide (LipidTOX⁺) wiesen Zellen der Tcf21-Linie (Tcf21^{lin}) meistens einen lipofibroblastischen Phänotyp auf. Darüberhinaus unterschieden sich Zellen der Tcf21^{lin} wesentlich von den Myofibroblasten, die während der Bildung sekundärer Septen in der Lunge vermehrt vorkommen. Markierung und Nachverfolgung der Tcf21^{lin} Zellen in adulten Mäusen zeigte, dass die Tcf21^{lin} Zellen adulter Mäuse einen ähnlichen Phänotyp wie Tcf21^{lin} Zellen postnataler Mäuse aufweisen. Zudem wurde

beobachtet, dass die Tcf21^{lin} Zellen eine besondere Morphologie mit multiplen schlanken zytoplasmatischen Ausstülpungen besitzen, die Lipidtröpfchen enthalten und in direktem Kontakt zu Alveolarepithelzellen Typ 2 stehen. Einige dieser zytoplasmatischen Ausstülpungen zeigten eine enge räumliche Beziehung zu dem Rand von Kapillarschlingen.

Um ein kompensatorisches Lungenwachstum in erwachsenen Tcf21^{iCre/+;R26^{tdT/DTA}}-Mäusen nach partieller Depletion von Tcf21^{lin} Zellen und in Kontroll-Tcf21^{+/+;R26^{tdT/DTA}}-Mäusen ohne Depletion von Tcf21^{lin} Zellen zu induzieren, wurde eine Pneumonektomie des linken Lungenflügels durchgeführt. Stereologische Analysen, die 7 Tage nach der Operation durchgeführt wurden, zeigten keinen signifikanten Einfluss der präoperativen partiellen Depletion der Tcf21^{lin} Zellen auf die Lungenstruktur im kompensatorischen Lungenwachstum. Ergebnisse von in-vitro Experimenten unter Verwendung von Alveolosphären deuteten jedoch daraufhin, dass Tcf21^{lin} Zellen zur Bildung von Alveolosphären beitragen und dass diese Tcf21^{lin}-abhängige Unterstützung der Sphärenbildung teilweise durch lösliche Faktoren vermittelt wurde.

10. References

- Abercrombie, M. 1978. "Fibroblasts." *Journal of Clinical Pathology. Supplement (Royal College of Pathologists)* 12: 1–6. <http://www.ncbi.nlm.nih.gov/pubmed/365883>.
- Acharya, Asha, Seung Tae Baek, Serena Banfi, Banu Eskiocak, and Michelle D. Tallquist. 2011. "Efficient Inducible Cre-Mediated Recombination in Tcf21 Cell Lineages in the Heart and Kidney." *Genesis* 49 (11): 870–77. <https://doi.org/10.1002/dvg.20750>.
- Acharya, Asha, Seung Tae Baek, Guo Huang, Banu Eskiocak, Sean Goetsch, Caroline Y. Sung, Serena Banfi, et al. 2012. "The BHLH Transcription Factor Tcf21 Is Required for Lineage-Specific EMT of Cardiac Fibroblast Progenitors." *Development* 139 (12): 2139–49. <https://doi.org/10.1242/dev.079970>.
- Addis, T. 1928. "COMPENSATORY HYPERTROPHY OF THE LUNG AFTER UNILATERAL PNEUMECTOMY." *The Journal of Experimental Medicine* 47 (1): 51–56. <https://doi.org/10.1084/jem.47.1.51>.
- Ahlbrecht, Katrin, and Stephen E. McGowan. 2014. "In Search of the Elusive Lipofibroblast in Human Lungs." *American Journal of Physiology-Lung Cellular and Molecular Physiology* 307 (8): L605–8. <https://doi.org/10.1152/ajplung.00230.2014>.
- Alam, D. Al, Elie El Agha, Reiko Sakurai, Vahid Kheirollahi, Alena Moiseenko, Soula Danopoulos, A. Shrestha, et al. 2015. "Evidence for the Involvement of Fibroblast Growth Factor 10 in Lipofibroblast Formation during Embryonic Lung Development." *Development* 142 (23): 4139–50. <https://doi.org/10.1242/dev.109173>.
- Allen, John F., and William Martin. 2007. "Out of Thin Air." *Nature* 445 (7128): 610–12. <https://doi.org/10.1038/445610a>.
- Barkauskas, Christina E., Mei-I Chung, Bryan Fioret, Xia Gao, Hiroaki Katsura, and Brigid L. M. Hogan. 2017. "Lung Organoids: Current Uses and Future Promise." *Development* 144 (6): 986–97. <https://doi.org/10.1242/dev.140103>.
- Barkauskas, Christina E., Michael J. Counce, Craig R. Rackley, Emily J. Bowie, Douglas R. Keene, Barry R. Stripp, Scott H. Randell, Paul W. Noble, and Brigid L.M. Hogan. 2013. "Type 2 Alveolar Cells Are Stem Cells in Adult Lung." *Journal of Clinical Investigation* 123 (7): 3025–36. <https://doi.org/10.1172/JCI68782>.
- Barron, Luke, Sina A. Gharib, and Jeremy S. Duffield. 2016. "Lung Pericytes and Resident Fibroblasts." *The American Journal of Pathology* 186 (10): 2519–31. <https://doi.org/10.1016/j.ajpath.2016.07.004>.
- Benton, M. 1995. "Diversification and Extinction in the History of Life." *Science* 268 (5207): 52–58. <https://doi.org/10.1126/science.7701342>.
- Besnard, Valérie, Susan E. Wert, Mildred T. Stahlman, Anthony D. Postle, Yan Xu, Machiko Ikegami, and Jeffrey A. Whitsett. 2009. "Deletion of Scap in Alveolar Type II

Cells Influences Lung Lipid Homeostasis and Identifies a Compensatory Role for Pulmonary Lipofibroblasts.” *Journal of Biological Chemistry* 284 (6): 4018–30. <https://doi.org/10.1074/jbc.M805388200>.

Boström, Hans, Amel Gritli-Linde, and Christer Betsholtz. 2002. “PDGF- α /PDGF Alpha-Receptor Signaling Is Required for Lung Growth and the Formation of Alveoli but Not for Early Lung Branching Morphogenesis.” *Developmental Dynamics* 223 (1): 155–62. <https://doi.org/10.1002/dvdy.1225>.

Boström, Hans, Karen Willetts, Milos Pekny, Per Levéen, Per Lindahl, Håkan Hedstrand, Marcela Pekna, et al. 1996. “PDGF-A Signaling Is a Critical Event in Lung Alveolar Myofibroblast Development and Alveogenesis.” *Cell* 85 (6): 863–73. [https://doi.org/10.1016/S0092-8674\(00\)81270-2](https://doi.org/10.1016/S0092-8674(00)81270-2).

Braitsch, Caitlin M., Michelle D. Combs, Susan E. Quaggin, and Katherine E. Yutzey. 2012. “Pod1/Tcf21 Is Regulated by Retinoic Acid Signaling and Inhibits Differentiation of Epicardium-Derived Cells into Smooth Muscle in the Developing Heart.” *Developmental Biology* 368 (2): 345–57. <https://doi.org/10.1016/j.ydbio.2012.06.002>.

Branchfield, Kelsey, Rongbo Li, Vlasta Lungova, Jamie M. Verheyden, David McCulley, and Xin Sun. 2016. “A Three-Dimensional Study of Alveologenesis in Mouse Lung.” *Developmental Biology* 409 (2): 429–41. <https://doi.org/10.1016/j.ydbio.2015.11.017>.

Brand-Saber, Beate E.M., and Thorsten Schäfer. 2014. “Trachea.” *Thoracic Surgery Clinics* 24 (1): 1–5. <https://doi.org/10.1016/j.thorsurg.2013.09.004>.

Breatnach, E., G. C. Abbott, and R. G. Fraser. 1984. “Dimensions of the Normal Human Trachea.” *American Journal of Roentgenology*. <https://doi.org/10.2214/ajr.142.5.903>.

Brody, J. S. 1985. “Cell-to-Cell Interactions in Lung Development.” *Pediatric Pulmonology* 1: S42–48. <https://europepmc.org/article/med/3906541>.

Burridge, Keith, and Magdalena Chrzanowska-Wodnicka. 1996. “FOCAL ADHESIONS, CONTRACTILITY, AND SIGNALING.” *Annual Review of Cell and Developmental Biology* 12 (1): 463–519. <https://doi.org/10.1146/annurev.cellbio.12.1.463>.

Butler, James P, Stephen H Loring, Samuel Patz, Akira Tsuda, Dmitriy a Yablonskiy, and Steven J Mentzer. 2012. “Evidence for Adult Lung Growth in Humans.” *New England Journal of Medicine* 367 (3): 244–47. <https://doi.org/10.1056/NEJMoa1203983>.

Cagle, Philip T., Claire Langston, and William M. Thurlbeck. 1988. “The Effect of Age on Postpneumonectomy Growth in Rabbits.” *Pediatric Pulmonology* 5 (2): 92–95. <https://doi.org/10.1002/ppul.1950050205>.

Charan, Nirmal B., William H. Thompson, and Paula Carvalho. 2007. “Functional Anatomy of Bronchial Veins.” *Pulmonary Pharmacology & Therapeutics* 20 (2): 100–103. <https://doi.org/10.1016/j.pupt.2006.03.004>.

- Chen, Leiling, Thomas Acciani, Tim Le Cras, Carolyn Lutzko, and Anne-Karina T Perl. 2012. "Dynamic Regulation of Platelet-Derived Growth Factor Receptor α Expression in Alveolar Fibroblasts during Realveolarization." *American Journal of Respiratory Cell and Molecular Biology* 47 (4): 517–27. <https://doi.org/10.1165/rcmb.2012-0030OC>.
- Ciric, I, MP Meyers, J Mayba, and NR Anthonisen. 2003. "Autopneumonectomy with Compensatory Lung Growth." *Canadian Respiratory Journal* 10 (5): 271–73. <https://doi.org/10.1155/2003/853729>.
- Cohn, Roy. 1939. "Factors Affecting the Postnatal Growth of the Lung." *The Anatomical Record* 75 (2): 195–205. <https://doi.org/10.1002/ar.1090750206>.
- Desmoulière, A, M Redard, I Darby, and G Gabbiani. 1995. "Apoptosis Mediates the Decrease in Cellularity during the Transition between Granulation Tissue and Scar." *The American Journal of Pathology* 146 (1): 56–66. <http://www.ncbi.nlm.nih.gov/pubmed/7856739%0Ahttp://www.pubmedcentral.nih.gov/articlerender.fcgi?artid=PMC1870783>.
- Desmoulière, Alexis, Ian A Darby, and Giulio Gabbiani. 2003. "Normal and Pathologic Soft Tissue Remodeling: Role of the Myofibroblast, with Special Emphasis on Liver and Kidney Fibrosis." *Laboratory Investigation* 83 (12): 1689–1707. <https://doi.org/10.1097/01.LAB.0000101911.53973.90>.
- Eddy, R J, J A Petro, and J J Tomasek. 1988. "Evidence for the Nonmuscle Nature of the 'Myofibroblast' of Granulation Tissue and Hypertrophic Scar. An Immunofluorescence Study." *The American Journal of Pathology* 130 (2): 252–60. <http://www.ncbi.nlm.nih.gov/pubmed/3277440>.
- El Agha, Elie, Rafael Kramann, Rebekka K. Schneider, Xiaokun Li, Werner Seeger, Benjamin D. Humphreys, and Saverio Bellusci. 2017. "Mesenchymal Stem Cells in Fibrotic Disease." *Cell Stem Cell* 21 (2): 166–77. <https://doi.org/10.1016/j.stem.2017.07.011>.
- El Agha, Elie, Alena Moiseenko, Vahid Kheirollahi, Stijn De Langhe, Slaven Crnkovic, Grazyna Kwapiszewska, Marten Szibor, et al. 2017. "Two-Way Conversion between Lipogenic and Myogenic Fibroblastic Phenotypes Marks the Progression and Resolution of Lung Fibrosis." *Cell Stem Cell* 20 (2): 261-273.e3. <https://doi.org/10.1016/j.stem.2016.10.004>.
- Ellis, Harold. 2005. "Lungs: Blood Supply, Lymphatic Drainage and Nerve Supply." *Anaesthesia & Intensive Care Medicine* 6 (11): 362. <https://doi.org/10.1383/anes.2005.6.11.362>.
- Fehrenbach, H., R. Voswinckel, V. Michl, T. Mehling, A. Fehrenbach, W. Seeger, and J. R. Nyengaard. 2008. "Neoalveolarisation Contributes to Compensatory Lung Growth Following Pneumonectomy in Mice." *European Respiratory Journal* 31 (3): 515–22. <https://doi.org/10.1183/09031936.00109407>.

- Gandjeva, Aneta, and Rubin M. Tuder. 2018. "Lung Histological Methods." In *Methods in Molecular Biology*, 1809:315–29. https://doi.org/10.1007/978-1-4939-8570-8_20.
- Graham, Jeffrey B., Nancy M. Aguilar, Robert Dudley, and Carl Gans. 1995. "Implications of the Late Palaeozoic Oxygen Pulse for Physiology and Evolution." *Nature* 375 (6527): 117–20. <https://doi.org/10.1038/375117a0>.
- Gurtner, Geoffrey C, Sabine Werner, Yann Barrandon, and Michael T Longaker. 2008. "Wound Repair and Regeneration." *Nature* 453 (7193): 314–21. <https://doi.org/10.1038/nature07039>.
- Habel, David M, and Cory M Hogaboam. 2017. "Heterogeneity of Fibroblasts and Myofibroblasts in Pulmonary Fibrosis." *Current Pathobiology Reports* 5 (2): 101–10. <https://doi.org/10.1007/s40139-017-0134-x>.
- Hagood, James S, Priya Prabhakaran, Pallavi Kumbla, Lorena Salazar, Mark W MacEwen, Thomas H Barker, Luis A Ortiz, et al. 2005. "Loss of Fibroblast Thy-1 Expression Correlates with Lung Fibrogenesis." *The American Journal of Pathology* 167 (2): 365–79. [https://doi.org/10.1016/S0002-9440\(10\)62982-3](https://doi.org/10.1016/S0002-9440(10)62982-3).
- Hinz, Boris, Giuseppe Celetta, James J. Tomasek, Giulio Gabbiani, and Christine Chaponnier. 2001. "Alpha-Smooth Muscle Actin Expression Upregulates Fibroblast Contractile Activity." Edited by Paul T. Matsudaira. *Molecular Biology of the Cell* 12 (9): 2730–41. <https://doi.org/10.1091/mbc.12.9.2730>.
- Holmes, C. Thurlbeck, W.M. 1979. "Normal Lung Growth and Response after Pneumonectomy in Rats at Various Ages" *The American Review of Respiratory Disease* 120 (5): 1125–36. <https://doi.org/10.1164/arrd.1979.120.5.1125>.
- Hsia, C. C W. 2006. "Quantitative Morphology of Compensatory Lung Growth." *European Respiratory Review* 15 (101): 148–56. <https://doi.org/10.1183/09059180.00010105>.
- Hsia, Connie C. W., Dallas M. Hyde, Matthias Ochs, and Ewald R. Weibel. 2010. "An Official Research Policy Statement of the American Thoracic Society/European Respiratory Society: Standards for Quantitative Assessment of Lung Structure." *American Journal of Respiratory and Critical Care Medicine* 181 (4): 394–418. <https://doi.org/10.1164/rccm.200809-1522ST>.
- Hsia, Connie C. W., Anke Schmitz, Markus Lambertz, Steven F. Perry, and John N. Maina. 2013. "Evolution of Air Breathing: Oxygen Homeostasis and the Transitions from Water to Land and Sky." In *Comprehensive Physiology*, 3:849–915. Hoboken, NJ, USA: John Wiley & Sons, Inc. <https://doi.org/10.1002/cphy.c120003>.
- Hsia, Connie C.W. 2004. "Lessons from a Canine Model of Compensatory Lung Growth." In *Current Topics in Developmental Biology*, 64:17–32. [https://doi.org/10.1016/S0070-2153\(04\)64002-6](https://doi.org/10.1016/S0070-2153(04)64002-6).

- Ibrahim, Mohamed M, Lei Chen, Jennifer E Bond, Manuel A Medina, Licheng Ren, George Kokosis, Angelica M Selim, and Howard Levinson. 2015. "Myofibroblasts Contribute to but Are Not Necessary for Wound Contraction." *Laboratory Investigation* 95 (12): 1429–38. <https://doi.org/10.1038/labinvest.2015.116>.
- Jong, Jasper M. A. de, Ola Larsson, Barbara Cannon, and Jan Nedergaard. 2015. "A Stringent Validation of Mouse Adipose Tissue Identity Markers." *American Journal of Physiology-Endocrinology and Metabolism* 308 (12): E1085–1105. <https://doi.org/10.1152/ajpendo.00023.2015>.
- Kanisicak, Onur, Hadi Khalil, Malina J. Ivey, Jason Karch, Bryan D. Maliken, Robert N. Correll, Matthew J. Brody, et al. 2016. "Genetic Lineage Tracing Defines Myofibroblast Origin and Function in the Injured Heart." *Nature Communications* 7 (1): 12260. <https://doi.org/10.1038/ncomms12260>.
- Kaplan, Nancy B, Margaret M Grant, and Jerome S Brody. 1985. "The Lipid Interstitial Cell of the Pulmonary Alveolus. Age and Species Differences." *Am Rev Respir Dis* 132 (6): L1307–12. <https://doi.org/10.1164/arrd.1985.132.6.1307>.
- Komuro, Terumasa. 1990. "Re-Evaluation of Fibroblasts and Fibroblast-like Cells." *Anatomy and Embriology*.
- Lai-Fook, Stephen J. 2004. "Pleural Mechanics and Fluid Exchange." *Physiological Reviews* 84 (2): 385–410. <https://doi.org/10.1152/physrev.00026.2003>.
- Laros, C.D., and C.J.J. Westermann. 1987. "Dilatation, Compensatory Growth, or Both after Pneumonectomy during Childhood and Adolescence." *The Journal of Thoracic and Cardiovascular Surgery* 93 (4): 570–76. [https://doi.org/10.1016/S0022-5223\(19\)36386-X](https://doi.org/10.1016/S0022-5223(19)36386-X).
- Lazcano, A., J. Oró, and Stanley L. Miller. 1983. "Primitive Earth Environments: Organic Syntheses and the Origin and Early Evolution of Life." In *Developments in Precambrian Geology*, 7:151–74. [https://doi.org/10.1016/S0166-2635\(08\)70246-9](https://doi.org/10.1016/S0166-2635(08)70246-9).
- Lechner, Andrew J., Ian H. Driver, Jinwoo Lee, Carmen M. Conroy, Abigail Nagle, Richard M. Locksley, and Jason R. Rock. 2017. "Recruited Monocytes and Type 2 Immunity Promote Lung Regeneration Following Pneumonectomy." *Cell Stem Cell* 21 (1): 120-134.e7. <https://doi.org/10.1016/j.stem.2017.03.024>.
- Lo, Chun-Min, Denis B Buxton, Gregory C H Chua, Micah Dembo, Robert S Adelstein, and Yu-Li Wang. 2004. "Nonmuscle Myosin IIb Is Involved in the Guidance of Fibroblast Migration." *Molecular Biology of the Cell* 15 (3): 982–89. <https://doi.org/10.1091/mbc.e03-06-0359>.
- Lu, Jianrong, Priscilla Chang, James A. Richardson, Lin Gan, Hartmut Weiler, and Eric N. Olson. 2000. "The Basic Helix-Loop-Helix Transcription Factor Capsulin Controls Spleen Organogenesis." *Proceedings of the National Academy of Sciences* 97 (17): 9525–30. <https://doi.org/10.1073/pnas.97.17.9525>.

- Madisen, Linda, Theresa A. Zwingman, Susan M. Sunkin, Seung Wook Oh, Hatim A. Zariwala, Hong Gu, Lydia L. Ng, et al. 2010. "A Robust and High-Throughput Cre Reporting and Characterization System for the Whole Mouse Brain." *Nature Neuroscience* 13 (1): 133–40. <https://doi.org/10.1038/nn.2467>.
- Maezawa, Yoshiro, Tuncer Onay, Rizaldy P. Scott, Lindsay S. Keir, Henrik Dimke, Chengjin Li, Vera Eremina, et al. 2014. "Loss of the Podocyte-Expressed Transcription Factor Tcf21/Pod1 Results in Podocyte Differentiation Defects and FSGS." *Journal of the American Society of Nephrology* 25 (11): 2459–70. <https://doi.org/10.1681/ASN.2013121307>.
- Maina, J. N. 2002. "Structure, Function and Evolution of the Gas Exchangers: Comparative Perspectives." *Journal of Anatomy* 201 (4): 281–304. <https://doi.org/10.1046/j.1469-7580.2002.00099.x>.
- Maina, J N. 1994. "Comparative Pulmonary Morphology and Morphometry: The Functional Design of Respiratory Systems." In *Advances in Comparative and Environmental Physiology*, 20:111–232. Springer, Berlin, Heidelberg. https://doi.org/10.1007/978-3-642-78598-6_4.
- Maksvytis, H J, C Vaccaro, and J S Brody. 1981. "Isolation and Characterization of the Lipid-Containing Interstitial Cell from the Developing Rat Lung." *Laboratory Investigation; a Journal of Technical Methods and Pathology* 45 (3): 248–59. <http://www.ncbi.nlm.nih.gov/pubmed/7278133>.
- Massaro, Donald, and Gloria DeCarlo Massaro. 2010. "Lung Development, Lung Function, and Retinoids." *New England Journal of Medicine* 362 (19): 1829–31. <https://doi.org/10.1056/NEJMe1002366>.
- McAnulty, Robin J. 2007. "Fibroblasts and Myofibroblasts: Their Source, Function and Role in Disease." *The International Journal of Biochemistry & Cell Biology* 39 (4): 666–71. <https://doi.org/10.1016/j.biocel.2006.11.005>.
- McGowan, S. E., M. M. Doro, and S. K. Jackson. 1997. "Endogenous Retinoids Increase Perinatal Elastin Gene Expression in Rat Lung Fibroblasts and Fetal Explants." *American Journal of Physiology-Lung Cellular and Molecular Physiology* 273 (2): L410–16. <https://doi.org/10.1152/ajplung.1997.273.2.L410>.
- McGowan, S.E., and A.J. Holmes. 2007. "Vitamin A Deficiency Alters Pulmonary Parenchymal Collagen and Tissue Mechanics." *Respiratory Physiology & Neurobiology* 156 (3): 312–19. <https://doi.org/10.1016/j.resp.2006.11.008>.
- McGowan, Stephen E., and Diann M. McCoy. 2014. "Regulation of Fibroblast Lipid Storage and Myofibroblast Phenotypes during Alveolar Septation in Mice." *American Journal of Physiology-Lung Cellular and Molecular Physiology* 307 (8): L618–31. <https://doi.org/10.1152/ajplung.00144.2014>.

- McGowan, Stephen E, Ruth E Grossmann, Patricia W Kimani, and Amey J Holmes. 2008. "Platelet-Derived Growth Factor Receptor-Alpha-Expressing Cells Localize to the Alveolar Entry Ring and Have Characteristics of Myofibroblasts During Pulmonary Alveolar Septal Formation." *The Anatomical Record: Advances in Integrative Anatomy and Evolutionary Biology* 291 (October): 1649–61. <https://doi.org/10.1002/ar.20764>.
- McGowan, Stephen E, and John S Torday. 1997. "THE PULMONARY LIPOFIBROBLAST (LIPID INTERSTITIAL CELL) AND ITS CONTRIBUTIONS TO ALVEOLAR DEVELOPMENT." *Annual Review of Physiology* 59 (1): 43–62. <https://doi.org/10.1146/annurev.physiol.59.1.43>.
- McQualter, Jonathan L, Rosa C. McCarty, Joanne Van der Velden, Robert J.J. O'Donoghue, Marie-Liesse Asselin-Labat, Steven Bozinovski, and Ivan Bertoncello. 2013. "TGF- β Signaling in Stromal Cells Acts Upstream of FGF-10 to Regulate Epithelial Stem Cell Growth in the Adult Lung." *Stem Cell Research* 11 (3): 1222–33. <https://doi.org/10.1016/j.scr.2013.08.007>.
- Nadkarni, Rohan R., Soumeya Abed, and Jonathan S. Draper. 2016. "Organoids as a Model System for Studying Human Lung Development and Disease." *Biochemical and Biophysical Research Communications* 473 (3): 675–82. <https://doi.org/10.1016/j.bbrc.2015.12.091>.
- Nakajima, C., C. Kijimoto, Y. Yokoyama, T. Miyakawa, Y. Tsuchiya, T. Kuroda, M. Nakano, and M. Saeki. 1998. "Longitudinal Follow-up of Pulmonary Function after Lobectomy in Childhood - Factors Affecting Lung Growth." *Pediatric Surgery International* 13 (5–6): 341–45. <https://doi.org/10.1007/s003830050334>.
- Ntokou, Aglaia, Friederike Klein, Daria Dontireddy, Sven Becker, Saverio Bellusci, William D Richardson, Marten Szibor, et al. 2015. "Characterization of the Platelet-Derived Growth Factor Receptor- α -Positive Cell Lineage during Murine Late Lung Development." *American Journal of Physiology. Lung Cellular and Molecular Physiology* 309 (9): L942–58. <https://doi.org/10.1152/ajplung.00272.2014>.
- Ntokou, Aglaia, Marten Szibor, José Alberto Rodríguez-Castillo, Jennifer Quantius, Susanne Herold, Elie El Agha, Saverio Bellusci, et al. 2017. "A Novel Mouse Cre-Driver Line Targeting Perilipin 2-Expressing Cells in the Neonatal Lung." *Genesis* 55 (12): e23080. <https://doi.org/10.1002/dvg.23080>.
- O'Hare, Karen Hitchcock, and Michael N. Sheridan. 1970. "Electron Microscopic Observations on the Morphogenesis of the Albino Rat Lung, with Special Reference to Pulmonary Epithelial Cells." *American Journal of Anatomy* 127 (2): 181–205. <https://doi.org/10.1002/aja.1001270205>.
- Ochs, Matthias, Jens R. Nyengaard, Anja Jung, Lars Knudsen, Marion Voigt, Thorsten Wahlers, Joachim Richter, and Hans Jørgen G. Gundersen. 2004. "The Number of Alveoli in the Human Lung." *American Journal of Respiratory and Critical Care Medicine* 169 (1): 120–24. <https://doi.org/10.1164/rccm.200308-1107OC>.

- Packard, Gary C. 1974. "THE EVOLUTION OF AIR-BREATHING IN PALEOZOIC GNATHOSTOME FISHES." *Evolution* 28 (2): 320–25. <https://doi.org/10.1111/j.1558-5646.1974.tb00751.x>.
- Paisley, Derek, Luke Bevan, Katherine J Choy, and Carina Gross. 2013. "The Pneumonectomy Model of Compensatory Lung Growth: Insights into Lung Regeneration." *Pharmacology and Therapeutics*. <https://doi.org/10.1016/j.pharmthera.2013.12.006>.
- Pan, Xiaoqing, Norio Suzuki, Ikuo Hirano, Shun Yamazaki, Naoko Minegishi, and Masayuki Yamamoto. 2011. "Isolation and Characterization of Renal Erythropoietin-Producing Cells from Genetically Produced Anemia Mice." *PLoS ONE* 6 (10): e25839. <https://doi.org/10.1371/journal.pone.0025839>.
- Park, Juwon, Malina J. Ivey, Yanik Deana, Kara L. Riggsbee, Emelie Sørensen, Veronika Schwabl, Caroline Sjöberg, et al. 2019. "The Tcf21 Lineage Constitutes the Lung Lipofibroblast Population." *American Journal of Physiology - Lung Cellular and Molecular Physiology*. <https://doi.org/10.1152/ajplung.00254.2018>.
- Parker, James C. 2011. "Acute Lung Injury and Pulmonary Vascular Permeability: Use of Transgenic Models." In *Comprehensive Physiology*, 1:835–82. Hoboken, NJ, USA: John Wiley & Sons, Inc. <https://doi.org/10.1002/cphy.c100013>.
- Pastuła, Agnieszka, and Janusz Marcinkiewicz. 2019. "Cellular Interactions in the Intestinal Stem Cell Niche." *Archivum Immunologiae et Therapiae Experimentalis* 67 (1): 19–26. <https://doi.org/10.1007/s00005-018-0524-8>.
- Paxson, Julia A., Alisha Gruntman, Christopher D. Parkin, Melissa R. Mazan, Airiell Davis, Edward P. Ingenito, and Andrew M. Hoffman. 2011. "Age-Dependent Decline in Mouse Lung Regeneration with Loss of Lung Fibroblast Clonogenicity and Increased Myofibroblastic Differentiation." *PLoS ONE* 6 (8): e23232. <https://doi.org/10.1371/journal.pone.0023232>.
- Pozarska, Agnieszka, José Alberto Rodríguez-Castillo, David E. Surate Solaligue, Aglaia Ntokou, Philipp Rath, Ivana Mižíková, Alicia Madurga, et al. 2017. "Stereological Monitoring of Mouse Lung Alveolarization from the Early Postnatal Period to Adulthood." *American Journal of Physiology-Lung Cellular and Molecular Physiology* 312 (6): L882–95. <https://doi.org/10.1152/ajplung.00492.2016>.
- Quaggin, S E, L Schwartz, S Cui, P Igarashi, J Deimling, M Post, and J Rossant. 1999. "The Basic-Helix-Loop-Helix Protein Pod1 Is Critically Important for Kidney and Lung Organogenesis." *Development (Cambridge, England)* 126 (24): 5771–83. <https://doi.org/10.1242/dev.01266>.
- Raup, David M. 1979. "Size of the Permo-Triassic Bottleneck and Its Evolutionary Implications." *Science* 206 (4415): 217–18. <https://doi.org/10.1126/science.206.4415.217>.

- Rawlins, Emma L., and Anne Karina Perl. 2012. "The a"MAZE"ing World of Lung-Specific Transgenic Mice." *American Journal of Respiratory Cell and Molecular Biology* 46 (3): 269–82. <https://doi.org/10.1165/rcmb.2011-0372PS>.
- Rehan, Virender K., Sharon Sugano, Ying Wang, Jamie Santos, Sonia Romero, Chiranjib Dasgupta, Michael P. Keane, Mildred T. Stahlman, and John S. Torday. 2006. "EVIDENCE FOR THE PRESENCE OF LIPOFIBROBLASTS IN HUMAN LUNG." *Experimental Lung Research* 32 (8): 379–93. <https://doi.org/10.1080/01902140600880257>.
- Rockey, Don C, P Darwin Bell, and Joseph a Hill. 2015. "Fibrosis — A Common Pathway to Organ Injury and Failure." Edited by Dan L. Longo. *New England Journal of Medicine* 372 (12): 1138–49. <https://doi.org/10.1056/NEJMra1300575>.
- Rodríguez-Castillo, José Alberto, David Bravo Pérez, Aglaia Ntokou, Werner Seeger, Rory E. Morty, and Katrin Ahlbrecht. 2018. "Understanding Alveolarization to Induce Lung Regeneration." *Respiratory Research* 19 (1): 148. <https://doi.org/10.1186/s12931-018-0837-5>.
- Sánchez Alvarado, Alejandro. 2006. "Planarian Regeneration: Its End Is Its Beginning." *Cell* 124 (2): 241–45. <https://doi.org/10.1016/j.cell.2006.01.012>.
- Sandbo, N., L. V. Smolyaninova, S. N. Orlov, and N. O. Dulin. 2016. "Control of Myofibroblast Differentiation and Function by Cytoskeletal Signaling." *Biochemistry (Moscow)* 81 (13): 1698–1708. <https://doi.org/10.1134/S0006297916130071>.
- Sandbo, Nathan, and Nickolai Dulin. 2011. "Actin Cytoskeleton in Myofibroblast Differentiation: Ultrastructure Defining Form and Driving Function." *Translational Research: The Journal of Laboratory and Clinical Medicine* 158 (4): 181–96. <https://doi.org/10.1016/j.trsl.2011.05.004>.
- Seifert, Ashley W., and Ken Muneoka. 2018. "The Blastema and Epimorphic Regeneration in Mammals." *Developmental Biology* 433 (2): 190–99. <https://doi.org/10.1016/j.ydbio.2017.08.007>.
- Sorokin, Sergei, Helen A. Padykula, and Edith Herman. 1959. "Comparative Histochemical Patterns in Developing Mammalian Lungs." *Developmental Biology* 1 (2): 125–51. [https://doi.org/10.1016/0012-1606\(59\)90023-5](https://doi.org/10.1016/0012-1606(59)90023-5).
- Sorrell, J. Michael, Marilyn A. Baber, and Arnold I. Caplan. 2007. "Clonal Characterization of Fibroblasts in the Superficial Layer of the Adult Human Dermis." *Cell and Tissue Research* 327 (3): 499–510. <https://doi.org/10.1007/s00441-006-0317-y>.
- Sorrell, J. Michael, and Arnold I. Caplan. 2009. "Chapter 4 Fibroblasts—A Diverse Population at the Center of It All." *International Review of Cell and Molecular Biology* 276 (January): 161–214. [https://doi.org/10.1016/S1937-6448\(09\)76004-6](https://doi.org/10.1016/S1937-6448(09)76004-6).

- Spit, B. J. 1983. "Induction of Lipid Droplets in Fibroblasts of the Hamster Lung by a Diet High in Vitamin A." *Experimental Lung Research* 4 (4): 247–57. <https://doi.org/10.3109/01902148309055012>.
- Stamati, Katerina, Vivek Mudera, and Umber Cheema. 2011. "Evolution of Oxygen Utilization in Multicellular Organisms and Implications for Cell Signalling in Tissue Engineering." *Journal of Tissue Engineering* 2 (1): 204173141143236. <https://doi.org/10.1177/2041731411432365>.
- Stanley, Steven M. 2016. "Estimates of the Magnitudes of Major Marine Mass Extinctions in Earth History PNAS PLUS." <https://doi.org/10.1073/pnas.1613094113>.
- Stiles, Q. R., B. W. Meyer, G. G. Lindesmith, and J. C. Jones. 1969. "The Effects of Pneumonectomy in Children." *Journal of Thoracic and Cardiovascular Surgery*. [https://doi.org/10.1016/0022-3468\(70\)90535-x](https://doi.org/10.1016/0022-3468(70)90535-x).
- Suarez, Carlos Jose, Suzanne M Dintzis, and Charles W Frevert. 2012. "Respiratory." In *Comparative Anatomy and Histology*, 121–34. Elsevier. <https://doi.org/10.1016/B978-0-12-381361-9.00009-3>.
- Swonger, Jessica M, Jocelyn S Liu, Malina J Ivey, and Michelle D Tallquist. 2016. "Genetic Tools for Identifying and Manipulating Fibroblasts in the Mouse." *Differentiation* 92 (3): 66–83. <https://doi.org/10.1016/j.diff.2016.05.009>.
- Tahedl, Daniel, André Wirkes, Stefan A. Tschanz, Matthias Ochs, and Christian Mühlfeld. 2014. "How Common Is the Lipid Body-Containing Interstitial Cell in the Mammalian Lung?" *American Journal of Physiology-Lung Cellular and Molecular Physiology* 307 (5): L386–94. <https://doi.org/10.1152/ajplung.00131.2014>.
- Taub, Rebecca. 2004. "Liver Regeneration: From Myth to Mechanism." *Nature Reviews Molecular Cell Biology* 5 (10): 836–47. <https://doi.org/10.1038/nrm1489>.
- Terwilliger, N B. 1998. "Functional Adaptations of Oxygen-Transport Proteins." *Journal of Experimental Biology* 201 (8): 1085–98.
- Thane, Kristen, Edward P Ingenito, and Andrew M Hoffman. 2014. "Lung Regeneration and Translational Implications of the Postpneumonectomy Model." *Translational Research* 163 (4): 363–76. <https://doi.org/10.1016/j.trsl.2013.11.010>.
- Tomashefski, Joseph F, and Carol F Farver. 2008. "Anatomy and Histology of the Lung." In *Dail and Hammar's Pulmonary Pathology*, 1:20–48. New York, NY: Springer New York. https://doi.org/10.1007/978-0-387-68792-6_2.
- Torday, J., Ji Hua, and Richard Slavin. 1995. "Metabolism and Fate of Neutral Lipids of Fetal Lung Fibroblast Origin." *Biochimica et Biophysica Acta (BBA) - Lipids and Lipid Metabolism* 1254 (2): 198–206. [https://doi.org/10.1016/0005-2760\(94\)00184-Z](https://doi.org/10.1016/0005-2760(94)00184-Z).
- Torday, J. S., E. Torres, and V. K. Rehan. 2003. "The Role of Fibroblast Transdifferentiation in Lung Epithelial Cell Proliferation, Differentiation, and Repair in Vitro." *Pediatric*

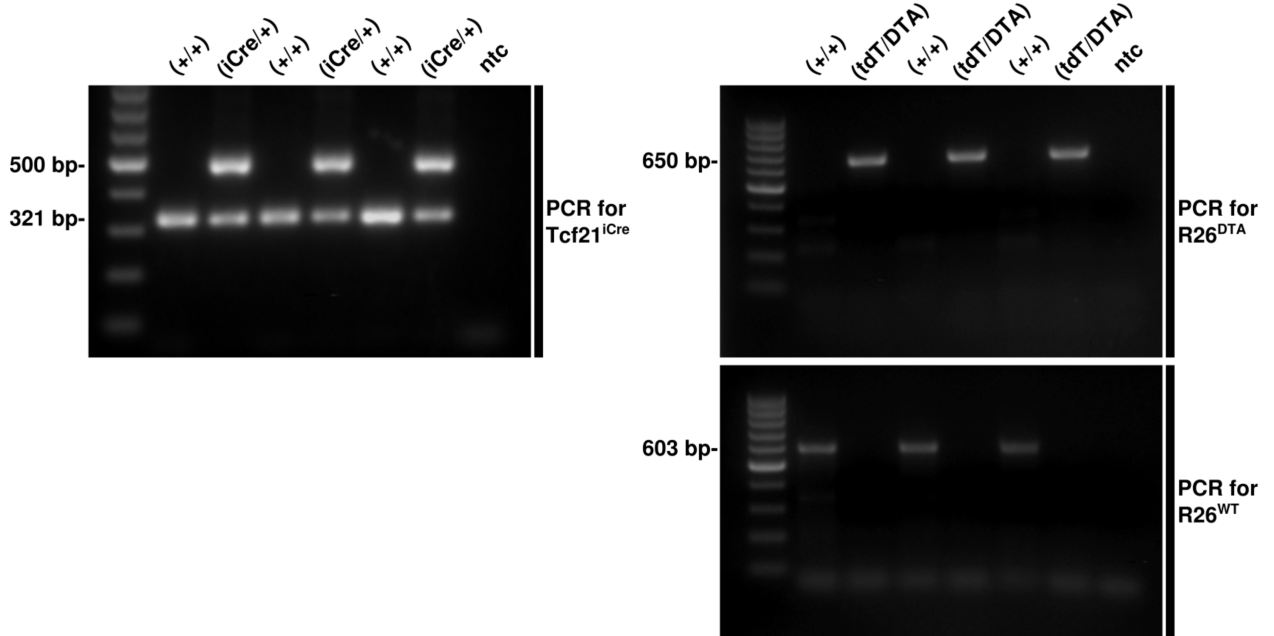
Pathology and Molecular Medicine 22 (3): 189–207.
<https://doi.org/10.1080/15227950307732>.

- Vaccaro, Charles, and Jerome S Brody. 1978. "Ultrastructure of Developing Alveoli."
- Varisco, Brian M, Namasivayam Ambalavanan, Jeffrey A Whitsett, and James S Hagood. 2012. "Thy-1 Signals through PPAR γ to Promote Lipofibroblast Differentiation in the Developing Lung." *American Journal of Respiratory Cell and Molecular Biology* 46 (6): 765–72. <https://doi.org/10.1165/rcmb.2011-0316OC>.
- Voehringer, David, Hong-Erh Liang, and Richard M. Locksley. 2008. "Homeostasis and Effector Function of Lymphopenia-Induced 'Memory-Like' T Cells in Constitutively T Cell-Depleted Mice." *The Journal of Immunology*. <https://doi.org/10.4049/jimmunol.180.7.4742>.
- Voswinckel, R. 2004. "Characterisation of Post-Pneumonectomy Lung Growth in Adult Mice." *European Respiratory Journal* 24 (4): 524–32. <https://doi.org/10.1183/09031936.04.10004904>.
- Wake, Kenjiro. 1971. "'Sternzellen' in the Liver: Perisinusoidal Cells with Special Reference to Storage of Vitamin A." *American Journal of Anatomy* 132 (4): 429–61. <https://doi.org/10.1002/aja.1001320404>.
- Wansleeben, Carolien, Christina E. Barkauskas, Jason R. Rock, and Brigid L. M. Hogan. 2013. "Stem Cells of the Adult Lung: Their Development and Role in Homeostasis, Regeneration, and Disease." *Wiley Interdisciplinary Reviews: Developmental Biology* 2 (1): 131–48. <https://doi.org/10.1002/wdev.58>.
- Weibel, E. R. 2015. "On the Tricks Alveolar Epithelial Cells Play to Make a Good Lung." *American Journal of Respiratory and Critical Care Medicine* 191 (5): 504–13. <https://doi.org/10.1164/rccm.201409-1663OE>.
- Weibel, Ewald R. 1974. "On Pericytes, Particularly Their Existence on Lung Capillaries." *Microvascular Research* 8 (2): 218–35. [https://doi.org/10.1016/0026-2862\(74\)90096-X](https://doi.org/10.1016/0026-2862(74)90096-X).
- Weibel, Ewald R. 1963. *Morphometry of the Human Lung*. 1st ed. Berlin, Heidelberg: Springer Berlin Heidelberg. <https://doi.org/10.1007/978-3-642-87553-3>.
- Werner, Heinrich A, Gordon E Pirie, Helen R Nadel, Arlen G Fleisher, and Jacques G LeBlanc. 1993. "Lung Volumes, Mechanics, and Perfusion after Pulmonary Resection in Infancy." *The Journal of Thoracic and Cardiovascular Surgery* 105 (4): 737–42. [https://doi.org/10.1016/S0022-5223\(19\)34202-3](https://doi.org/10.1016/S0022-5223(19)34202-3).
- Willführ, Alper, Christina Brandenberger, Tanja Piatkowski, Roman Grothausmann, Jens Randel Nyengaard, Matthias Ochs, and Christian Mühlfeld. 2015. "Estimation of the Number of Alveolar Capillaries by the Euler Number (Euler-Poincaré Characteristic)."

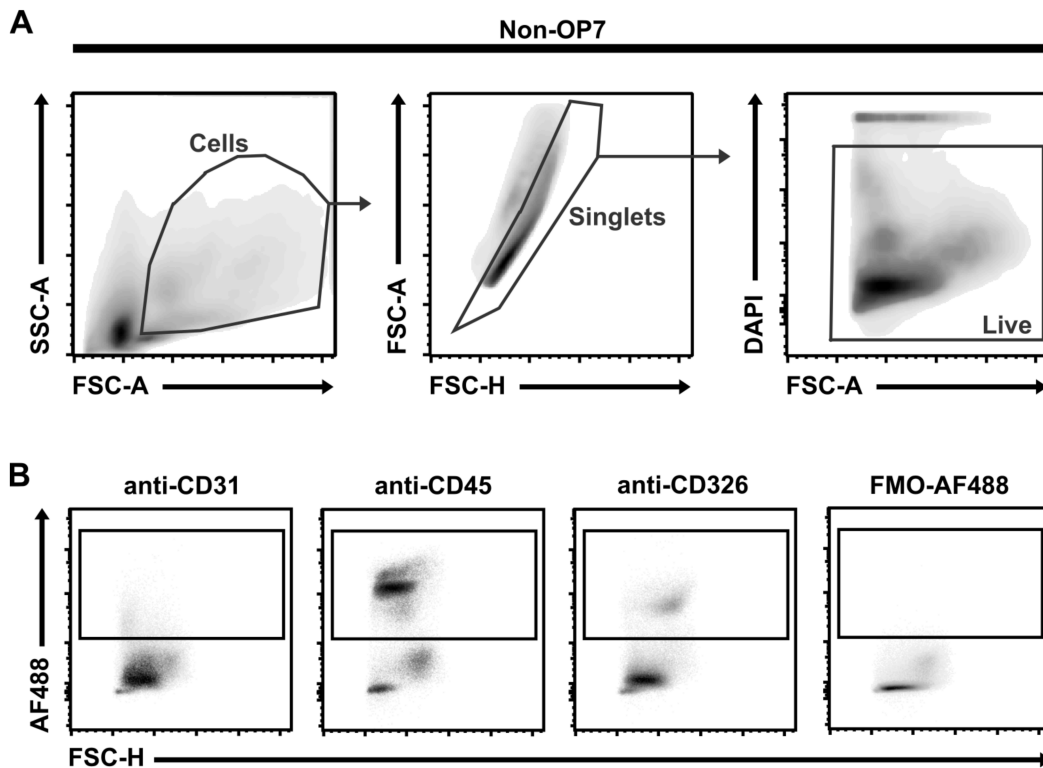
American Journal of Physiology-Lung Cellular and Molecular Physiology 309 (11): L1286–93. <https://doi.org/10.1152/ajplung.00410.2014>.

Zeisberg, Michael, and Raghu Kalluri. 2015. "Physiology of the Renal Interstitium." *Clinical Journal of the American Society of Nephrology* 10 (10): 1831–40. <https://doi.org/10.2215/CJN.00640114>.

11. Appendix



Appendix 1. Example of genotyping gels. bp, base pairs; ntc, no-template control.



Appendix 2. Initial gating strategy and control plots used during the phenotypic characterization of *Tcf21^{lin}* in adult mice. A and B. Representative flow cytometry plots of single cell suspensions from *Tcf21^{iCre/+};R26^{tdT/tdT}* lineage traced adult mice stained with antibodies against CD31, CD45, CD326 and PDGFR- α or selected controls. **A.** Initial gating strategy to select for live cells during analysis. Debris, doublets and dead cells were excluded (Left, center and right plots respectively). DAPI was added to the samples as a dead cell stain prior to acquisition. **B.** Plots gated from a live population from samples stained individually with each of the antibodies against CD31, CD45 or CD326 show that that each antibody allows to detect a population of positive events.

12. List of Figures

Figure 1. Induction of Cre-recombination in Tcf21 ^{iCre/+} ;R26 ^{tdT/tdT} mice.....	53
Figure 2. Spatial distribution of Tcf21 ^{lin}	54
Figure 3. Tcf21 ^{lin} constitute a mesenchymal population primarily composed of PDGFR- α ⁺ cells in the adult mouse.....	56
Figure 4. Confocal imaging of PCLS from a Tcf21 ^{iCre/+} ;R26 ^{tdT/tdT} mouse labeled with fluorescently conjugated Lectin (Lectin-DyLight649).....	57
Figure 5. Induction of Cre-recombination for lineage tracing of Tcf21 ⁺ cells during postnatal alveolarization.....	58
Figure 6. Neutral lipid droplets are highly prevalent in Tcf21 ^{lin} cells during late lung development.....	59
Figure 7. Tcf21 ^{lin} cells express the lipid droplet binding protein ADRP during late lung development.....	60
Figure 8. Tcf21 ^{lin} cells maintain close contact with alvolar type 2 cells during alveolarization	62
Figure 9. Early postnatal lineage tracing of Tcf21 results in more specific labeling of ADRP-expressing cells after the peak of secondary septation than ADRP lineage labeling.....	62
Figure 10. Proliferation of Tcf21 ^{lin} cells during secondary alveolarization.....	63
Figure 11. A very small proportion of Tcf21 ^{lin} cells contribute to the myofibroblast pool during secondary septation.....	64
Figure 12. Validation of the post-pneumonectomy compensatory regrowth model.....	65
Figure 13. Experimental workflow for the study of the Tcf21 lineage during compensatory regrowth.....	66
Figure 14. Pulmonary Tcf21 ^{lin} cells are localized to the lung parenchyma in both sham and pneumonectomized mice.....	67
Figure 15. Tcf21 ^{lin} cells preserve PDGFR- α expression in the mouse after PN.....	68
Figure 16. Tcf21 ^{lin} cells show lipofibroblast characteristics, which are maintained during neo-alveolarization after pneumonectomy.....	69
Figure 17. Studying the impact of Tcf21 ^{lin} cell depletion in compensatory lung regrowth....	70
Figure 18. Macroscopic findings during compensatory lung regrowth model after Tcf21 ^{lin} cell depletion.....	72

Figure 19. Stereological analysis of the effect of Tcf21 ^{lin} cell depletion on compensatory lung regrowth.....	74
Figure 20. Tamoxifen injection of adult Tcf21 ^{iCre/+;R26^{tdT/DTA}} mice results in partial depletion of Tcf21 ^{lin} cells.....	76
Figure 21. Experimental workflow for evaluation of the effect of TCF21 ^{lin} cells on a model of alveolosphere formation.....	78
Figure 22. Tcf21 ^{lin} cells are important for alveolosphere formation.....	80
Figure 23. Tcf21 ^{lin} cells promote alveolosphere formation in absence of direct contact with alveolar epithelial type 2 cells.....	81
Figure 24. Prominent features of Tcf21 ^{lin} cells in murine alveoli.....	92

13. List of Tables

Table 1. Differences between human and murine respiratory systems.....	11
Table 2. PCR primers for mouse genotyping.....	28
Table 3. PCR programs for genotyping of transgenic mice.....	29
Table 4. Tamoxifen dosing schemes used in this work.....	30
Table 5. Primary antibodies used in this work.....	48
Table 6. Secondary antibodies and detection systems used in this work.....	49
Table 7. Stereological analysis of the structural impact of partial Tcf21 ^{lin} cell depletion on compensatory lung regrowth.....	73

14. List of Abbreviations

2D	Two-dimensional
3D	Three-dimensional
4-OH-Tmx	4-Hydroxytamoxifen
ACTG1	Actin gamma 1
ADRP	Adipocyte differentiation-related protein
ADRP^{lin}	ADRP lineage-traced cells
AEC1	Alveolar epithelial cells type 1
AEC2	Alveolar epithelial cells type 2
bp	Base pairs
BSA	Bovine serum albumin
CE	Coefficient of error
CL	Cardiac lobe
CT	Computed tomography
CV	Coefficient of variation
DAPI	4',6-Diamidino-2-phenylindole
ddH₂O	Double distilled water
DMEM	Dulbecco's modified Eagle medium
DNA	Deoxyribonucleic acid
DTA	Diphtheria toxin A
ECM	Extracellular matrix
EDTA	Ethylenediaminetetraacetic acid
EdU	5-ethynyl-2'-deoxyuridine
EpCAM	Epithelial cell adhesion molecule
FACS	fluorescence-activated cell sorting
FGF10	fibroblast growth factor 10
Fig.	Figure

FITC	Fluorescein isothiocyanate
FMO	Fluorescence minus one
<i>g</i>	Gravitational acceleration
HBSS	Hanks' balanced salt solution
HEPES	4-(2-hydroxyethyl)-1-piperazineethanesulfonic acid
i.p.	intraperitoneally
IgG	Immunoglobulin G
kg	Kilogram
LL	Left lobe
α-MEM	Alpha minimum essential medium
μg	microgram
μl	microliter
μm	micrometer
μM	micromolar
mg	Milligram
ml	Milliliter
MLI	Mean linear intercept
mM	Milimolar
MS	Mass-specific (normalized to body mass)
n	Number
nCL	Right non-Cardiac lobes (cranial, middle and caudal right lobes)
NO	Non-operated
ntc	No template control
OsO₄	Osmium tetroxide
OP	Operation
P	postnatal day
<i>P</i>	P-value

p.i.	Post-injection
P/S	Penicillin/Streptomycin
PBS	Phosphate-buffered saline
PBST	1× Phosphate-buffered saline + 0,05% TWEEN® 20
PCLS	Precision-cut lung slices
PCR	Polymerase chain reaction
PDGFA	Platelet-derived growth factor A
PDGFR-α	Platelet-derived growth factor receptor alpha
PECAM-1	Platelet endothelial cell adhesion molecule
PFA	Paraformaldehyde
PNX	Pneumonectomy
Post-OP	Post-operative day
PPAR-γ	Peroxisome proliferator-activated receptor gamma
PTHrP	Parathyroid hormone-related protein
PTHrP-R	Parathyroid hormone-related protein receptor
RFP	Red fluorescent protein
rMC	Resident mesenchymal cells
RL	Right lung
RNA	Ribonucleic acid
rpm	Revolutions per minute
RT-PCR	Reverse transcription-PCR
Sca-1	Stem cells antigen-1
SD	Standard deviation
α-SMA	Alpha smooth muscle actin
SPC	Surfactant protein C
TCF21/Tcf21	Transcription factor 21
Tcf21^{lin}	Tcf21 lineage-traced cell(s)
TE	Tris-EDTA

TGF-β1	Transforming growth factor beta 1
Thy-1	Thymocyte antigen 1
Tmx	Tamoxifen
WFI	Water for injection
WT	Wild-type

15. Publications

- Rodríguez-Castillo, José Alberto, Alma Y. Arce-Mendoza, Armando Quintanilla-Siller, Adrian Rendon, Mario C. Salinas-Carmona, and Adrian G. Rosas-Taraco. 2015. "Possible Association of Rare Polymorphism in the ABCB1 Gene with Rifampin and Ethambutol Drug-Resistant Tuberculosis." *Tuberculosis* 95 (5): 532–37. <https://doi.org/10.1016/j.tube.2015.04.004>.
- Ntokou, Aglaia, Marten Szibor, José Alberto Rodríguez-Castillo, Jennifer Quantius, Susanne Herold, Elie El Agha, Saverio Bellusci, et al. 2017. "A Novel Mouse Cre-Driver Line Targeting Perilipin 2-Expressing Cells in the Neonatal Lung." *Genesis* 55 (12): e23080. <https://doi.org/10.1002/dvg.23080>.
- Pozarska, Agnieszka, José Alberto Rodríguez-Castillo, David E. Surate Solaligue, Aglaia Ntokou, Philipp Rath, Ivana Mižíková, Alicia Madurga, et al. 2017. "Stereological Monitoring of Mouse Lung Alveolarization from the Early Postnatal Period to Adulthood." *American Journal of Physiology-Lung Cellular and Molecular Physiology* 312 (6): L882–95. <https://doi.org/10.1152/ajplung.00492.2016>.
- Ruiz-Camp, Jordi, José Alberto Rodríguez-Castillo, Susanne Herold, Konstantin Mayer, István Vadász, Michelle D. Tallquist, Werner Seeger, Katrin Ahlbrecht, and Rory E. Morty. 2017. "Tamoxifen Dosing for Cre-Mediated Recombination in Experimental Bronchopulmonary Dysplasia." *Transgenic Research* 26 (1): 165–70. <https://doi.org/10.1007/s11248-016-9987-8>.
- Surate Solaligue, David E., José Alberto Rodríguez-Castillo, Katrin Ahlbrecht, and Rory E. Morty. 2017. "Recent Advances in Our Understanding of the Mechanisms of Late Lung Development and Bronchopulmonary Dysplasia." *American Journal of Physiology-Lung Cellular and Molecular Physiology* 313 (6): L1101–53. <https://doi.org/10.1152/ajplung.00343.2017>.
- Hoang, Tuong-Van, Claudio Nardiello, David E. Surate Solaligue, José Alberto Rodríguez-Castillo, Philipp Rath, Konstantin Mayer, István Vadász, et al. 2018. "Stereological Analysis of Individual Lung Lobes during Normal and Aberrant Mouse Lung Alveolarisation." *Journal of Anatomy* 232 (3): 472–84. <https://doi.org/10.1111/joa.12773>.
- Kalymbetova, Tatiana V., Balachandar Selvakumar, José Alberto Rodríguez-Castillo, Miša Gunjak, Christina Malainou, Miriam Ruth Heindl, Alena Moiseenko, et al. 2018. "Resident Alveolar Macrophages Are Master Regulators of Arrested Alveolarization in

Experimental Bronchopulmonary Dysplasia.” *The Journal of Pathology* 245 (2): 153–59. <https://doi.org/10.1002/path.5076>.

Rodríguez-Castillo, José Alberto, David Bravo Pérez, Aglaia Ntokou, Werner Seeger, Rory E Morty, and Katrin Ahlbrecht. 2018. “Understanding Alveolarization to Induce Lung Regeneration.” *Respiratory Research* 19 (1): 148. <https://doi.org/10.1186/s12931-018-0837-5>.

Dzhuraev, Georgy, José Alberto Rodríguez-Castillo, Jordi Ruiz-Camp, Isabelle Salwig, Martin Szibor, István Vadász, Susanne Herold, et al. 2019. “Estimation of Absolute Number of Alveolar Epithelial Type 2 Cells in Mouse Lungs: A Comparison between Stereology and Flow Cytometry.” *Journal of Microscopy* 275 (1): 36–50. <https://doi.org/10.1111/jmi.12800>.

Ruiz-Camp, Jordi, Jennifer Quantius, Ettore Lignelli, Philipp F Arndt, Francesco Palumbo, Claudio Nardiello, David E Surate Solaligue, et al. 2019. “Targeting MiR-34a/ Pdgfra Interactions Partially Corrects Alveologenesis in Experimental Bronchopulmonary Dysplasia.” *EMBO Molecular Medicine* 11 (3): 1–17. <https://doi.org/10.15252/emmm.201809448>.

16. Acknowledgments

I must acknowledge first my supervisor Dr. Katrin Ahlbrecht for her continued advise, guidance, and patience, as well as for all those exciting discussions that happened during the development of this work.

Next I would like to thank Dr. Rory E. Morty for allowing me to be a member in his lab and for supporting my career from the very first moment we met.

Also, my thanks go to all current and past members of the Morty's lab which I met during these years because all of them contributed to make my experience in the lab a very memorable one. Specially, thanks to Jordi Ruiz, Claudio Nardiello, Ivana Mižiková for all the brainstorming. In several ways you have helped modeling the scientist in me. Thank you, Lina Ntokou for all your helpful advice. Thank you, Despoina Myti, Ettore Lignelli and David (Pérez) Bravo for so much fun! And thank you Solmaz Khagani and Georgy Dzhuraev for making me remember how much I enjoy teaching others.

I would like to extend my most sincere thanks to Tanja Enders, Kevin Wilson, and other staff at the animal facility. Without them, this work would have been a near-impossible task. I am grateful as well, to Ann Atzberger for her advice and technical assistance regarding flow cytometry.

I would like to thank next, Dr. Ana Ivonne Vázquez Armendariz for her excellent input and technical support during the development of the organoid assays, for her input during the planning of other experiments, and most importantly, for standing by me all along the way. Thank you for so much patience, care and love, my dearest wife.

Lastly, I thank my son Diego, who was born recently, for providing me with the last kick I needed to finish writing this thesis.

17. Affirmation

I declare that I have completed this dissertation single-handedly without the unauthorized help of a second party and only with the assistance acknowledged therein. I have appropriately acknowledged and referenced all text passages that are derived literally from or are based on the content of published or unpublished work of others, and all information that relates to verbal communications. I have abided by the principles of good scientific conduct laid down in the charter of the Justus Liebig University of Giessen in carrying out the investigations described in the dissertation.

[SIGNATURE REMOVED FROM DIGITAL VERSION]

José Alberto Rodríguez Castillo

Giessen, December 2020